THESIS FOR THE DEGREE OF DOCTOR OF PHILOSOPHY

Atmospheric corrosion of Mg and MgAl alloys–characterization and mechanisms

Mehrdad Shahabi-Navid

Department of Chemistry and Chemical Engineering

Chalmers University of Technology

Gothenburg, Sweden 2015

Atmospheric corrosion of Mg and MgAl alloys–characterization and mechanisms

Mehrdad Shahabi-Navid

ISBN: 978-91-7597-249-7

Doktorandsavhandlingar vid Chalmers tekniska högskola

Ny serie nr: 3930

ISSN: 0346-718X

Division of Energy and Materials

Department of Chemistry and Chemical Engineering

Chalmers University of Technology

412 96, Gothenburg

Sweden

Phone: +46 (0)31 772 2850

Cover: 3D imaging of corrosion pits formed on alloy RC AM50 exposed at 95% RH and 22°C in the presence of 70 µg/cm² NaCl for 672 h: (a) in the presence of 400 ppm CO_2 and (b) in the absence of CO_2.

Dedicated to

Atmospheric corrosion of Mg and MgAl alloys–characterization and mechanisms

Mehrdad Shahabi-Navid
Department of Chemistry and Chemical Engineering
Chalmers University of technology

Abstract

The atmospheric corrosion of Mg and MgAl alloys was investigated. Corrosion tests were performed in the laboratory under controlled environment. CP Mg, AM50 and AZ91 samples were exposed at 95% RH and 22°C in the presence and in the absence of 400 ppm CO_2 for 24 h to 672 h. The passive film was characterized by means of XPS, FTIR, AES and XRD. The film consisted of $MgO/Mg(OH)_2$ with carbonate on top in the presence of CO_2. In addition, Al^{3+} was present in the film formed on the alloys. The thickening of the surface film was described in terms of a hydration mechanism. Also, a dissolution-precipitation mechanism was proposed for the break-down of the passive film in humid air. FIB cross-sectioning revealed that, in the presence of CO_2, dissolution of the passive film increased compared to CO_2-free exposures.

The NaCl–induced atmospheric corrosion of Mg and MgAl alloys was studied in the same environment. Brucite ($Mg(OH)_2$) was the main corrosion product in the absence of CO_2. In the case of the alloys, meixnerite ($Mg_6Al_2(OH)_{18}\cdot 4.5H_2O$) was also detected. Magnesium hydroxy carbonates were the dominating corrosion products in the presence of CO_2. All tested materials exhibited higher corrosion rates in the absence of CO_2 compared to exposures with CO_2. The electrochemical corrosion cells were more extensive in the absence of CO_2 compared to when 400 ppm CO_2 was present. EDX analysis revealed that η-phase particles were more efficient cathodes compared to the β-phase and the interdendritic areas. The FIB and BIB techniques combined with SEM-EDX revealed that Cl accumulated at the bottom of the pits.

The localized corrosion in the presence of NaCl (aq) was investigated in 2D and 3D. Plan view characterization was performed by means of SE and BSE imaging in SEM. Interference microscopy was employed to study the distribution of the pits after corrosion product removal. SEM-3D imaging of pitted regions was performed using a FIB-SEM system. It was shown that the β-phase acted as a barrier against corrosion, especially in the case of alloy AZ91. In the absence of CO_2, the corrosion pits tended to interconnect below the metal surface, forming severely pitted regions. In the presence of CO_2, the pits were isolated and shallower. The beneficial effect of CO_2 on corrosion is attributed to its acidity that caused neutralization of the catholyte.

Keywords: Atmospheric corrosion, Mg and MgAl alloys, Pitting, NaCl, CO_2, Characterization, Thin film, SEM, EDX, FIB, BIB, XRD, XPS, FTIR, Interference microscopy, 3D imaging

Appended papers

This thesis is based on the following papers:

I. M. Shahabi-Navid, M. Esmaily, J.-E. Svensson, M. Halvarsson, L. Nyborg, Y. Cao, L.-G. Johansson, NaCl-induced atmospheric corrosion of the MgAl alloy AM50 in semi-solid cast and high pressure diecast form; the relation between alloy microstructure and corrosion, In: Corrosion, In: Characterization, Simulation, In: DGM International Congress on Light Materials (LightMAT), Editor: A. Lohmüller, Bremen, Germany, 2013.

II. M. Shahabi-Navid, M. Esmaily, J.-E. Svensson, M. Halvarsson, L. Nyborg, Y. Cao, L.-G. Johansson, NaCl-induced atmospheric corrosion of the MgAl alloy AM50 - the influence of CO_2, Journal of the Electrochemical Society, vo. 161, issue 6, pp. C277-C287, 2014.

III. M. Shahabi-Navid, M. Esmaily, Y. Cao, L.-G. Johansson, J.-E. Svensson, NaCl-induced atmospheric corrosion of two MgAl alloys in semi-solid cast and diecast states – Influence of microstructure and CO_2, In: Corrosion Understanding and Mitigation, In: Corrosion Monitoring and Control, In: Materials Science and Technology (MS&T), Editor: G.-L., Song, Pittsburgh, Pennsylvania, USA, 2014.

IV. M. Shahabi-Navid, Y. Cao, M. Esmaily, J.-E. Svensson, L.-G. Johansson, Initial stages of corrosion of Mg and two MgAl alloys in humid air, Manuscript.

V. M. Shahabi-Navid, M. Halvarsson, M. Esmaily, J.-E. Svensson, L.-G. Johansson, Localized corrosion of semi-solid cast MgAl alloys in the presence of NaCl-a 2D and 3D investigation, Manuscript.

Statement of author's contribution:

I carried out the majority of the sample preparation and exposure experiments in all of the papers. In addition, I wrote most parts of the papers. I conducted all of the OP, SEM, EDX, FIB, BIB, 3D imaging and interference microscopy analysis. I did most of the XRD measurements. Also, I participated in the XPS and FTIR measurements. I carried out most of the data analysis.

Related papers not included in this thesis:

- M. Esmaily, M. Shahabi-Navid, J.-E. Svensson, M. Halvarsson, L. Nyborg, Y. Cao, L.-G. Johansson, Influence of temperature on the atmospheric corrosion of the MgAl alloy AM50 produced by semi-solid cast and high pressure die cast techniques, In: Corrosion, In: Characterization, Simulation, In: DGM International Congress on Light Materials (LightMAT), Editor: A. Lohmüller, Bremen, Germany, 2013.

- M. Esmaily, M. Shahabi-Navid, N. Mortazavi, J.-E. Svensson, M. Halvarsson, M. Wessén, A.E.W. Jarfors, L.-G. Johansson, Microstructural characterization of the Mg-Al alloy AM50 produced by a newly developed rheo-casting process, Materials Characterization, vol. 95, pp. 50-64, 2014.

- M. Esmaily, N. Mortazavi, M. Shahabi-Navid, J.-E., Svensson, M. Halvarsson, L. Nyborg, M. Wessén, A.E.W., Jarfors and L.-G., Johansson, Effect of Rheocasting on Corrosion of AM50 Mg Alloy, The Journal of the Electrochemical Society, vol. 162, issue 3, pp. C85-C95, 2015.

- M. Esmaily, M. Shahabi-Navid, J.-E. Svensson, M. Halvarsson, L. Nyborg, Y. Cao, L.-G. Johansson, Influence of temperature on the atmospheric corrosion of the MgAl alloy AM50, Corrosion Science, vol. 90, pp. 420-433, 2015.

- M. Esmaily, N. Mortazavi, M. Shahabi-Navid, J.-E., Svensson, L.-G., Johansson, M. Halvarsson, On the Capability of in-situ exposure in an environmental scanning electron microscope for investigating the atmospheric corrosion of magnesium, Ultramicroscopy, vol. 153, pp. 45-54, 2015.

List of acronyms

AES	Auger electron spectroscopy
BIB	Broad ion beam milling
BSE	Backscattered electron
CP	Commercially pure
DC	Diecasting
EBSD	Electron backscatter diffraction
EEM	Enthalpy exchange module
EDX	Energy dispersive X-ray spectroscopy
FIB	Focused ion beam milling
HPDC	High pressure diecasting
LLS	Linear least squares
OM	Optical microscopy
RC	Rheocasting
RE	Rear-earth
RH	Relative humidity
SCC	Stress cracking corrosion
SE	Secondary electron
SEM	Scanning electron microscopy
SKPFM	Scanning Kelvin probe force microscopy
SSC	Semi-solid casting
TEM	Transmission electron microscopy
TOF-SIMS	Time of flight-secondary ion mass spectroscopy
UTS	Ultimate tensile strength
VSI	Vertical scanning interferometer
XPS	X-ray photoelectron spectroscopy
XRD	X-ray powder diffraction

Table of contents

1. Introduction

1.1. Overview and background

The limited availability of fossil fuels and the harmful impact of exhaust gases on the environment have motivated the automotive industry to look for lighter materials to reduce fuel consumption [1]. With a density of 1.74 g/cm^3, magnesium (Mg) is the lightest metallic structural material, its density is about two-thirds that of aluminum (Al) and one-fourth that of iron (Fe). Also, its high specific stiffness as well as the excellent damping properties of Mg alloys meet the levels required in the automotive industry [1]. Moreover, the high strength to weight ratio of magnesium alloys makes them good candidates for aeronautical and aerospace applications [1, 2].

Being the eighth most abundant element in the earth's crust, the beneficial intrinsic characteristics of Mg and its alloys such as high electrical and thermal conductivity (e.g. in portable laptops) good electromagnetic shielding (e.g. mobile telephone casings), dimensional stability, machinability, recyclability, etc. have made these materials good candidates for a wide range of applications. This includes household utensils [3, 4] electronic devices [3, 5] and biomaterials technology [6]. While commercially pure magnesium is seldom used, Mg alloys are widely employed. MgAl alloys are the most popular class of alloys due to their beneficial mechanical and casting properties [7].

The majority of Mg alloy components are produced using the high pressure diecasting (HPDC) technique. This is a fast and cost-effective casting method in which the molten metal is injected into a mold under high pressure. Thus, components with high dimensional accuracy and thin sections can be manufactured using HPDC. However, the high pressure gives rise to a turbulent flow which causes surface oxide and gas entrapment in the cavity. The entrapped gas creates gas-filled pores in the cast part which impedes conventional heat treatment and reduces mechanical properties such as yield strength and ultimate tensile strength (UTS) [8, 9]. One way of solving this problem is to use mechanical working such as extrusion [10], rolling [11] and equal channel angular pressing (ECAP) ([12]. Another option to attain less porous material in the first place is semi-solid casting (SSC) where the starting material is a slurry (mixture of solid and melt) rather a liquid. Hence, less turbulent flow is achieved in SSC which results in less porous components compared to HPDC [13]. SCC will be further explained in section 2.4.2 of this thesis.

Conventional Mg alloys have poor strength at high temperatures. A major problem at elevated temperatures is creep failure. In recent years, new Mg alloys have been developed that provide better creep resistance compared to conventional Mg alloys. This has been mainly achieved through two mechanisms: grain refinement and the formation of intermetallic precipitates. The magnesium rare-earth (Mg-RE) alloys are known to have sufficient creep resistance up to 250°C [14]. The Mg-Y-Nd alloys (e.g. WE43 and WE54), with a good combination of mechanical and corrosion properties, have better creep resistance than most cast Mg alloys [15]. Another type of Mg-RE alloy more affordable than the WE series is Mg-Nd-Zn-Zr, referred to

as M10 (Russia) or ZM6 (China). Although not as strong as the alloy WE, ML10 or ZM6 has good creep resistance [16, 17]. Also, newly developed cast alloys such as the Mg-Zn-Si series are reported to have better creep resistance compared to conventional AZ91 [18]. The addition of silicon increases the fluidity of the melt and the resulting Mg_2Si intermetallic, which has low density and high hardness, can impede grain boundary sliding at high temperatures [18]. Mg-Sn-Sr alloy is also a good candidate for high temperature applications. Both Sn and Sr act as grain refiners in this alloy. Moreover, a series of intermetallic compounds form that have good thermal stability and provide the alloy with good creep resistance[19].

A major problem with magnesium and its alloys is the relatively poor corrosion resistance [2, 4] especially in the presence of chloride salts [20]. There are reports on the high susceptibility of Mg alloys to general and localized corrosion such as pitting and stress corrosion cracking (SCC) [2]. Magnesium alloys are prone to galvanic corrosion. A galvanic cell forms when two different metallic materials are connected electrically in the presence of an electrolyte. Consequently, one of the two components will be corroded preferentially (the anode). The standard electrode potential of Mg/Mg^{2+} is -2.38 V which is one of the lowest values (Li/Li^{+}: -3.04 V, Al/Al^{3+}: -1.66 V, Fe/Fe^{2+}: -0.41 V). In fact, magnesium has the lowest corrosion potential among engineering metals. The very fact that Mg corrodes easily has directed most of its applications in automobiles towards the interior parts such as dashboards, seat frames and steering wheels. The corrosion behavior of Mg alloys in corrosive solutions [21-23] and in the atmosphere [24-26] has been extensively investigated.

1.2. Aim

The aim of this thesis is to elucidate the atmospheric corrosion of Mg and MgAl alloys. The surface film that forms on Mg is known to be protective in dry air, however, at a high humidity Mg and its alloys corrode. Thus, it is important to understand the transition of the Mg surface film from its protective to its non-protective state and to recognize the respective characteristics of this film.

Another goal of this thesis is to investigate the NaCl–induced atmospheric corrosion of Mg and MgAl alloys with respect to the effect of CO_2 and microstructure. It can be assumed that the supply of CO_2 is limited in many situations like crevice corrosion. Thus, it is important to compare atmospheric corrosion properties in the presence and in the absence of CO_2. Although, the influence of CO_2 on corrosion has been investigated previously, this parameter has not been studied much in relation to alloy microstructure. For example, different microstructural constituents of the materials can influence the corrosion properties. Hence, particularly in the case of MgAl alloys, it is important to investigate the correlation of microstructure and corrosion.

2. Theory and literature review

2.1. Corrosion of Mg alloys

2.1.1. General characteristics

Magnesium, like most metals, forms a surface oxide in dry air [27]. Thus an MgO film forms on the surface that protects the metal from further oxidation. This is called the passive film. In the presence of water MgO is converted to $Mg(OH)_2$. $Mg(OH)_2$ is thermodynamically more stable in water, thus less soluble $\log K_s$ = -11.16 compared to $\log K_s$ = -6.33 for MgO [27]. Experiments have shown that a hydrated MgO film forms on the surface of Mg alloys exposed to air [28].

Mg and its alloys are reported to corrode electrochemically in aqueous media [29]. The reaction includes anodic dissolution of Mg according to:

$$Mg(s) \rightarrow Mg^{2+}(aq) + 2e^{-} \quad (1)$$

The corresponding cathodic reaction is the evolution of hydrogen [30]:

$$2H^{+}(aq) + 2e^{-} \rightarrow H_2(g) \quad (2)$$

In alkaline solutions hydrogen evolution occurs according to:

$$2H_2O + 2e^{-} \rightarrow H_2(g) + 2OH^{-}(aq) \quad (3)$$

The electrochemical corrosion of Mg in water corresponds to the sum of the two half-cell reactions (1) and (3):

$$Mg(s) + 2H_2O \rightarrow Mg(OH)_2(s) + H_2(g) \quad (4)$$

Pourbaix diagrams show the thermodynamic stability of different phases in aqueous corrosion. Figure 1 shows the Pourbaix diagram for the magnesium-water system at 25°C, for logC = -6 [31]. As can be seen in this figure, the $Mg(OH)_2$ is insoluble in an alkaline environment. In contrast, it dissolves in neutral and acidic solutions where Mg^{2+} is produced. Both MgO and $Mg(OH)_2$ are electronically insulating and therefore cannot act as cathodes. It should be noted that electrons can pass extremely thin insulating film by tunneling.

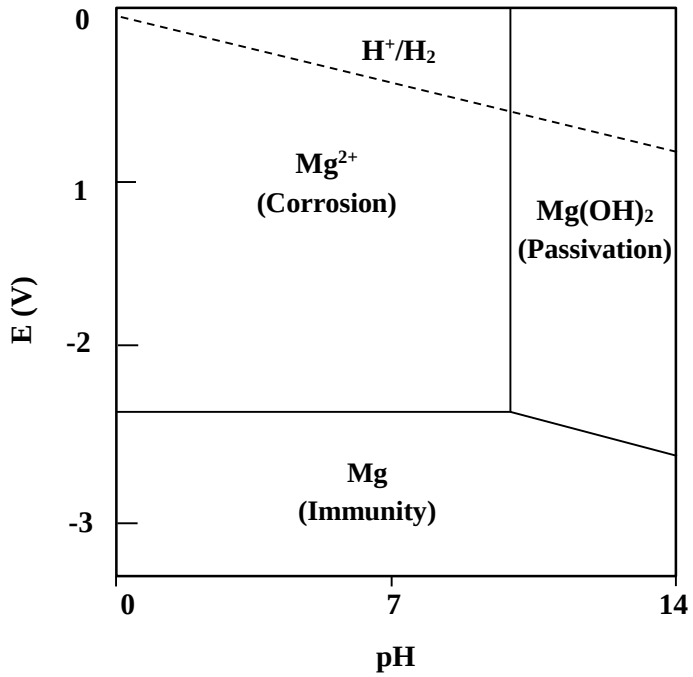

Fig. 1. Pourbaix diagram for Mg in water at 25°C, logC = -6 [31].

According to Song and Atrens, the rate of Mg corrosion depends on the availability of efficient cathodes [2]. Electrochemical corrosion of Mg can occur involving an external cathode (e.g. another metal connected to the Mg alloy) or an internal cathode (e.g. second or impurity phase) [2]. The presence of elements such as Fe, Ni and Cu in Mg alloys is deleterious for corrosion since they can form intermetallic compounds which act as cathodes [2]. High purity Mg alloys with a low amount of noble inclusions have higher corrosion resistance in chloride-containing environments than most commercial Mg alloys [32]. Figure 2 illustrates the electrochemical corrosion of Mg alloys with external and internal cathodes, respectively.

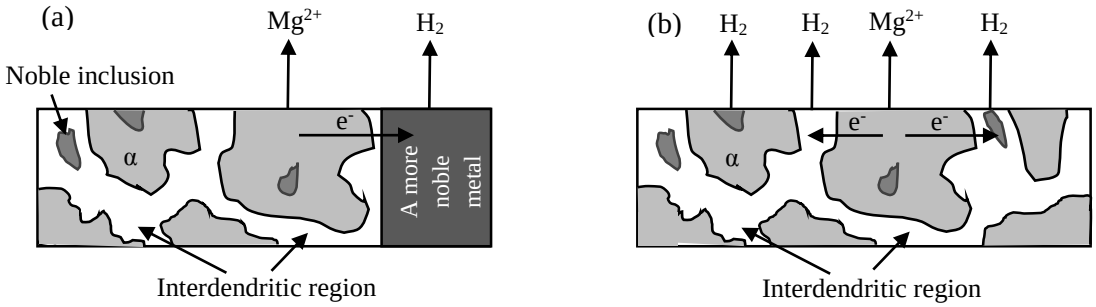

Fig. 2. Schematic illustration of the electrochemical corrosion of Mg alloys, (a) with external cathode (α-Mg is dissolved and hydrogen evolved on the more noble metal), (b) with internal cathode (α-Mg is dissolved and hydrogen is evolved on the noble inclusions).

2.1.2. MgAl alloys

Over 90% of magnesium alloy components are produced via casting, especially diecasting [33]. Major commercial MgAl alloys include the AZ series (MgAlZn), the AM series (MgAlMn) and the AE series (MgAlRE) [34, 35]. Aluminum is known to improve the castability and

mechanical properties of Mg. The former corresponds to the higher latent heat of solidification in the presence of Al [36], and the latter is mainly due to solid solution strengthening [37].

There are reports on the beneficial effect of increasing Al content on the corrosion resistance of MgAl alloys [2, 32, 38]. The Al-rich $Mg_{17}Al_{12}$ second phase that forms in MgAl alloys plays a role in corrosion [39]. The high aluminum content of $Mg_{17}Al_{12}$ precipitates (also known as β-phase) is believed to give rise a more protective passive film compared to that formed on the matrix material (i.e. solid solution of Al in α-Mg) [28, 40]. On the other hand, the β-phase is cathodic to the matrix [21, 41, 42]. The morphology and distribution of β precipitates has been reported to affect the corrosion of MgAl alloys [22-24]. A recent work by Cao et al. [43] noted that as-cast high purity Mg has a lower corrosion rate compared to as-cast and solution treated MgX alloys (X= Mn, Sn, Ca, Zn, Al, Zr, Si, Sr). It should be noted that high purity Mg and MgX alloys did not have the same concentration of impurities. Also, the solubility of the impurity elements in Mg may change due to the presence of various alloying elements.

As mentioned earlier, certain elements such as Fe are very detrimental to the corrosion resistance of Mg alloys because they have low solubility in Mg and form intermetallic compounds that can serve as efficient cathodes. Therefore, a tolerance limit is defined for such elements as shown in Fig. 3. The tolerance limit represents the solubility limit with respect to the fabrication conditions (not the thermodynamic solubility).

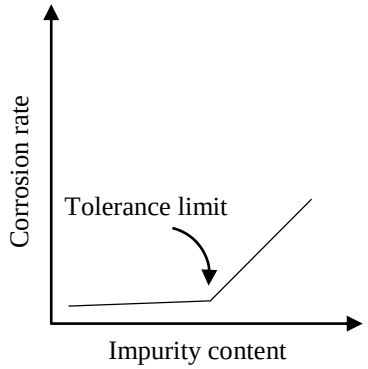

Fig. 3. Schematic illustration of the tolerance limit.

As depicted in Fig. 3, the corrosion rate increases drastically when the impurity content exceeds the tolerance limit. This value is alloy-specific and changes with respect to the manufacturing technique and the presence of other elements [20]. For example, the tolerance limit for iron reported for high purity magnesium is 170 wt.ppm [44]. However, it is shown in the literature that when 7 wt.% and 10 wt.% of Al is added to Mg, the tolerance limit decreases to 5 wt.ppm and to a negligible amount, respectively. This behavior is attributed to the formation of a Fe-Al precipitate that is more active as a cathode than iron-magnesium particles [45]. Manganese is added to a number of commercial alloys such as AZ91 and AM50 in order to increase corrosion performance. It is observed that the tolerance limit for iron in cast Mg alloys depends strongly on the Mn content of the alloy. Consequently, the Fe/Mn ratio is used as the measure for the tolerance limit instead of the concentration of Fe [46]. In the presence of Al and Mn, Fe

dissolves in AlMn particles that are much less detrimental for the corrosion properties than Al-Fe particles [32].

2.2. Atmospheric Corrosion

2.2.1. Atmospheric parameters

In the atmosphere, the required electrolyte in order for the electrochemical reactions to proceed is provided by *adsorbed water* and *liquid water*. When exposed to air, most metals form a thin oxide layer that protects the metal against further oxidation. This protective layer is called the "passive film". Although the passive film forms very fast, the reaction of the water adsorbed on the film with the substrate metal is slow [47]. It should be noted that in the case of noble metals such as gold, water is adsorbed directly on the metal surface. The amount of adsorbed water at a certain temperature depends on the vapor pressure of water, in other words on the relative humidity (RH). The RH is the ratio between the partial pressure of water in air and the saturation vapor pressure of water over liquid water at the same temperature:

$$RH = \frac{P_{H_2O}(T)}{P^{o}_{H_2O}(T)} \tag{5}$$

The amount of adsorbed water is reported to be about 1 monolayer of water at 20% RH at 25°C and about 10 layers of water at 95% RH [47]. A typical adsorption isotherm is shown in Fig. 4.

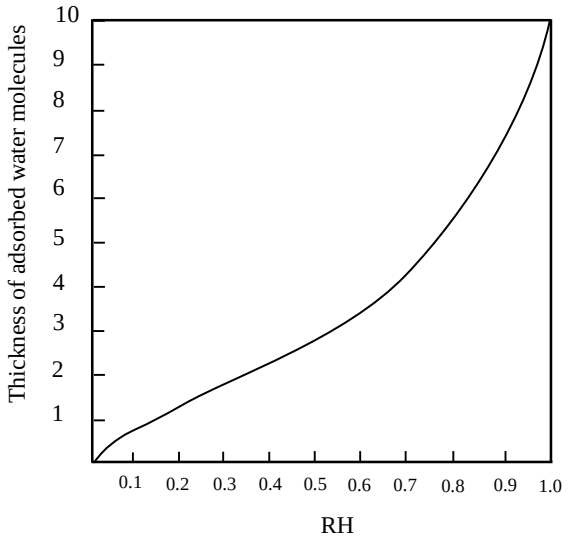

Fig. 4. Schematic adsorption isotherm for a metal exposed to air at 25°C [47].

Relative humidity is associated with dew point. The dew point is the temperature below which water vapor in the air condenses spontaneously, forming liquid water. For a constant amount of moisture in the air, RH decreases if the temperature increases. This is because, while water vapor pressure remains constant (constant amount of moisture), the saturation vapor pressure of water in air increases with temperature. In the outdoor environment, RH varies during the day as the temperature changes.

Liquid water can be provided by condensation of water vapor (i.e. RH>100% for a clean system) directly on a solid surface, mist (i.e. suspension of water droplets in the air which typically occurs in the cold air above a warmer body of water), rain, splashing, etc. However, water by itself causes only limited corrosion in an uncontaminated environment [2, 48]. This is basically due to the low conductivity of pure water.

Atmospheric contaminants are deposited on surfaces by wet and dry deposition. In wet deposition, the substances are dissolved in an aqueous phase (e.g. rain). Deposition not involving water is considered dry deposition (whether the substrate is wet or dry). Atmospheric contaminants are produced both naturally and synthetically. Major pollutants include ***sulfur oxides*** (i.e. SO_2). Atmospheric corrosion is usually stimulated in the presence of SO_2, particularly in the case of steel [48]. In industrialized regions, human activities such as combustion of sulfur-bearing fuels are the main source of SO_2. Natural sources of SO_2 include volcanic eruptions, oxidation of hydrogen sulfide (H_2S), etc.[49].

Nitrogen compounds play a crucial role in the corrosion of materials, particularly by forming ***nitric acid*** (HNO_3). ***Ammonia*** (NH_3) is also active in corrosion processes. For example, it stimulates corrosion in season-cracking (a type of SCC) of brass. Ammonia is naturally formed during thunderstorms. According to reports, the increased concentration of the ammonium ion in rainfall over Europe corresponds to the increased use of artificial fertilizers [49].

Saline particles are also present in the atmosphere and cause corrosion. These particles may be divided into two groups. The first group is ***ammonium sulphate***, which accelerates corrosion initiation due to its hygroscopic and acidic characteristics. This compound is typically formed in industrial areas where significant concentrations of ammonia and H_2SO_4 aerosol co-exist. The second group includes ***marine salts*** with sodium chloride as the most important constituent [49]. Measurements show considerable concentrations of other ions such as potassium, magnesium and calcium in rainfall [50]. In regions where the temperature goes below zero during the winter, NaCl is used as an anti-freeze agent on roads. Chlorides are hygroscopic and the chloride ion is highly corrosive towards some metals. Deliquescent salts available in the environment (e.g. sea-salt and NaCl) and water soluble corrosion products (e.g. $MgSO_4$ in case of Mg) reduce the RH required for condensation. NaCl (s), $MgCl_2$ (s) and $ZnCl_2$ (s) form aqueous solutions above 75%, 33% and 10% RH, respectively [49, 51]. This extends the duration of wetness, thereby increasing the extent of corrosion [48]. Such pollutants also increase the conductivity of the aqueous film [2]. Table 1 shows the relative humidities of air in equilibrium with saturated salt solution at 20°C.

Table 1. Relative humidities of air in equilibrium with some saturated salt solutions at 20°C [49].

Salt in solution	RH (%)	Salt in solution	RH (%)
$CuSO_4 \cdot 5H_2O$	98	NaCl	76
K_2SO_4	98	$CuCl_2 \cdot 2H_2O$	68
Na_2SO_4	93	$FeCl_2$	56
$Na_2CO_3 \cdot 10H_2O$	92	$NiCl_2$	54
$FeSO_4 \cdot 7H_2O$	92	$K_2CO_3 \cdot 2H_2O$	44
$ZnSO_4 \cdot 7H_2O$	90	$MgCl_2 \cdot 6H_2O$	34
$3CdSO_4 \cdot 8H_2O$	89	$CaCl_2 \cdot 6H_2O$	32
KCl	86	$ZnCl_2 \cdot xH_2O$	10
$(NH_4)_2 \cdot SO_4$	81	NH_4Cl	80

Siliceous particles in the atmosphere are *non-absorbent*. Hence, they have little effect on corrosion. On the other hand, *absorbent* yet inert particles in the atmosphere, such as ***charcoal*** and ***soot,*** adsorb SO_2. Accordingly, by either co-adsorption of water vapor or condensation of water these particles facilitate the formation of a corrosive acidic electrolyte solution [49]. Charcoal and soot are electronic conductors and are active cathodes when in contact with metals [52].

Wetting frequency is also important. Rain, which can leach pollutants, causes less serious corrosion than continuous water splashing [48, 53]. If the flow of aqueous solution is fast enough to remove the protective layer, higher corrosion rates may result [54].

Table 2 shows common anions and cations existing in rain, sea-salt and fine tropospheric particles (particles in the lowest section of Earth's atmosphere).

**Table 2. ***Examples of composition of rain, sea-salt and fine tropospheric particles.
a: [55], b: [56], c: [57]

Ions	Rain (mg/l)[a]	Sea-salt (%)[b]	Fine tropospheric particles[c]		
			Urban (%)	Rural (%)	Marine (%)
Cl^-	0.36	55	0.6	2	10
NO_3^-	0.56	<1	6	4	3
SO_4^{2-}	1.17	8	28	37	22
Ca^{2+}	0.20	1	2	0.4	3
Mg^{2+}	0.12	4	n/a	n/a	n/a
Na^+	0.23	31	n/a	n/a	n/a
NH_4^+	0.56	<1	8	11	7
K^+	0.12	1	1	1	3
C(org+elem)	n/a	n/a	40	29	11

**The composition of sea-salt is constant while the composition of rain and tropospheric particles varies widely.*

Chloride is generally considered to be a major corrosion accelerator. Atmospheric corrosion of the passivating metals in the presence of Cl^- is often characterized by pitting. In chloride solutions, a critical potential is defined below which no pitting occurs, which is called the pitting potential. The pitting potential has often been reported to decrease linearly with $\log(Cl^-)$

(chloride activity or concentration) at constant pH [58, 59]. Research has shown [60, 61] that pit nucleation is set off at potentials below the pitting potential and above the passive potential. However, only metastable (or unstable) pits exist below the pitting potential. These grow for a brief period and then repassivate [60, 61]. Hence, although stable pits only form above the pitting potential, metastable pits form both below and above the pitting potential.

The process of pitting initiation and propagation in the presence of Cl^- is complex and several, partly conflicting hypotheses have been proposed to describe how Cl^- helps destroy the passive film on different metals and alloys. Several researchers argue that adsorbed Cl^- causes local dissolution of the passive film [62, 63]. Other investigators have proposed that chloride penetrates the passive film forming metal chloride at the film/alloy interface [64-66].

2.2.2. Corrosion of Mg alloys in an ambient atmosphere

Atmospheric corrosion environments may be divided into four types based on the level of contaminants: *rural* environments with a low level of anthropogenic pollutants, *urban* and *industrial* environments with higher levels of contamination and *marine* environment with a large quantity of salt aerosols. It has been reported in the literature [2] that Mg alloys show better corrosion resistance than mild steel in severe marine atmospheres. In general, the corrosion rate of Mg alloys is lower than for mild steel but greater than that of aluminum. Table 3 compares corrosion rate values obtained for alloy AZ91 (~9 wt.% Al), AZ51 (~5 wt.% Al), Al, Zn and mild steel exposed to different atmospheric environments. According to the table, the two MgAl alloys have lower corrosion rates than mild steel in all environments. However, in almost all cases, the corrosion resistance of MgAl alloys is poorer than for Al and Zn. Also, the lowest corrosion rate value in each environment is that of aluminum. In general, the rate of atmospheric corrosion slows with the exposure time. Atmospheric corrosion exposures typically run for several years.

Table 3. Corrosion rates in different atmospheric environments-comparison of MgAl alloys, Al, Zn and mild steel.

Material	Environment	Corrosion rate(μm/year)	Reference
AZ91	Rural	2.8	[67]
AZ91	Marine	6.4	[67]
AZ91	Urban/industrial	14	[67]
AZ51	Rural	14	[68]
AZ51	Marine	14.5	[68]
AZ51	Urban/industrial	12	[68]
Al	Rural	0-0.1	[69]
Al	Marine	0.4-0.6	[69]
Al	Urban/industrial	<1	[69]
Zn	Rural	0.2-3	[69]
Zn	Marine	0.5-8	[69]
Zn	Urban/industrial	2-16	[69]
Mild steel	Rural	5-9	[70]
Mild steel	Marine (mild)	26-60	[70]
Mild steel	Marine (severe)	57-100	[70]
Mild steel	Urban	7-45	[70]
Mild steel	Industrial	45-75	[70]

Atmospheric corrosion can also be studied in a controlled environment in the laboratory. A laboratory experiment is often designed to accelerate corrosion compared to real atmospheric environments. Thus, investigation of corrosion properties can be carried out much faster in the laboratory than in real atmospheric environments. Moreover, the effect of individual parameters can be studied in laboratory exposures. This is not possible in a real atmosphere where different parameters (e.g. RH, temperature, concentration of corrosive substances, etc.) vary continuously. The most common laboratory test is known as "salt spray" where specimens are exposed in a chamber where a salt-water solution is sprayed indirectly (onto the specimens). This type of experiment was first used for corrosion testing in 1914. In 1939, the neutral salt spray test was established as ASTM Method B 117. The traditional B 117 standard specifies continuous exposure to a fog of 5% salt solution at 35°C. Two limitations of B 117 are that: (a) the 5% salt solution is not necessarily the best representative of the service electrolytes and (b) continuous exposure does not meet the real conditions where the specimens experience cyclical changes in wetness, temperature, sunlight and corrosive solution concentration. As a result, modifications have been made to B 117 in the past years. Various electrolyte mixtures are currently being employed for different applications. Many methods have been developed that use different combinations of wet/dry cycling, temperature cycling and solution concentration cycling [71]. An example is the salt spray test adapted by Volvo Corporation is the STD

1027,1375; an accelerated atmospheric corrosion testing particularly designed to simulate road environments where sodium chloride constitutes a dominating corrosive component [72].

Salt spray tests are not the only methods used to investigate the NaCl–induced atmospheric corrosion behavior of metals. In the present work NaCl was added to the samples prior to exposure by spraying a saturated solution of NaCl in a mixture of ethanol and water. The sprayed samples were exposed in individual chambers by means of Nylon filaments and exposed to a controlled flow of air at constant RH and temperature. The RH was controlled by mixing dry and wet air. Similar controlled laboratory exposures have been performed previously [25, 73]. Another way of achieving a certain RH is to use a saturated or unsaturated salt solution in a closed container. In fact, any salt solution at a certain concentration and constant temperature is in equilibrium with a certain partial pressure of water vapor and provides a constant relative humidity [74]. This method has been used for atmospheric corrosion investigations [24, 75]. The latter technique was employed in the present work to study atmospheric corrosion in the absence of CO_2. In this case, KOH solution was used both as RH regulator and CO_2 getter. More information on the experimental set-up used in this work will be presented later in this thesis. Table 4 presents atmospheric corrosion rates measured for several materials (AZ91, AM60 (~5 wt.% Al), Al, Zn and carbon steel) using salt spray techniques and other controlled laboratory exposures [25, 76-79]. As can be seen, much higher corrosion rates were reported for MgAl alloys tested by salt spray techniques compared to constant RH laboratory exposures. Also, the corrosion rate for the materials tested in constant RH laboratory exposures have the order of Al<Zn<AZ91<AM60<carbon steel.

Table 4. Corrosion rates in salt spray test and in constant RH controlled laboratory exposures–comparison of MgAl alloys, Al, Zn and carbon steel.

Type of experiment	Material	Details	Corrosion rate (µm/year)	Reference
Salt spray	AZ91	Standard: GMN9319TP (168h: 1min salt spray+119min drying)	600	[76]
	AM60	Standard: GMN9319TP (168h: 1min salt spray+119min drying)	3100	[76]
Controlled laboratory exposure (constant RH and temperature)	AZ91	95% RH, 22°C, water vapour+350ppm CO_2, 70µg/cm^2 NaCl	15	[25]
	AM60	95% RH, 22°C, water vapour+350ppm CO_2, 70µg/cm^2 NaCl	37	[25]
	Al	95% RH, 22°C, water vapour+350ppm CO_2, 70µg/cm^2 NaCl	1.2	[77]
	Zn	95% RH, 22°C, water vapour+350ppm CO_2, 75.5µg/cm^2 NaCl	14.8	[78]
	Carbon steel	80% RH, 20°C, water vapour+350ppm CO_2, 140µg/cm^2 NaCl	50.5	[79]

A common method to evaluate the corrosion resistance of metals and alloys is immersion testing where specimens are suspended in a corrosive aqueous solution [21-23]. The pH and the composition of the solution can be monitored online. Immersion testing is generally more accelerated than atmospheric corrosion testing, because abundant electrolyte is available throughout the experiment. The mass of the corrosion product is not measured in this type of experiment because corrosion products may fall off the specimen and dissolve. This is aggravated by hydrogen evolution which gives rise to cracking of the corrosion products. Table 5 shows corrosion rates for AZ91D, AM60, Al, Zn and mild steel in immersion tests. A comparison of the corrosion rates assigned to an individual metal or alloy in Tables 3, 4 and 5 shows that immersion tests tend to be more severe than the other types of corrosion experiments discussed in this section.

Table 5. Corrosion rates in immersion test–comparison of MgAl alloys, Al, Zn and mild steel.

Material	Details	Corrosion rate (μm/year)	Reference
AZ91D	pH: 5.6, 3.5% NaCl	≤182	[80]
AM60 (Fe/Mn: 0.0071)	pH:~7, 5% NaCl	3407	[81]
Al	pH:~7, 0.01M NaCl,	0.68-1.76	[82]
Zn	Laboratory distilled water	36-77	[83]
Mild steel	pH: 5, 3% NaCl	1050	[84]

2.3. Role of CO_2

The ambient concentration of CO_2 is about 400 ppm with slight local variations according to the latitude and/or human activity. Notably, depletion of CO_2 occurs during corrosion for instance in crevices [85] and underneath organic coatings [86]. Lindström et al. [25] have shown that the atmospheric corrosion of MgAl alloys is inhibited by CO_2.

pH and corrosion products

The presence of CO_2 changes the corrosion chemistry of the surface due to its acidic properties. The pH of water at equilibrium with the atmospheric level of carbon dioxide is 5.6 [27]. The slight acidity is due to the reactive dissolution of CO_2. When dissolved in water, CO_2 forms carbonic acid:

$$CO_2(g) \rightarrow CO_2(aq) \quad (6)$$

$$CO_2(aq) \rightarrow H_2CO_3(aq) \quad (7)$$

Carbonic acid protolyzes to form carbonate and hydroxy carbonate:

$$H_2CO_3(aq) + OH^-(aq) \rightarrow HCO_3^-(aq) \quad (8)$$

$$HCO_3^-(aq) + OH^-(aq) \rightarrow CO_3^{2-}(aq) \quad (9)$$

Equations 6-9 occur both in liquid water and in adsorbed water films that are thick enough to be liquid water-like. Carbonate can react with Mg^{2+} and form magnesium hydroxy carbonates, e.g.:

$$5Mg^{2+}(aq) + 4CO_3^{2-}(aq) + 2OH^-(aq) + 4H_2O \rightarrow Mg_5(CO_3)_4(OH)_2 \cdot 4H_2O(s) \quad (10)$$

CO_2 can also react directly with solids such as $Mg(OH)_2$ (brucite), forming magnesium hydroxy carbonate, *e.g.*:

$$5Mg(OH)_2(s) + 4CO_2(aq) \rightarrow Mg_5(CO_3)_4(OH)_2 \cdot 4H_2O(s) \quad (11)$$

Magnesium hydroxy carbonates are electronically insulating and therefore cannot act as cathodes. It has been suggested that magnesium hydroxy carbonates can physically block anodic and cathodic sites and decelerate the corrosion process [25, 87].

During the corrosion of Mg alloys in the presence of NaCl (aq), there is a local increase in pH in the cathodic regions. This is caused by hydrogen evolution (reaction (3)) in combination with the migration of Na^+ ions to the cathodes. Conversely, the anodic areas are acidified because of the generation of $MgCl_2$ (aq). Hence, a pH gradient is established between anode and cathode. In an immersion test, the pH gradients generated by the corrosion process are counteracted by diffusion of ions into the bulk solution and by convection. However, in atmospheric corrosion where the amount of electrolyte is very small, these processes are much less important and strong pH gradients are expected to remain. On the other hand, the limited amount of electrolyte and the resulting short diffusion paths makes the effect of acidic gases (such as CO_2) more significant in atmospheric corrosion compared to immersion tests.

In addition to $MgO/Mg(OH)_2$, the passive film formed on MgAl alloys is expected to also contain Al^{3+}. As can be seen in the Al Pourbaix diagram in Fig. 5, aluminum hydroxide is stable at neutral and slightly acidic pH. Thus, neutralization of the electrolyte by CO_2 is expected to slow alumina dissolution [88, 89].

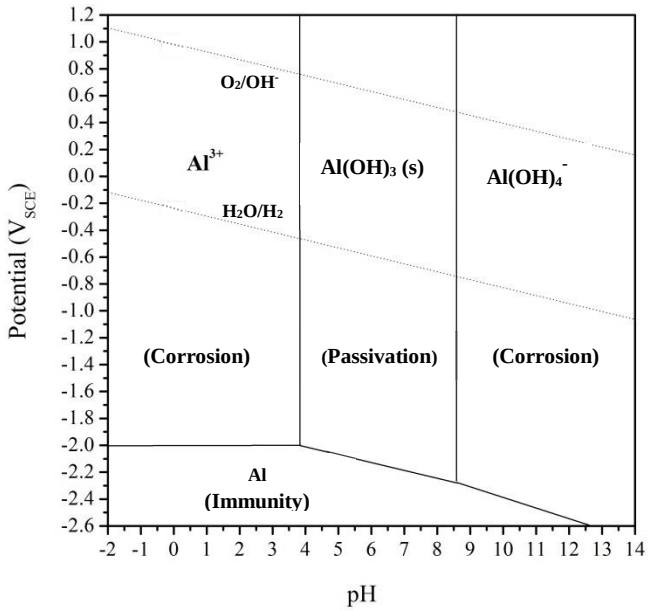

Fig. 5. Pourbaix diagram for Al in water at 25°C, logC = -6 [90].

A positive effect of CO_2 on the corrosion of MgAl alloys has been reported in the literature [25, 26]. The higher corrosion resistance in the presence of CO_2 might be attributed to the magnesium hydroxy carbonate film and to the alumina in the passive film. In the absence of CO_2, the corrosion product has been reported to include $Mg(OH)_2$ and a small amount of magnesium hydroxy chloride [25, 26]. In the presence of ambient concentration of CO_2, corrosion rates decrease significantly compared to exposure in the absence of CO_2. Lindström et al. have proposed that the NaCl–induced atmospheric corrosion of MgAl alloys in CO_2-free air, is similar to early stage corrosion of Mg alloys immersed in aqueous NaCl [25]. However, the corrosion rates reported for MgAl alloys in immersion tests (e.g. [80, 81]) are significantly higher than that in CO_2-free air exposures (e.g. [25]). This may correspond to the greater availability of NaCl (aq) (i.e. larger volume of electrolyte) in immersion test compared to CO_2-free air exposures. In addition, the convection in the electrolyte prevents a local increase in pH at the cathodic area and leads to the dissolution of $Mg(OH)_2$ (see Fig. 1).

2.4. Role of microstructure

2.4.1. Different phases and their properties

MgAl alloys (e.g. the AM and AZ series) basically consist of three microstructural components:

- α-Mg (solid solution of Al in Mg)
- β (Mg-Al intermetallic)
- η (Al-Mn intermetallic)

According to the Mg-Al binary phase diagram in Fig. 6, the solubility limit of Al in α-Mg is 12.7 wt.% at the eutectic temperature of 437°C. The eutectic composition contains 32.3 wt.% Al. The cast MgAl alloys form a dendritic microstructure in which the β-phase ($Mg_{17}Al_{12}$) is precipitated mainly between the dendrites. Also, there is an interdendritic region (also known as segregation band) that is rich in Al compared to the dendrites [91].

In the case of alloy AM50 with ~5 wt.% Al, when the melt is cooled below the liquidus line, the first solid that forms is α-Mg with significantly less Al than the maximum solubility at the eutectic temperature. Assuming an equilibrium solidification (in other words very slow cooling with sufficient solid-state diffusion) the final liquid transforms to a uniform solid solution at about 550°C. However, during a casting process, the cooling rate is fast and the system is far from equilibrium solidification. Hence, solid-state diffusion does not establish the equilibrium solid composition at each temperature as the alloy cools and the remaining liquid becomes increasingly Al-rich and solidifies at the eutectic temperature (i.e. 437°C) [92].

In non-equilibrium solidification, the amount of liquid present during cooling can be greater than predicted by the Lever rule. According to the Lever rule, complete mixing in the liquid and complete diffusion in the solid at each temperature are assumed to occur during cooling so that equilibrium is achieved. Non-equilibrium solidification can be described by the Scheil equation. In Scheil calculations, there is complete mixing in the liquid, but no diffusion in the solid is allowed [92]. Assuming that the liquidus and solidus curves are close to straight lines, the Scheil equation has the following form:

$$C_s = KC_o(1 - f_s)^{K-1} \tag{12}$$

where C_s is the concentration of solutes in the solid phase adjacent to the solid-liquid boundary, f_s is the fraction of solid phase in the solidifying alloy, C_o is the total concentration of solute in the alloy and K is the equilibrium partition coefficient.

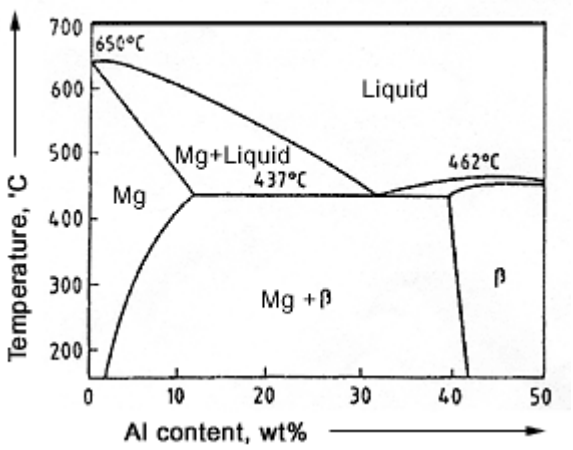

Fig. 6. Mg-Al phase diagram [93].

Measurements show [32, 41, 42] that η-phase is cathodic to both β-phase and α-Mg, and that the corrosion potential of β is between that of the other two constituents (being closer to that of η).

According to the literature, from the microstructural point of view, the corrosion resistance of the MgAl alloys mainly depends on the Al content of the alloy (and its gradient within the Mg matrix) [24], and on the shape and distribution of the β-phase [22]. Other factors, such as the chemical composition of Al-Mn intermetallic compounds [32] and the α-Mg grain size [21] have also been reported to influence the corrosion behavior of MgAl alloys.

By comparing a series of diecast (DC) MgAl alloys investigated in both salt spray and immersion tests (5% NaCl solution), Lunder et al. [32] proposed that increasing the Al level up to 4 wt.% improves the corrosion resistance drastically, while any further increase up to 9 wt.% results in a modest enhancement. In contrast, Pardo et al. observed that alloy AZ31 with 3.1 wt.% Al only reduced the corrosion susceptibility slightly compared to commercially pure Mg, while a huge improvement was achieved for the cast AZ80 and AZ91 alloys with 8.2 wt.% and 8.8 wt.% Al, respectively. It should be noted that alloy AZ31 was in wrought condition and that the materials were examined by immersion testing in 3.5% NaCl solution [22]. Jönsson and Persson confirmed that higher Al content reduces corrosion susceptibility, when they compared the atmospheric corrosion behavior of cast AM50 (5 wt.% Al) and AZ91D (9 wt.% Al) in the presence of NaCl [24]. They also suggested that NaCl–induced atmospheric corrosion of MgAl alloys initiated at the center of larger α-Mg grains since they possessed a lower amount of Al than that of smaller grains [24, 94]. In the abovementioned investigations, the Fe/Mn ratio of the alloys was less than 0.04, thus the effect of Fe-containing impurities on corrosion is considered insignificant.

It has been suggested that the β-phase has a dual role in the corrosion of MgAl alloys, meaning that it can serve both as a cathode and a corrosion barrier [21]. A continuous distribution and large fraction of β-phase has been shown to contribute significantly to reducing corrosion [21, 24]. Figure 7 shows how β particles can form a physical corrosion barrier. As can be seen, corrosion is initiated on the surface and proceeds through α-Mg until it is stopped at the β interface. In this scenario, β-phase is not expected to be protective in the initial stage of corrosion, but only after long exposures. On the other hand, after long exposures β (and in general all high Al content constituents of the microstructure) are reportedly affected by corrosion [24].

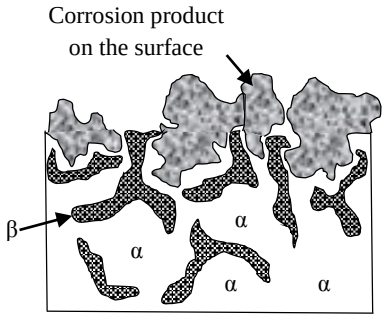

Fig. 7. Schematic cross-section overview of corroded AZ91D alloy, showing the β-particles surrounding the α-grains and acting as corrosion barriers. [2, 24, 42].

Lunder et al. have shown that the presence of Fe in the Al-Mn particles affect their cathodic behavior. They reported that if the iron level is higher than a few percent, the intermetallic precipitate acts as an efficient cathode [32].

Song et al. compared the microstructure of cast AZ91 alloys prepared using two different cooling rates [21]. They observed that the material manufactured with a slower cooling rate had larger α-grains and a lower amount of β-phase than one produced with a faster cooling rate. Also, in the case of the alloy with smaller grain size, β intermetallics were more continuously

distributed along the grain boundaries compared with agglomerated distribution of β in the case of the slowly cooled material. Their measurements showed lower corrosion rates for the rapidly cooled sample compared with the slowly cooled material [21]. There was no clear correlations between α grain size and the amount of β particles [21].

2.4.2. Modification of the microstructure using a SSC technique

Development of the SSC technique in the 70s led to the production of cast alloys with better quality than alloys prepared using conventional casting routes (e.g. diecasting). The major principle in SSC is that the starting material is a semi-solid slurry instead of a liquid, which gives rise to less shrinkage porosity. Moreover, when a viscous slurry is injected into a mold, the flow is non-turbulent; which prevents the entrapment of gas in the mold [13, 95].

In rheocasting (RC), one of the major SSC routes, the liquid material is mixed continuously with a stirrer while cooling down and becoming partially solidified, thus forming the slurry charge. The slurry is then injected into the mold cavity. As a result, the starting material is subject to a substantial shearing force which is believed to lead to a final microstructure with less dendritic structure [95]. Some of the alloys investigated in the present thesis were prepared by a modified RC technique. In this case, the melt was mixed continuously by means of a stirrer that was equipped with an enthalpy exchange module (EEM) on the head. The EEM consists of the same alloy as the melt. The EEM is lowered into the melt when the superheat reaches a desired value. The EEM cools the melt through the enthalpy of melting and induces shearing by stirring. The resulting slurry is made in typically less than ten seconds. The solid fraction of the slurry is adjusted by varying the liquid superheat and/or amount of EEM added. A vertical casting machine with a locking force of 50 tons was used in the present work.

Another SSC route is known as thixocasting (TC), where the ingot is heated until a slurry is achieved and the slurry is injected into the mold [13]. In one version the ingot was prepared using a stirring and cooling procedure [13]. Thus, the main difference between RC and TC is that the slurry is made by cooling a liquid in the former and by heating a solid material in the latter case.

Mathieu et al. compared the corrosion properties of MgAl alloys produced by SSC and HPDC. They reported an improved corrosion resistance in the case of the SCC material, because of the microstructural modification of the alloy. The major difference in the microstructure of the alloys prepared by SSC and HPDC was the formation of pre-existing α-Mg (in addition to the primary α) in the case of SCC alloy. The pre-existing α corresponds to the solid part of the slurry. When the slurry is injected into the mold the remaining liquid solidifies around the pre-existing α and forms the so called primary α. The higher corrosion resistance of SSC produced alloy was attributed to the aluminum content of the α-Mg (both pre-existing and primary) [23].

3. Materials and methods

3.1. Investigated materials

The materials investigated in this work include high purity MgAl alloys AM50 and AZ91 prepared by means of DC, HPDC and RC. In the case of DC and RC, a vertical casting machine with a locking force of 50 tons was used which had the capability of casting parts with a maximum projected area of 250 cm^2 [96]. The HPDC-AM50 alloy was cast in a horizontal casting machine with a gate speed about ten times faster than for DC-AZ91. Commercially pure (CP) Mg (99.97%) was employed as a reference material. Table 6 shows the chemical composition of the materials.

Table 6. Composition of the investigated CP Mg, AM50 and AZ91 materials. All values are in wt.%.

Material	Al	Mn	Zn	Si	Fe	Cu	Ni	Ca	Pb	Sn
CP Mg	0.0030	0.0023	0.0050	0.0030	0.0018	0.0003	0.0002	0.0010	0.0010	n.a.
AM50	5.0	0.25	0.01	0.01	0.0016	0.0010	0.0007	n.a.	n.a.	n.a.
AZ91	9.4	0.18	0.75	0.07	0.0074	0.0042	0.0007	0.0005	0.0011	0.0008

3.2. Sample preparation

The test coupons were machined as rectangular cuboids (approximate dimensions of 15×15×2 mm^3) with geometrical area of about 5.7 cm^2. The samples were wet-ground on SiC paper followed by two polishing steps with 3 and 1µm diamond paste. A suspension of colloidal silica in water (OPS) was used in the finishing step. The cleaned and dried samples were kept in a desiccator over a desiccant for 24 h before exposure. NaCl was applied before exposure by spraying a saturated solution of NaCl in an 80/20 mixture of ethanol and water. Two levels of salt (i.e. 14 and 70 µg/cm^2) were used. The salt was evenly distributed on the surface. Samples without salt were also exposed as references. Duplicate and triplicate samples were exposed.

3.3. Exposure set-up

3.3.1. Exposure in the presence of CO_2

Figure 8 shows the exposure set-up in the presence of CO_2. The exposure apparatus is entirely made of glass and Teflon. The samples are suspended by Nylon filaments in individual exposure chambers. There are eight parallel chambers each with an inner diameter of 55 mm and a volume of 0.4 dm^3. The chambers are immersed in a water tank held at the exposure temperature (i.e. 22.00±0.03°C). The temperature in the lab is kept at 25°C to avoid condensation in the parts of the apparatus outside of the water tank. A gas flow of 1000 l/min, corresponding to an average net flow velocity of 1 mm/s, passes through individual chambers in turn for 15 s. The relative humidity (RH) is regulated by mixing known amounts of dry air and air saturated with water vapor at the exposure temperature. The RH was 95.0% with an

accuracy of ±0.3%. CO_2 is added from a cylinder to give a constant concentration of 400±20 ppm.

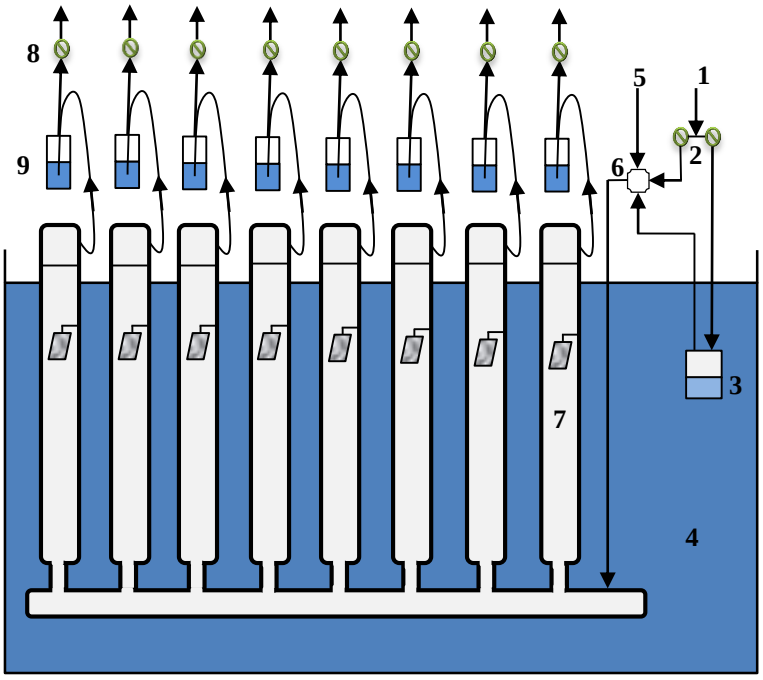

Fig. 8. The exposure set-up in the presence of CO_2. (1) dried purified air; (2) flow control; (3) humidifier; (4) water tank at constant temperature; (5) CO_2 inlet; (6) gas mixer; (7) eight exposure chambers with one sample in each; (8) solenoid valves; (9) wash bottles used for flow inspection.

3.3.2. Exposure in the absence of CO_2

The experimental set-up in the CO_2-free case is depicted in Fig. 9. The set-up includes a hermetically sealed desiccator (with a volume of 3 dm^3), immersed in a water tank kept at the experiment temperature (i.e. 22.00±0.03°C). The desiccator contained about 500 ml KOH (aq) solution which both retrieved CO_2 and regulated humidity to attain 95.0% RH. Specimens were hung on a holder inside the desiccator using Nylon filaments.

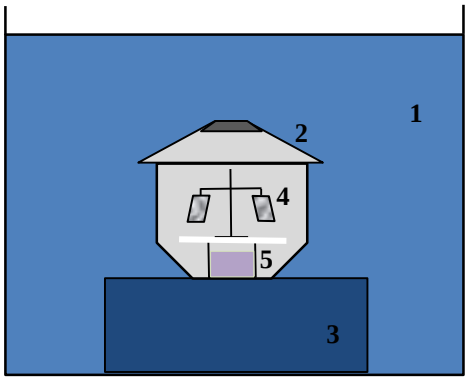

Fig. 9. The experimental set-up in the absence of CO_2. (1) water tank at constant temperature; (2) hermetically sealed desiccator; (3) platform for the desiccator; (4) specimens hung on the holder; (5) KOH (aq) solution.

3.4. Analytical methods

3.4.1. Gravimetric analysis

The samples were removed from the exposure environment for weighing at regular intervals using a six decimal balance. To avoid disturbing the corrosion process, specimens were weighed immediately. Hence, much of the water contained in the NaCl electrolyte remained during weighing and the corresponding values are accordingly termed *wet mass gains*. After discontinuing the corrosion experiment, the samples were stored in a desiccator over a desiccant for 24 h at room temperature so that the loosely bound water was removed. The specimens were weighed again and the corresponding values are termed *dry mass gains*.

Metal loss measurements were performed by leaching and pickling under sonication at ambient temperature. Leaching was carried out by immersing the samples in Milli-Q (ultrapure) water for 30 and 60 s. Soluble corrosion products and unreacted salt were removed at this stage. Afterwards, the samples were pickled at room temperature in a solution of 20% chromium trioxide (CrO_3) for 15 s following by several periods of 30 s. The samples were cleaned by pure water and acetone and finally dried by a stream of cold air. The metal loss and the mass of corrosion products were obtained by weighing the samples after pickling. Quantitative information on corrosion product stoichiometry can be achieved by calculating the corrosion product ratio according to:

$$\text{Corrosion product ratio} = \text{Mass of corrosion product} / \text{Metal loss} \quad (13)$$

where:

$$\text{Mass of corrosion product} = \text{Dry mass gain} + \text{Metal loss} \quad (14)$$

3.4.2. Optical microscopy

The macroscopic and microscopic evaluations of each specimen were carried out using a Leica and an Axio Vert.A1 metallurgical optical microscopy (OM) systems. The OM was employed to study the as-received microstructure of the materials as well as the corrosion product morphology.

A standard OM system consists of a light source which emits light on the specimen by means of a plain glass reflector installed in the microscope tube. An objective lens is located between the sample and the reflector which determines the image quality. Another set of lenses is placed near the eye as an eyepiece that can magnify the image (typically up to ×10).

3.4.3. Interference microscopy

After removal of the corrosion products in the pickling stage, 3D topography of the sample surface was obtained by interference microscopy using a RST Plus WYKO optical profiling system. The measurements were carried out in the vertical scanning interferometry (VSI) mode, where the vertical range was 0.5 mm with a resolution better than 10 nm. A 10× objective was used which produced a 457×610 μm² field of view. Also, line profiles were performed over typical corrosion pits.

An interference microscope is basically an advance optical microscope system plus an interferometer. Figure 10 depicts the schematic of an optical interference microscopy system. The principle of the technique is based on the destructive interference of coherent beams of light that are out of phase by half of a wavelength [97]. Interference microscopy technique uses fringe patterns to interpret the sample surface roughness. Fringes (interferograms) are the same as contour maps and allow a more accurate quantitative analysis of surface in comparison to similar methods (e.g. phase contrast).

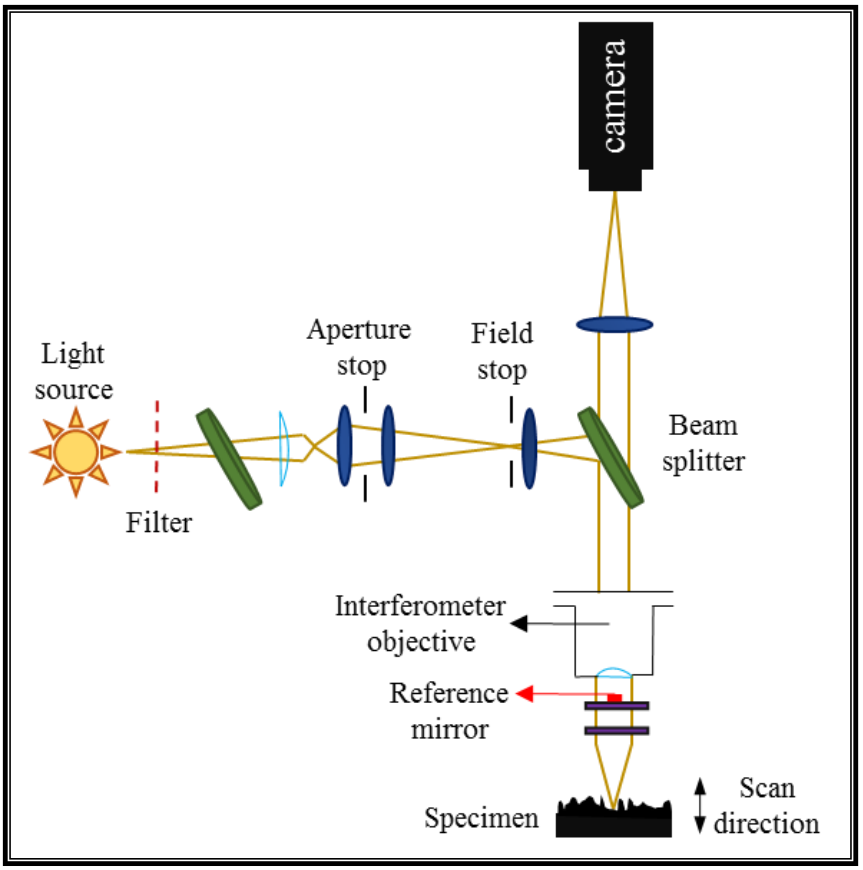

Fig. 10. Schematic illustration of optical interference microscopy system.

3.4.4. Infrared spectroscopy

The infrared (IR) spectroscopy was carried out to identify the functional groups in the corrosion products. The spectrometer used was a Nicolet 6700 from Thermo Scientific with insert cells for diamond attenuated total reflection (ATR) (DurasamplIR II from SensIR Technologies) and diffuse reflection fourier transform infrared (FTIR) (Collector II from Thermo Scientific). The spectrometer was equipped with a deuterated triglycine sulfate (DTGS) detector. The measurement range lies between 550 and 4050 cm^{-1} with a nominal resolution of 2.0 cm^{-1}. The sample is scanned 64 times and the data presented is an average value.

Figure 11 shows a schematic illustration of an IR system. The principle of the IR spectroscopy is the light absorption. When infrared light hits the specimen, some of it passes through (transmitted) the substance and the rest gets absorbed. The peaks at the resulting spectrum correspond to the frequencies of vibrations between the bonds of the atoms. Hence, the

measured infrared spectrum is a fingerprint of a certain compound. The FTIR system is the preferred type of IR spectroscopy. The original IR systems were of the dispersive type where energy frequencies were analyzed individually. The main advantage of a FTIR instrument over the dispersive type is that the former employs an interferometer which makes it possible to analyze all infrared frequencies simultaneously. The signals resulting from the interferometer (interferograms) are interpreted to intensities by means of Fourier transformation [98].

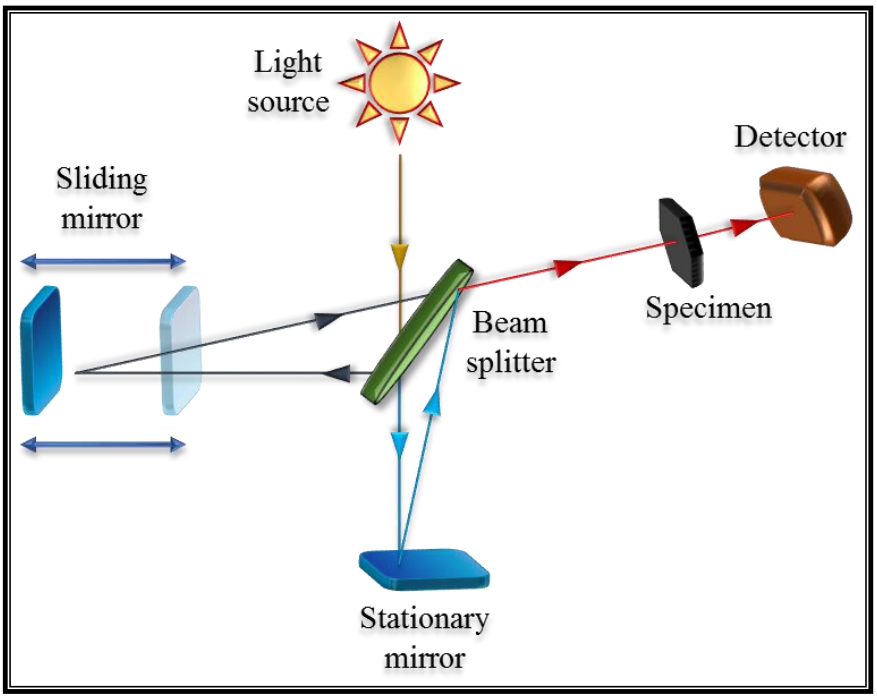

Fig. 11. Schematic illustration of the FTIR system.

3.4.5. X-ray powder diffraction

Crystalline compounds were identified using a Siemens D5000 X-ray powder diffraction (XRD) system and a Bruker AXS D8 advanced XRD system with Göbel mirror, using CuK_α radiation (λ = 1.5418 Å) and CrK_α radiation (λ = 2.29Å), respectively. Data were acquired typically in the range of 2θ: 5–80° in 0.05° increments using grazing incidence (GI-XRD) arrangement at 3° and 0.5°.

The principle of XRD is diffraction of the incoming X-ray. Figure 12 shows the illustration of XRD technique with respect to Bragg's law (15). In this way, constructive interference of X-ray occurs when the path length difference between two waves is equal to an integer (n) multiple of the wavelength (λ). On the other hand, the path difference between two waves is stated as $2d\sin(\theta)$ (see Fig. 12) where d is the interplanar distance between the atomic planes of the solid crystal, 2θ is the angle of diffraction and n represents the order of diffraction.

$$n\lambda = 2d\sin(\theta) \quad (15)$$

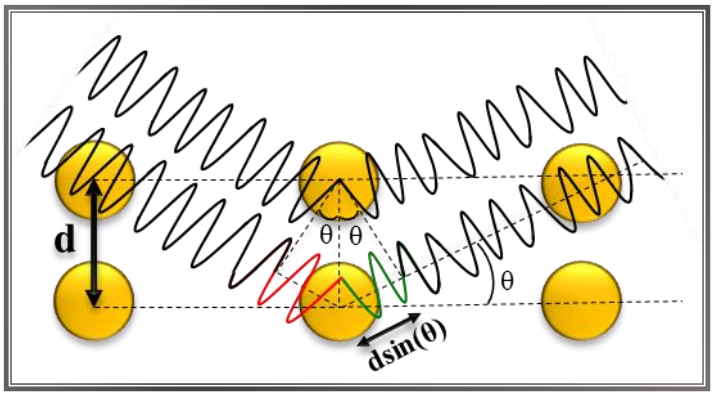

Fig. 12. Schematic showing the constructive interference meeting Bragg's law.

The GI-XRD arrangement at low angle of incidence was chosen in the present thesis due to the thin corrosion product that formed on the tested specimens. This was especially important in the case of brief exposures and exposures in the absence of salt. In GI-XRD, the incoming X-ray is radiated at the sample with a constant incidence angle. Also, a moving detector collects the diffracted X-ray photons at different angles. With the known X-ray wavelength (λ) and the measured θ, the d value is calculated (automatically by the software), which can be useful for identification of compounds.

3.4.6. X-ray photoelectron spectroscopy

A PHI 5500 X-ray photoelectron spectroscopy (XPS) system with an AlKα X-ray source (1486.6 eV) was employed. The acquisition conditions for the survey spectra were 93.9 eV pass energy, 45^{o} takeoff angle and 0.4 eV/step. The acquisition conditions for the region spectra were 23.5 eV pass energy, 45^{o} takeoff angle and 0.1 eV/step. Depth profiling was performed by successive XPS analysis and argon ion etching (4 kV) at an etch rate of 20.3 Å/min (calibrated by using Ta_2O_5 with known thickness under the same test conditions).

The XPS is a surface sensitive analysis that works at very high vacuum ($<10^{-8}$ millibar). It is capable of determining the composition of the surface layer and the element distribution in depth as well as the chemical state of an element. Although the depth resolution of the technique is generally smaller than 10 nm, the lateral resolution of a traditional XPS (e.g. the system that was employed in the present thesis) is ~1 mm. However, the modern XPS can reach lateral resolutions of ~10 μm. Figure 13 demonstrates the generation of a photo electron by X-ray emission. As shown in this figure, X-ray radiation ejects an electron which transfers to the vacuum carrying chemical information about the material.

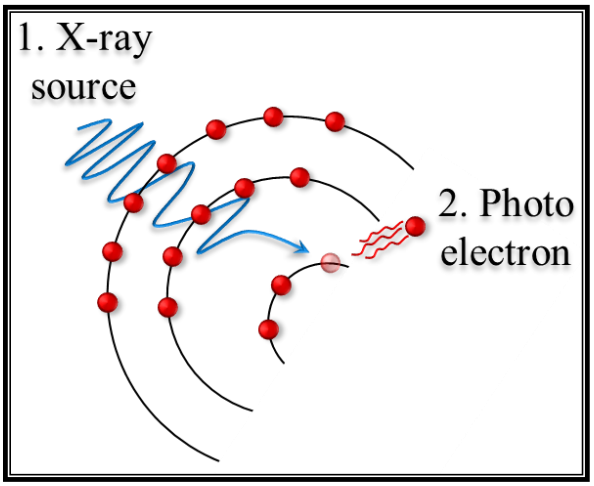

Fig. 13. Schematic illustration of an X-ray photo electron generation.

3.4.7. Auger electron spectroscopy

The Auger electron spectroscopy (AES) was carried out by means of a PHI 700 Xi scanning Auger nanoprobe with an accelerating voltage of 10 kV and beam current of 10 nA. Depth profiling was performed with 1 kV Ar^+ ion sputtering. The sputter rate at the sample position in the instrument was determined to be 5 nm/min for Ta_2O_5. The computer software PHI Matlab and the linear least squares (LLS) routine were used to separate the metal and metal oxide/hydroxide components in the depth profiles.

Just like the XPS technique, AES is a surface sensitive method. It is used to probe the composition of the surface layer and the element distribution in depth. It can also provide some chemical state information, but not as well as XPS. However, AES possesses high lateral resolution in the range of several tens of nm. An electron beam is normally employed as the source of energy in an AES instrument. As illustrated in Fig. 14, the electron beam may kick an electron off its position in an inner shell. Thus, the atom becomes energetically unstable. Relaxation occurs rapidly via an electron falling from a higher level to fill the core hole. The energy released in this process aids in the emission of the third electron. This is called the Auger electron, which contains characteristic information about the material. It should be noted that the atom may compensate the energy instability in a second way that will be explained in section 3.4.8. (Energy dispersive X-ray spectroscopy (EDX)) of this thesis. Furthermore, Auger electrons may be produced by X-ray radiations as well. In fact, Auger electrons are always collected in the XPS technique, however they are normally ignored. The kinetic energy of the Auger electron can be calculated as follows:

$$E_{kinetic} = E_A - E_B - E_C - \emptyset \qquad (16)$$

where E_A-E_B is the energy gained by core-hole annihilation, E_C is the energy needed to overcome the binding energy of the Auger electron to the work and ϕ refers to function.

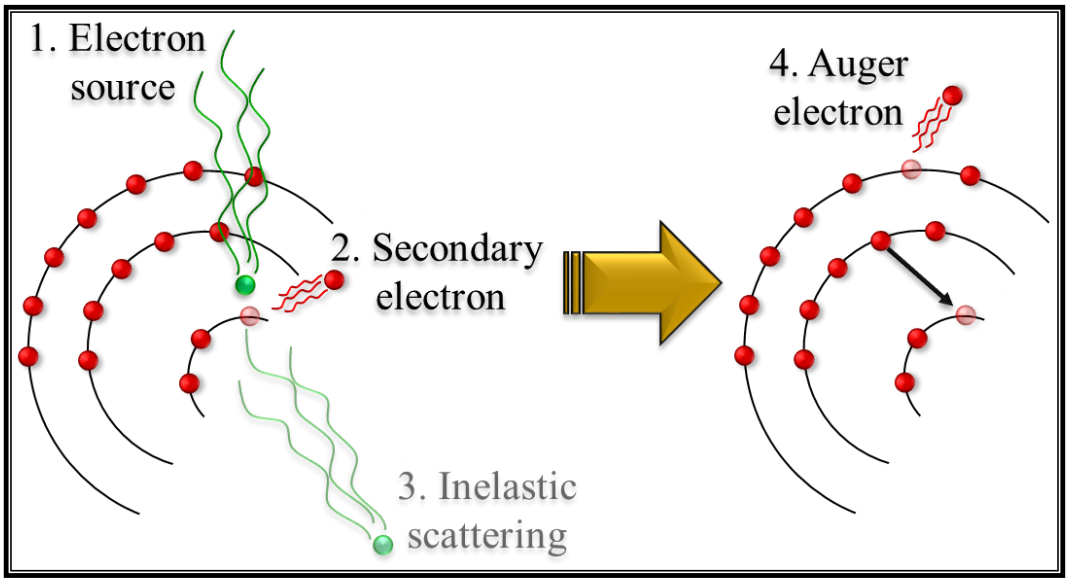

Fig. 14. Schematic illustration of an Auger electron generation.

3.4.8. Energy dispersive X-ray spectroscopy

In the present work EDX was carried in two scanning electron microscopes (SEMs)[1]. An Oxford Inca EDX detector was employed in both SEMs, which allowed the analysis of the local chemical composition and the elemental mapping. An electron beam with accelerating voltage of 15-20 kV was employed where the specimen was mounted at the working distance of 9-12 mm. Aperture size was adjusted to obtain an optimum signal count.

Figure 15 illustrates the characteristic X-ray generation as a result of electron beam radiation. When the beam kicks an electron off its location, another electron from outer shell migrates to the inner shell to fill the vacancy. As mentioned in section 3.4.7. (AES) of this thesis, in this case an Auger electron may be emitted. Instead X-ray may be generated as depicted in Fig. 15. This radiation is called the characteristic X-ray which contains unique information about the respective atom. The energy of the characteristic X-ray can be calculated as follows:

$$h\nu = E_A - E_B \tag{17}$$

where h is the Plank's constant, ν is the frequency of the radiation and as mentioned earlier E_A-E_B is the energy gained by core-hole annihilation.

As the atomic number increases the probability of characteristic X-ray emission also increases while that of AES decreases.

[1] See section 3.4.9. (SEM) for the specifications of the microscopes.

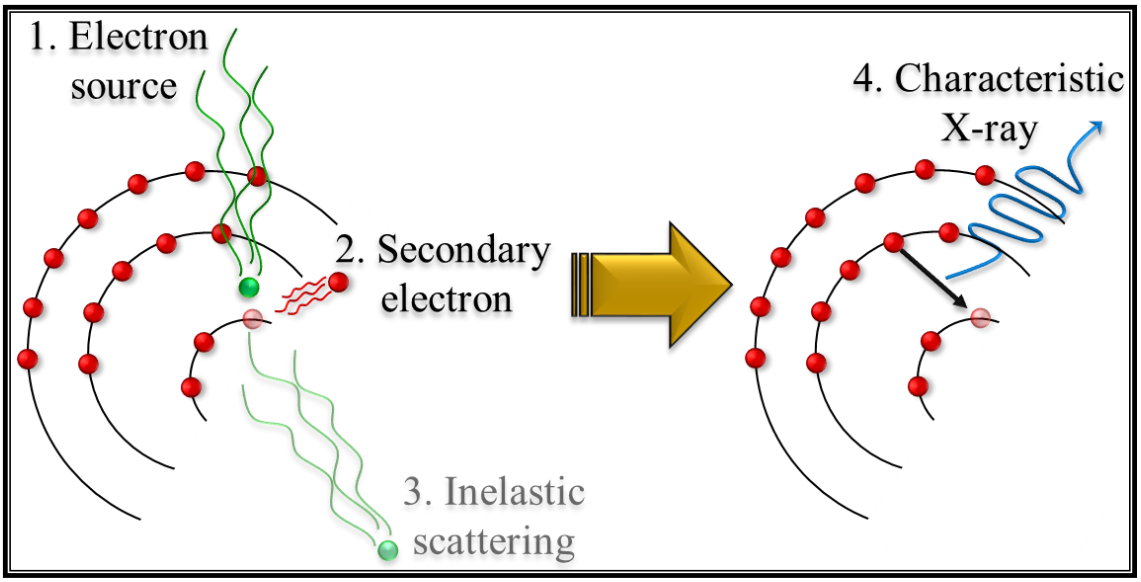

Fig. 15. Schematic illustration of characteristic X-ray generation.

3.4.9. Scanning electron microscopy

The microstructure of the as-cast material and the morphology of the corroded surfaces were investigated using an FEI Quanta 200 environmental scanning electron microscope (ESEM) and an Ultra 55 FEG SEM. Carl Zeiss AxioVision image analysis software was also employed to measure the area fraction of Mg-Al intermetallic particles (β-phase). A 1% nithal etchant was used to reveal alloy microstructure.

The SEM employs a narrow beam of electrons that is focused on the sample surface. Hence, atoms emit photons and electrons due to the impact of the incoming beam. As mentioned earlier, the analysis of a photon produced in this way is called EDX. The generated electrons are used for imaging. SEM imaging has two main modes based on the type of generated electrons: (a) secondary electron (SE) imaging and (b) backscattered electron (BSE) imaging. Figure 16 illustrates the process of SE and BSE generation. Thus, if the incoming electron escapes from the substance matter and returns towards the electron source, it is called BSE. BSEs may have precisely the same amount of energy as the incoming beam (elastic scattering) or they may have lost part of the original energy (inelastic scattering). On the other hand, the incident beam may hit and dislocate an electron from the substance atom that is called the SE. In this case the incoming beam scatters inelastically.

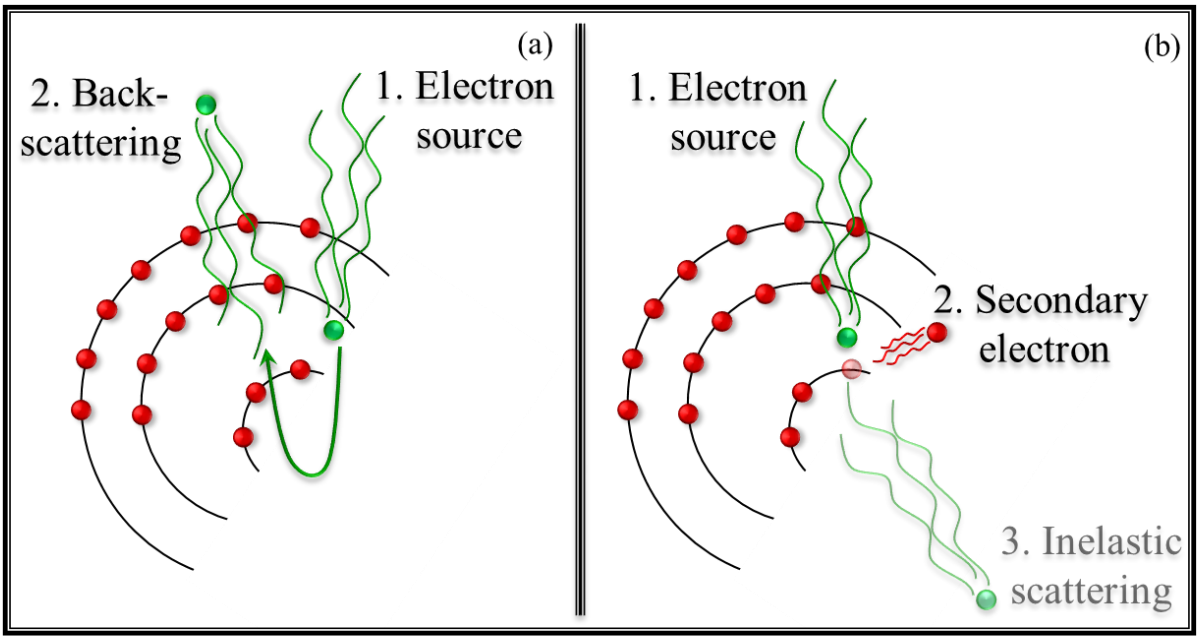

Fig. 16. Schematic illustration of (a) BSE and (b) SE generation.

The interaction volume of the incident beam and the substance matter determines the depth from which the electrons (particularly BSEs) and photons are emitted. The interaction volume has a pear-like shape and is dependent on the accelerating voltage and density of the sample. The illustration in Fig. 17 suggests a typical interaction volume for metals under 20 kV accelerating voltage. As can be seen, while BSEs are emitted from sections near the surface to the sections as deep as about 1 µm, the SEs are generated only at a thin subsurface region (1-50 nm deep). Figure 17 also shows that AES is a surface sensitive technique (Auger electron being generated 0.5-3 nm from top surface). Please note that the thickness at which Auger electrons are generated is analogous to that of X-ray photo electrons.

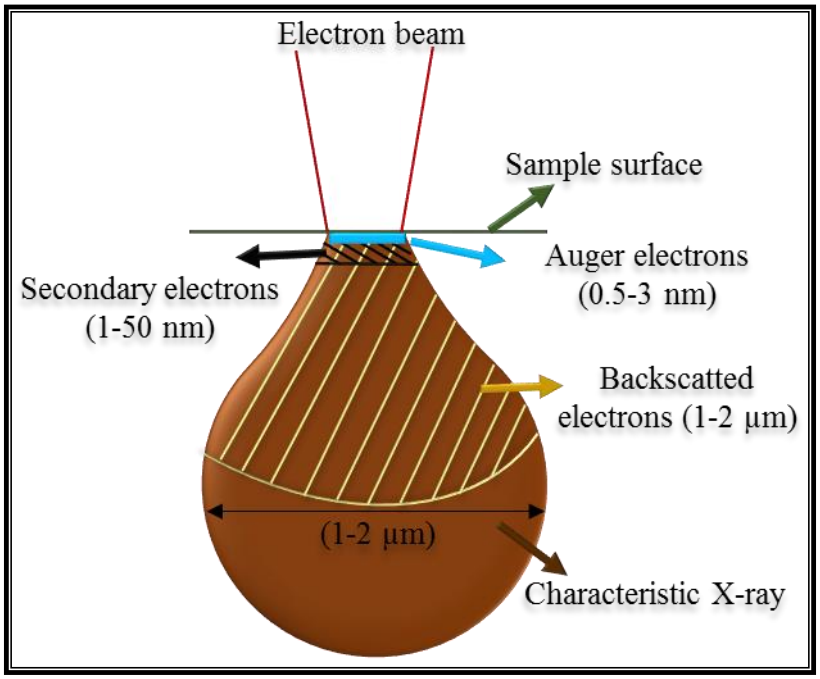

Fig. 17. Schematic of the interaction volume excited by a primary electron beam with 20 kV energy.

Since SEs are produced at a shallow thickness beneath the surface, the SE imaging mode gains better topography information than normal BSE imaging[2]. Hence, edges and sharp corners emit more SEs and will therefore be brighter in SE micrographs than horizontal surfaces. Figure 18 shows SE emission from a steep surface versus a horizontal surface. A greater fraction of excited volume lies along the sample surface of the steep surface compared to the smooth surface. Hence, more SEs can escape at the steep surface. On the other hand, BSE emission is sensitive to the local sample density and produces a chemical composition contrast. In general, the aforementioned contrast is referred to as Z-contrast[3]. In this way, a heavier (denser) substance is expected to emit more BSEs than a lighter (less dense) one.

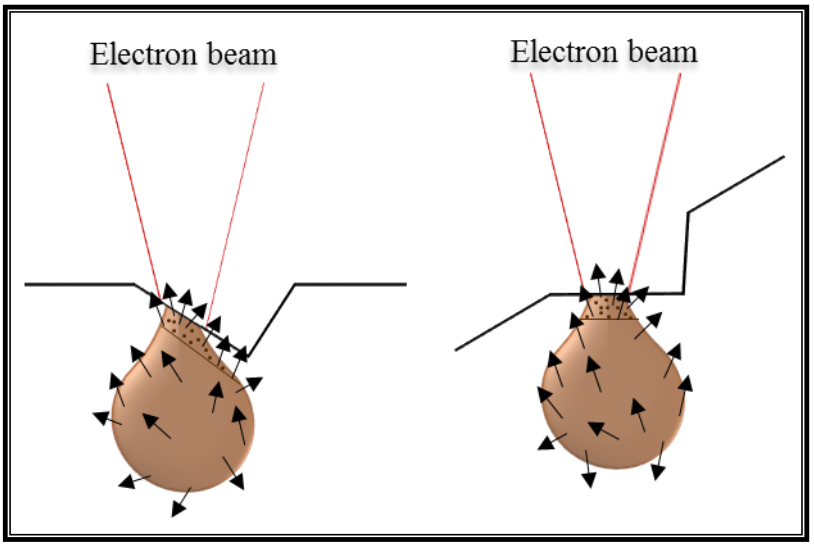

Fig. 18. Edge effect on the SE topographical imaging.

3.4.10. Focused ion beam milling

Focused ion beam (FIB) milling is a powerful method to produce cross-sections and thin foils. The thin foils are mainly used in transmission electron microscopy (TEM) analysis. Also, the foils can be used in the transmission electron backscatter diffraction (t-EBSD) technique. The cross-sections made by FIB are normally used for SEM imaging and SEM-EDX.

The incident beam in the FIB consists of Ga ions rather than electrons as in the SEM. Thus, it can be more destructive to the surface. In fact, this is the principle of milling, where material is removed when the ion beam scans the surface.

An FEI Versa 3D DualBeam FIB equipped with a Ga ion source was used to prepare cross-sections. The DualBeam system can use both electron and ion beams, where the ion beam is used mainly for the milling and Pt deposition processes and the electron beam is used for imaging and gentle Pt deposition.

[2] A specific BSE imaging mode can also be set to exclusively obtain topographical micrographs.
[3] "Z" represents the atomic number of elements.

3.4.10.1. Preparation of single cross-section using FIB

In the present thesis, FIB was employed for preparing cross-sections of corroded specimens. To achieve a smooth surface, several milling steps were performed where the ion beam current decreased gradually from the first (rough cutting) to the last (final polishing) step. Ion beam current was set at a range of 44 nA-2.7 nA at a 30 kV accelerating voltage. The sample was tilted 7° while milling, thus a 45° cross-section was obtained. The post-preparation analysis (e.g. EDX) was performed using a regular SEM system where the milled sample was mounted on a 45° pre-tilted holder. Hence, the milled cross-section was perpendicular to the electron beam and there was no obstacle between the cross-sectional surface and the beam source, neither between the cross-section and the detectors. Figure 19 shows the schematic of the milling and post-preparation analysis set-up.

3.4.10.2. 3D imaging using FIB

The FIB system was also used to prepare a stack of cross-sectional images after removing the corrosion products to prepare a 3D image. In this case, a constant ion beam current of 28 nA at 30 kV voltage was employed. Also, the thickness of each slice was approximately 500 nm. SE *in-situ* imaging was performed at the end of each milling pass at an accelerating voltage of 5.00 kV and a working distance of 10.0 mm. Figure 19 shows the schematic of slice and imaging and 3D reconstruction. The stack of slices prepared using FIB was compiled, aligned and processed by FIJI software (a distribution of open-source software ImageJ) [99] and a 3D illustration was created.

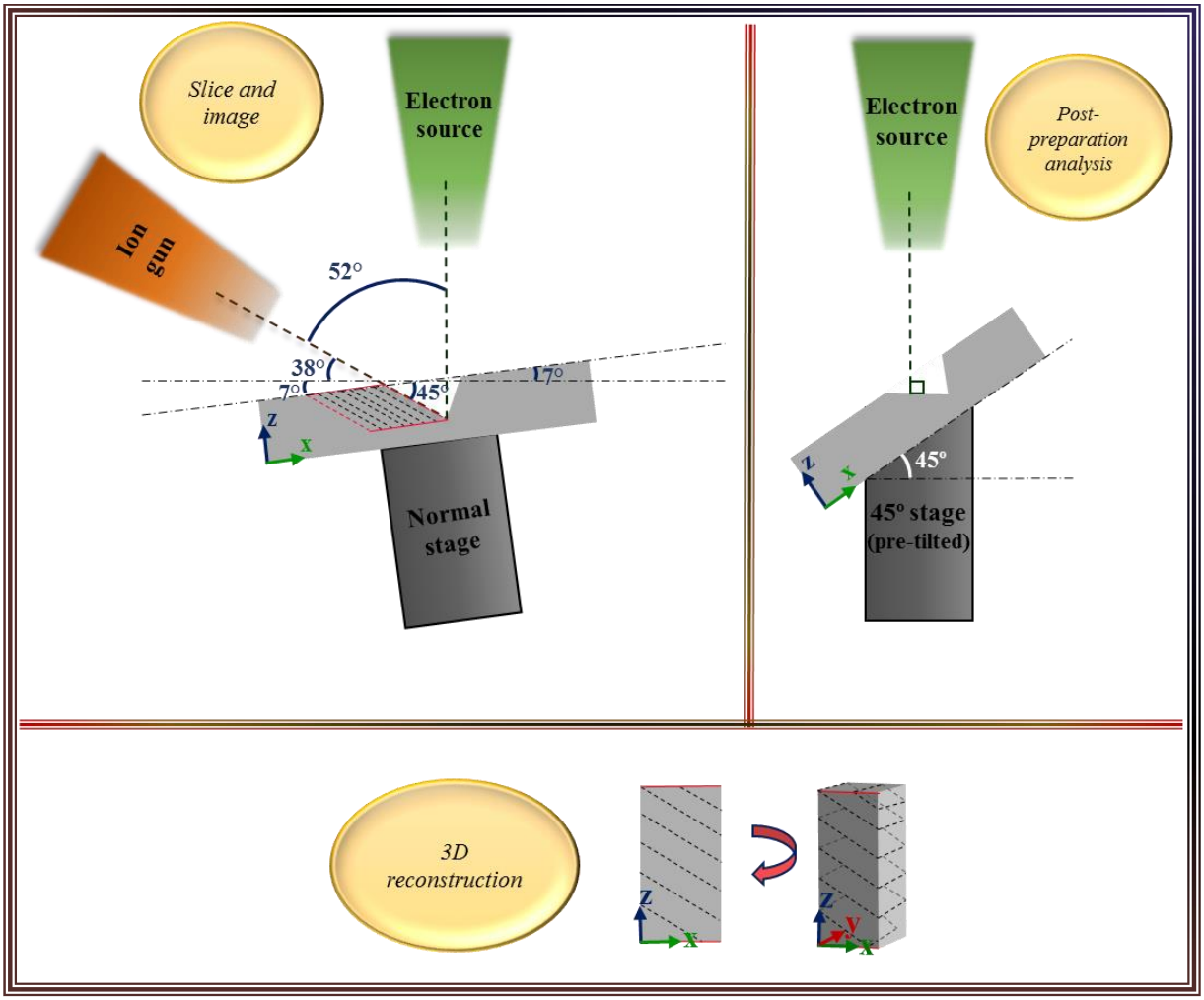

Fig. 19. Illustration of FIB milling showing the "slice and image", "3D reconstruction" and "post-preparation analysis" set-ups.

3.4.11. Broad ion beam milling

The FIB is not the most efficient tool for making wide cross-sections. In such cases, broad ion beam (BIB) milling, also known as "slope cutting", is often recommended. It is a surface preparation technique that utilizes a large (~1 mm) ion beam. A solid sputter-resistant shield blocks half of the beam and protects the top surface while stripping away a thin section of the sample.

In the present work, the corrosion layer and corrosion pits were studied using wide cross-sections (~500 µm) prepared by means of a Leica EM TIC 3X BIB equipped with three Ar ion sources. Figure 20 shows a schematic illustration of the BIB system set-up. As can be seen in this figure, a mask is implemented in the vacuum system in order to protect the sample surface from ion exposures. In the present work, an additional protection was employed by adding a Ni or Au coating on the top surface. The mask, which was in contact with the sample, was continuously cooled during milling to avoid thermally activated compositional changes in the corrosion products.

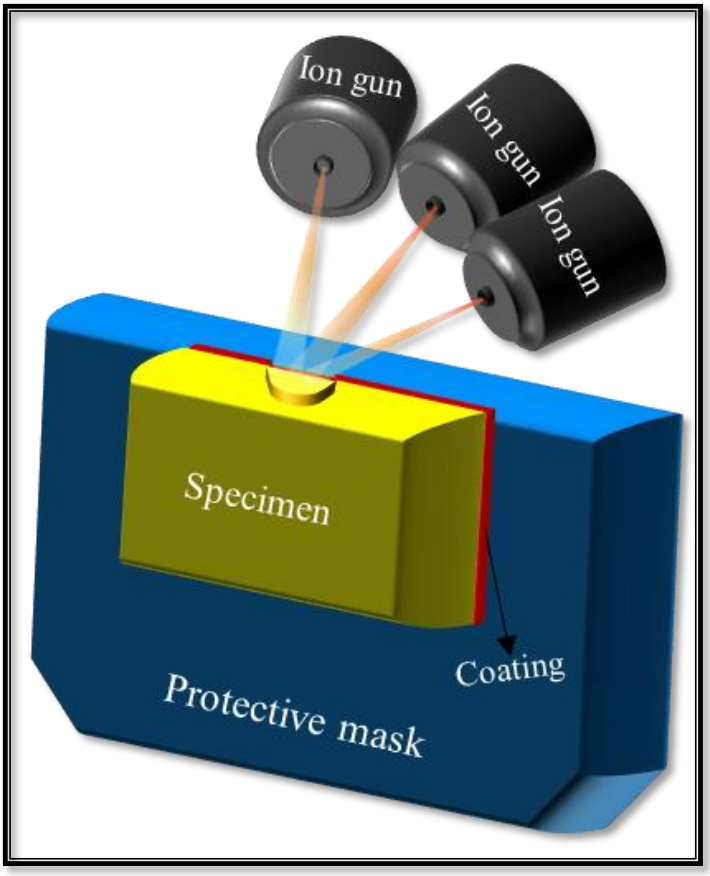

Fig. 20. Schematic illustration of BIB milling system.

4. Results and discussion

4.1. Investigation of the oxide film

4.1.1. Characterization

The surface film formed on CP Mg and on MgAl alloys in humid air and in the absence of NaCl was investigated by XPS. Using Ar^+ sputtering, depth profiles were obtained for polished specimens exposed for 96 h in the absence and in the presence of 400 ppm CO_2, at 22.00°C and 95% RH. To obtain the contribution corresponding to the different chemical states of the elements, the recorded XPS C 1s, Mg 2p and Al 2s photoelectron peaks were curve-fitted using the PHI Multipak software. The C 1s component representing adventitious hydrocarbon contamination was excluded from the depth profiles. Figure 21 (a) and (b) depict the depth profiles of CP Mg in the presence and absence of CO_2, respectively. In both cases, O and Mg^{2+} (Mg compound) were detected on the surface. In the presence of CO_2, carbonate that was confined to a very thin surface layer was also available. . As the analysis probed deeper strata of the film, the Mg^{2+} signal increased, reaching a maximum of 40-45%, at about the depth where the Mg metal peak appeared. The metallic Mg did not show up until after several minutes of ion etching. The CO_2 free exposure required an etching time five times longer than one with 400 ppm CO_2 before the Mg metal appeared. This indicates that the film was thicker in a CO_2 free environment.

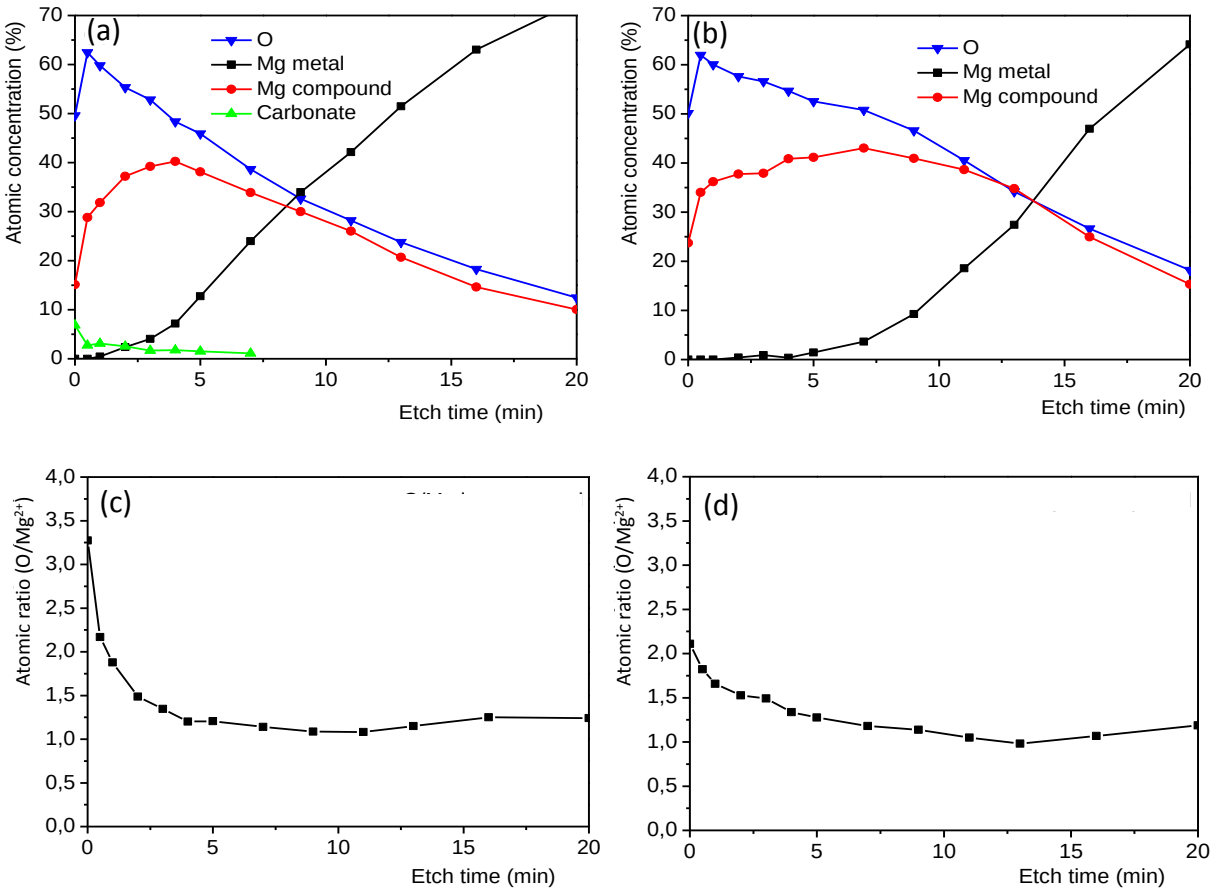

Fig. 21. XPS depth profiles for CP Mg exposed at 95% RH and 22°C for 96 h (a) in the presence and (b) in the absence of CO_2 (Adventitious carbon at the surface has been removed). O/Mg^{2+} ratios for CP Mg (c) in the presence of CO_2 and (d) in the absence of CO_2.

In Fig. 21, (c) and (d) show O/Mg^{2+} atomic ratios for the film formed on CP Mg in the presence and in the absence of CO_2, respectively, calculated from the XPS data. The O/Mg^{2+} ratio at the top of the surface film, formed on CP Mg in the absence and presence of CO_2, was about 2 and 3, respectively. The variations in the ratios are attributed to the presence of different compounds on the film in each case.

Figure 22 shows the C 1s, Mg 2p and Al 2s XPS spectra for alloy AM50 after 96 h exposure at 95% RH and 22°C, in the presence of 400 ppm CO_2 and in the absence of NaCl. As can be seen in Fig. 22 (c), Al^{3+} was detected after 4 minutes of sputtering. At this stage the metallic Al peak had lower intensity compared to Al^{3+}. In the presence of CO_2, Mg^{2+} and carbonate were both detected on top of the surface film. The two peaks were attributed to $MgO/Mg(OH)_2$ and magnesium hydroxy carbonates, respectively. While the Mg^{2+} peak was detected even after long sputtering, the carbonate peak disappeared after 9 minutes of Ar^+ etching. Similar compositional variation was observed in the absence of CO_2, except that no carbonate was detected in this case. The XPS results for alloy AM50 concerning the $MgO/Mg(OH)_2$ and hydroxy carbonate compounds are in good agreement with the aforementioned characterization of the CP Mg surface film.

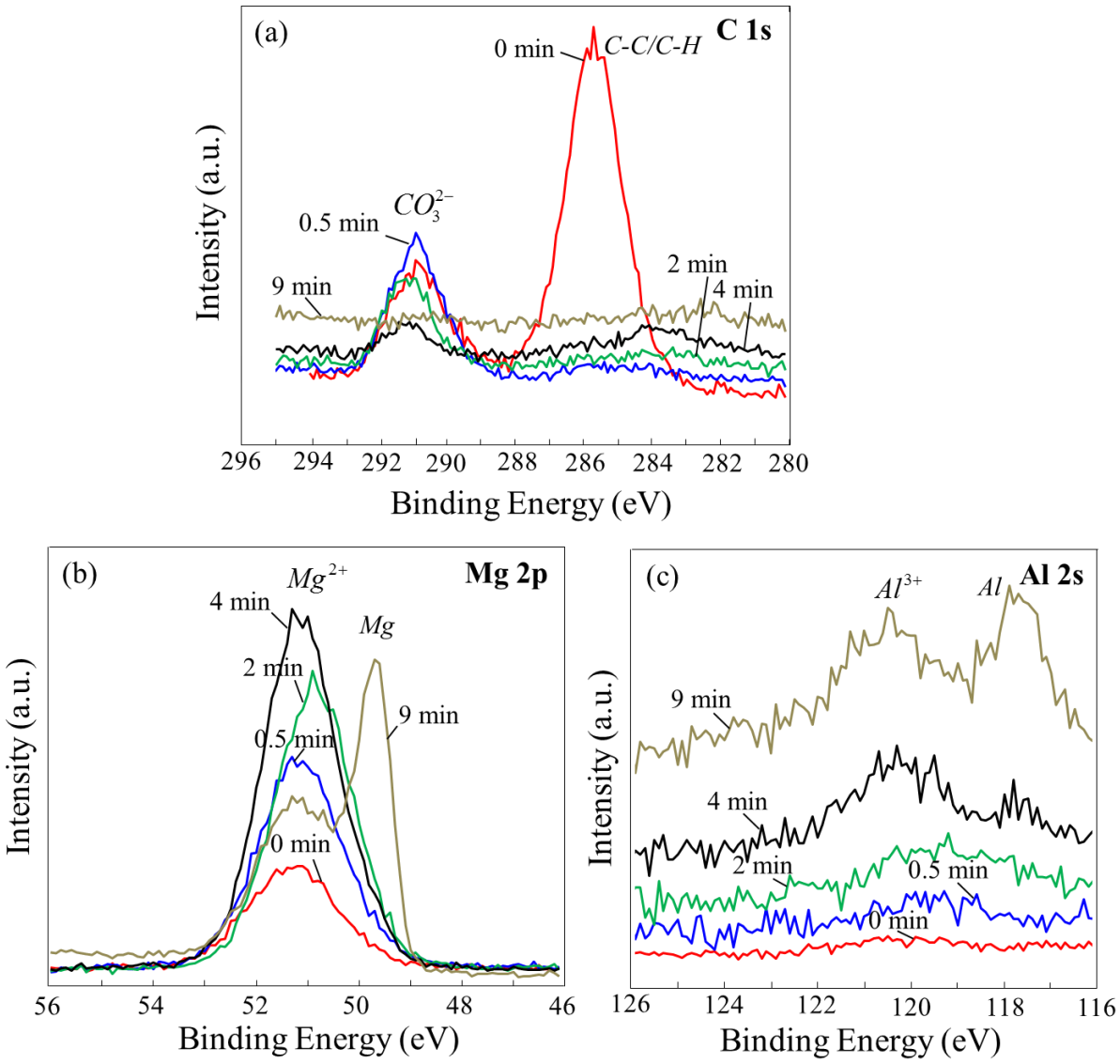

Fig. 22. XPS spectra: (a) C 1s, (b) Mg 2p, (c) Al 2s; for HPDC AM50 exposed in the 95% RH and 22°C, in the presence of 400 ppm CO_2 and in the absence of salt for 96 h.

Figure 23 shows FTIR curves for CP Mg exposed in the presence and in the absence of CO_2. Pure MgO, brucite $Mg(OH)_2$ and dypingite $Mg_5(CO_3)_4(OH)_2{\cdot}5H_2O$ were used as reference materials. In line with the XRD results (not presented here), CP Mg exposed in the absence of CO_2 exhibited a sharp peak at 3702 cm^{-1} that was attributed to brucite. CP Mg exposed in the presence of CO_2 exhibited a peak at the same position but at a lower intensity. The broad absorption peak in the range 3600-3000 cm^{-1} is attributed to OH stretching vibrations in water and hydroxide. The relatively weak peak at about 1650 cm^{-1} is attributed to OH bending vibrations in water. The peaks centered at around 1500 cm^{-1} are attributed to C-O stretching vibrations in carbonate. A comparison with the IR spectra of dypingite and hydromagnesite (the latter from [88]) showed indications for magnesium hydroxy carbonate in all cases. Thus, the peaks at about 580 cm^{-1}, 860, 1490 and 1550 cm^{-1} are tentatively attributed to $Mg_5(CO_3)_4(OH)_2{\cdot}5H_2O$. The observation of carbonate peaks on the sample exposed in the absence of CO_2 is attributed to uptake of CO_2 during measurement.

Using XRD and FTIR, brucite was not detected on the MgAl alloys after 96 h exposure in the absence of CO_2. The lack of evidence for brucite in this case is attributed to the presence of aluminum in the corrosion product film (see Fig. 22). In fact, partial substitution of Al^{3+} for Mg^{2+} in the layered brucite structure results in the formation of MgAl layered double hydroxides (LDHs) with anions intercalated between the positively charged brucite-like layers [100]. Substitution of small amounts of Mg^{2+} by Al^{3+} reportedly results in a broadening of the brucite XRD peak [101] making identification more difficult. Also, Al^{3+} substitution results in hydrogen bonding of the hydroxide ions, explaining the lack of evidence for brucite by FTIR.

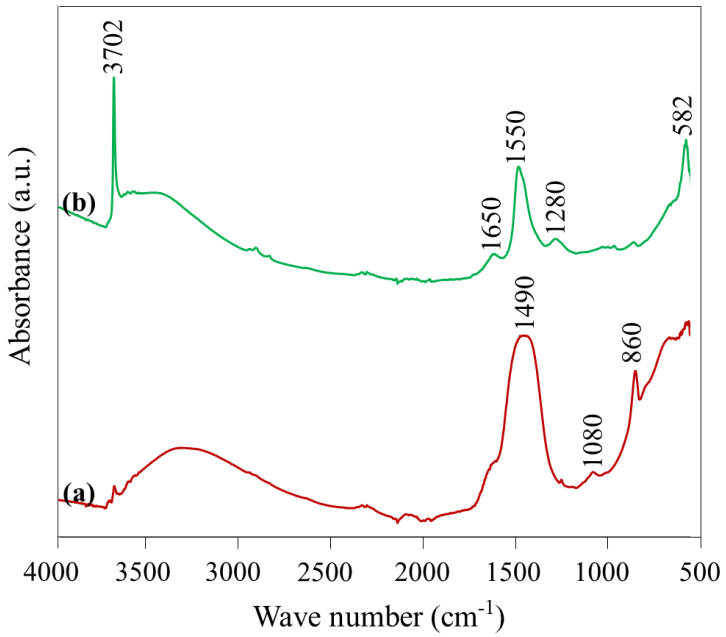

Fig. 23. FTIR curves acquired from CP Mg exposed at 95% RH and 22.00°C for 96 h (a) — in the presence of CO_2, (b) — in the absence of CO_2.

Brucite is known to be a dominant corrosion product on Mg in the absence of CO_2[25]. Magnesium hydroxy carbonates have been reported to be the dominant corrosion products in the presence of CO_2 [88]. However, other corrosion products have been also reported. Table 7 includes a list of compounds reported as corrosion products on Mg and MgAl alloys when exposed in high humidity. Table 7 also presents the respective $O/(Mg^{2+}+Al^{3+})$ atomic ratio for each compound.

Table 7. Atmospheric corrosion products reported in the literature for Mg and MgAl alloys with their respective O/(Mg+Al) ratios.

Reported corrosion product	$O/(Mg^{2+}+Al^{3+})$	Reference
MgO	1	[28, 102, 103]
$Mg(OH)_2$	2	[94, 104-106]
$Mg_6Al_2(OH)_{18}.4.5H_2O$	2.8	[104]
$Mg_5(CO_3)_4(OH)_2.4H_2O$	3.6	[94, 104, 106]
$Mg_5(CO_3)_4(OH)_2.5H_2O$	3.8	[29, 104]
$Mg_5(CO_3)_4(OH)_2.8H_2O$	4.4	[104]
$MgCO_3$	3	[29, 94]
$MgCO_3.3H_2O$	6	[94]
$MgAl_2(OH)_8$	2.6	[29]
$Mg_2(OH)_2CO_3.3H_2O$	4	[105]

Based on observations in the present work and reports in the literature, a schematic generalization is proposed for the compositional variation within the surface film that forms on Mg and MgAl alloys in a high humidity atmosphere in the absence of salts and other pollutants. The schematic is presented in Fig. 24. When exposed to ambient concentrations of CO_2, a magnesium hydroxy carbonate is expected to form on the outermost part of the film. Since hydromagnesite is a thermodynamically stable magnesium hydroxy carbonate [107], an $O/(Mg^{2+}+Al^{3+})$ value of 3.6 may be expected on the top surface. It is suggested that brucite is not completely converted to hydromagnesite, at least initially. Accordingly, as shown in region 1 in Fig. 24 (the blue dashed ellipse), there should be a transition from hydromagnesite (3.6) to brucite (2). As mentioned earlier, MgO that forms on the fresh sample is not expected to completely convert to $Mg(OH)_2$. Hence, there will be a second transition from $Mg(OH)_2$ to magnesium oxide (region 2 in Fig. 24 (the red dashed ellipse)). A plateau region is proposed to come immediately after the second transition (i.e. region 2). Ideally, the plateau would have a $O/(Mg^{2+}+Al^{3+})$ value of 1 corresponding to MgO. However, as mentioned earlier, MgO may be hydrated resulting in a slightly higher $O/(Mg^{2+}+Al^{3+})$ value. The XPS results of the present work for the alloys suggest the presence of Al, especially in the bottom of the film. It has been reported that in the case of MgAl alloys an Al-rich layer is present at the oxide-metal interface [108]. Assuming an enrichment of Al at the interface, a rise at the end of the curve in Fig. 24 is expected (see region 3 in Fig. 24 (the green dashed ellipse)). In addition, Nordlien et al. reported that extended exposure of Mg to humid air causes a hydrated region to form between the initially formed dense MgO layer and the metal [103]. Such a hydrated region might also be reflected in a rise of the curve in Fig. 24 after the plateau region.

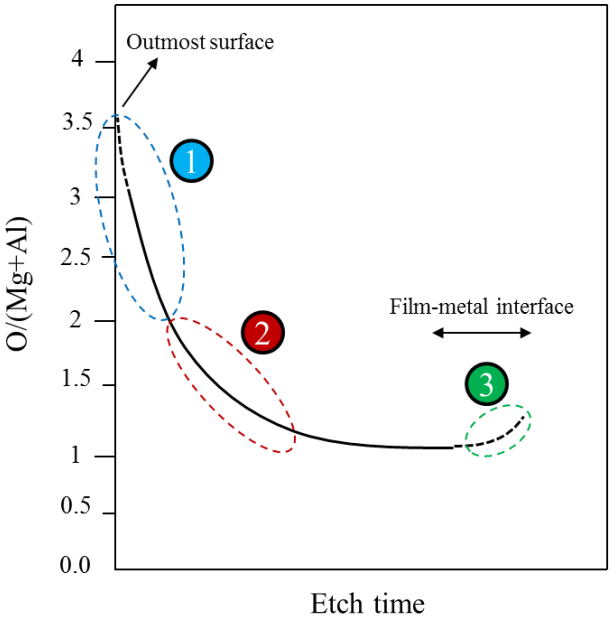

Fig. 24. Schematic proposal for the compositional variation within the surface film formed on Mg and MgAl alloys after exposure in a high humidity atmosphere.

4.1.2. Formation and growth

When exposed to dry air or oxygen, metals form an oxide film. The film formation was described using the Cabrera-Mott field-assisted cation transport mechanism and the growth of the film was fitted to a logarithmic relation [109]. Do et al. [110] showed that a Cabrera-Mott type MgO film forms on Mg in the presence of water vapor or humid air. For both Mg [110] and MgAl alloys [111], a three-stage process was proposed describing the formation and growth of the oxide film. Stage one included dissociative water adsorption at low exposures (up to ~0.7 L[4]). Stage two included fast oxide island nucleation and growth, up to ~5 L exposure. Eventually, in the third stage, the bulk oxide film grew in very high exposures. Stage three was described by inverse logarithmic kinetics. It should be noted that the first two stages of film formation and growth at low exposures was carried out by AES and XPS analysis (film thickness about 1 nm). Also, the third stage (bulk oxide thickening) was performed in laboratory air at 294 K and 50-65% RH (film thickness about 4 nm).

The formation of the MgO film is not the focus of the present work. However, the growth of the film was studied to some extent. The XPS results showed that the surface film formed in the absence of CO_2 consisted of a hydrated MgO bulk and magnesium hydroxide top layer with a total thickness of approximately 10 nm implying that the original Cabrera-Mott film present before exposure has grown. It should be noted that in the presence of CO_2 the total thickness of the film was in about 2 nm (paper IV).

4.1.2.1. MgO film growth by chemical reaction between Mg and $Mg(OH)_2$

Figure 25 illustrates the hydration of the MgO film. As shown in Fig. 25, a MgO film is present in dry air. When exposed to water vapor, the MgO surface chemisorbs water as presented in

[4] The langmuir (L) is a unit of surface exposure used in ultra-high vacuum studies (1 L = 1.33×10^{-4} Pa·s).

reactions (18)–(21). Refson et al. showed that water chemisorption is favored on MgO (111) surface rather than on a (001) surface [112]. Adsorbed water is subjected to autoprotolysis and OH^- and H^+ form (reaction (19)). Surface hydroxylation of MgO occurs transporting it to $Mg(OH)_2$. One OH^- group comes from autoprotolysis reaction and the other OH^- group is resulted from the reaction of H^+ from autoprotolysis and O^{2-} from MgO (reaction (20)).

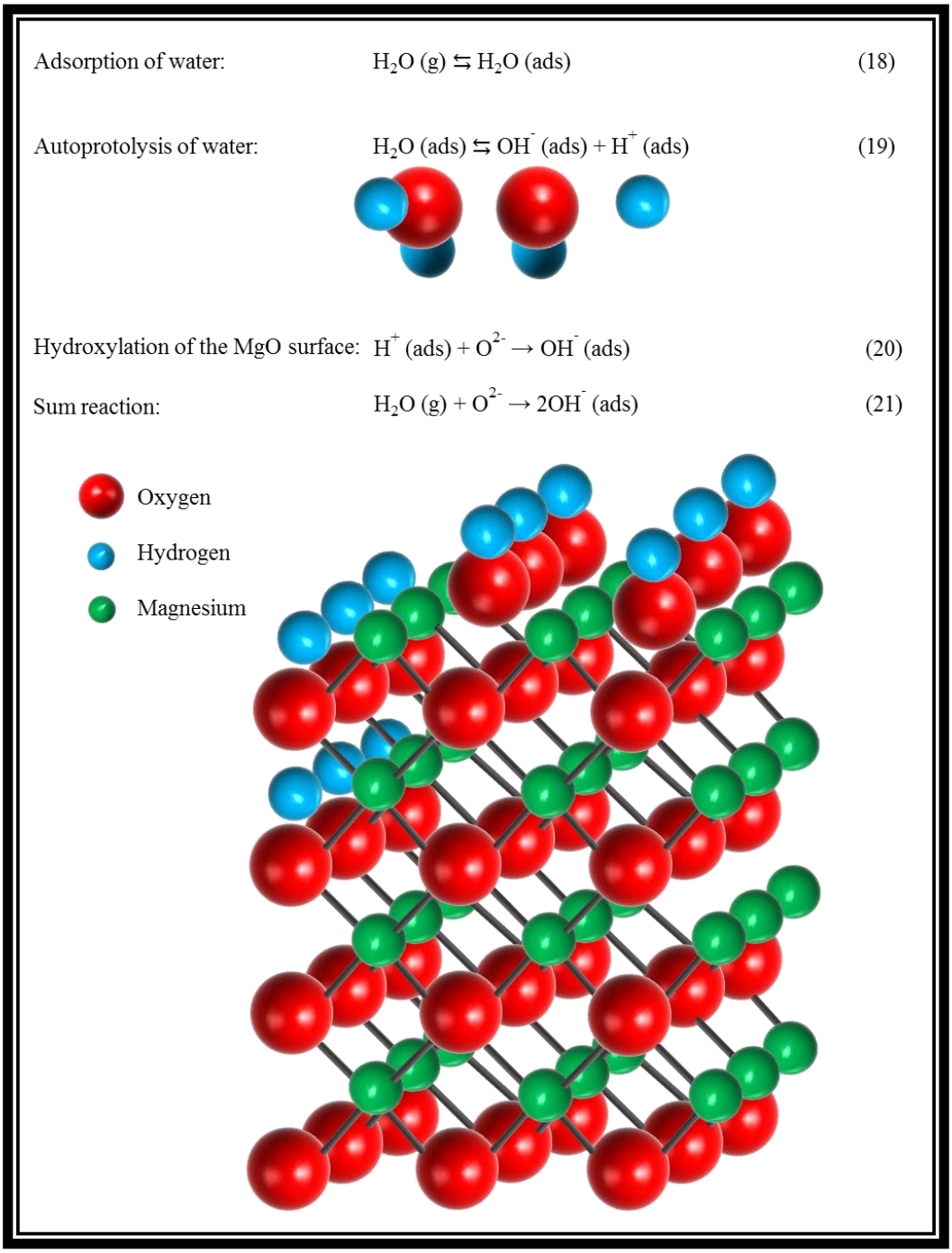

Fig. 25. Schematic illustration of the hydroxylation of the MgO (111) surface.

Figure 26 illustrates the thickening of the oxide film through a hydration mechanism. Also, in Fig. 26 the dissolution-precipitation mechanism is illustrated (see the following section). As mentioned above, the surface is already hydroxylated when exposed to the high humidity

environment. It is proposed that H_2O reacts with MgO, not only at the surface but also at grain boundaries (gb)s in the MgO film. In this way hydroxide decorates the MgO (gb) all the way to the metal-film interface. At the metal-film interface, $Mg(OH)_2$ (gb) reacts with the metal forming MgO and H at the interface (see reaction (22)). Hence, the film grows by a chemical reaction. The H produced can dissolve in the metal (see reaction (23)) or result in the generation of H_2 gas (see reaction (24)). The H_2 gas generated might crack the film on its way out (see Fig. 27 (a)). Using secondary ion mass spectroscopy (SIMS) technique, Unocic et al. [113] revealed that H penetrated the surface film to the underlying metal for MgAl alloy AZ31B (~3 wt.% Al and ~1 wt.% Zn) exposed for 24 h in de-ionized water at room temperature.

While the conversion of crystalline MgO to $Mg(OH)_2$ is thermodynamically favored under ambient conditions [114], the reaction is reported to be slow. Thus, Birchal et al. [115] reported that while the conversion of MgO (powder and single crystal) to $Mg(OH)_2$ in contact with liquid water and water vapor is initially rapid, it slows down quickly , resulting in incomplete conversion to $Mg(OH)_2$ even after long exposure times. However, the presence of MgO even after long exposures is not necessarily due to the slow conversion of MgO to $Mg(OH)_2$. Instead fresh MgO is formed at the metal-film interface by reaction between $Mg(OH)_2$ (gb)and Mg (reaction 22).

The thickening of the film by reaction between $Mg(OH)_2$ (gb)and Mg (reaction 22) may depend on the exposure temperature and the grain size of the film. Thus, higher temperature and smaller grain size (higher fraction of grain boundaries) are expected to increase the rate of reaction.

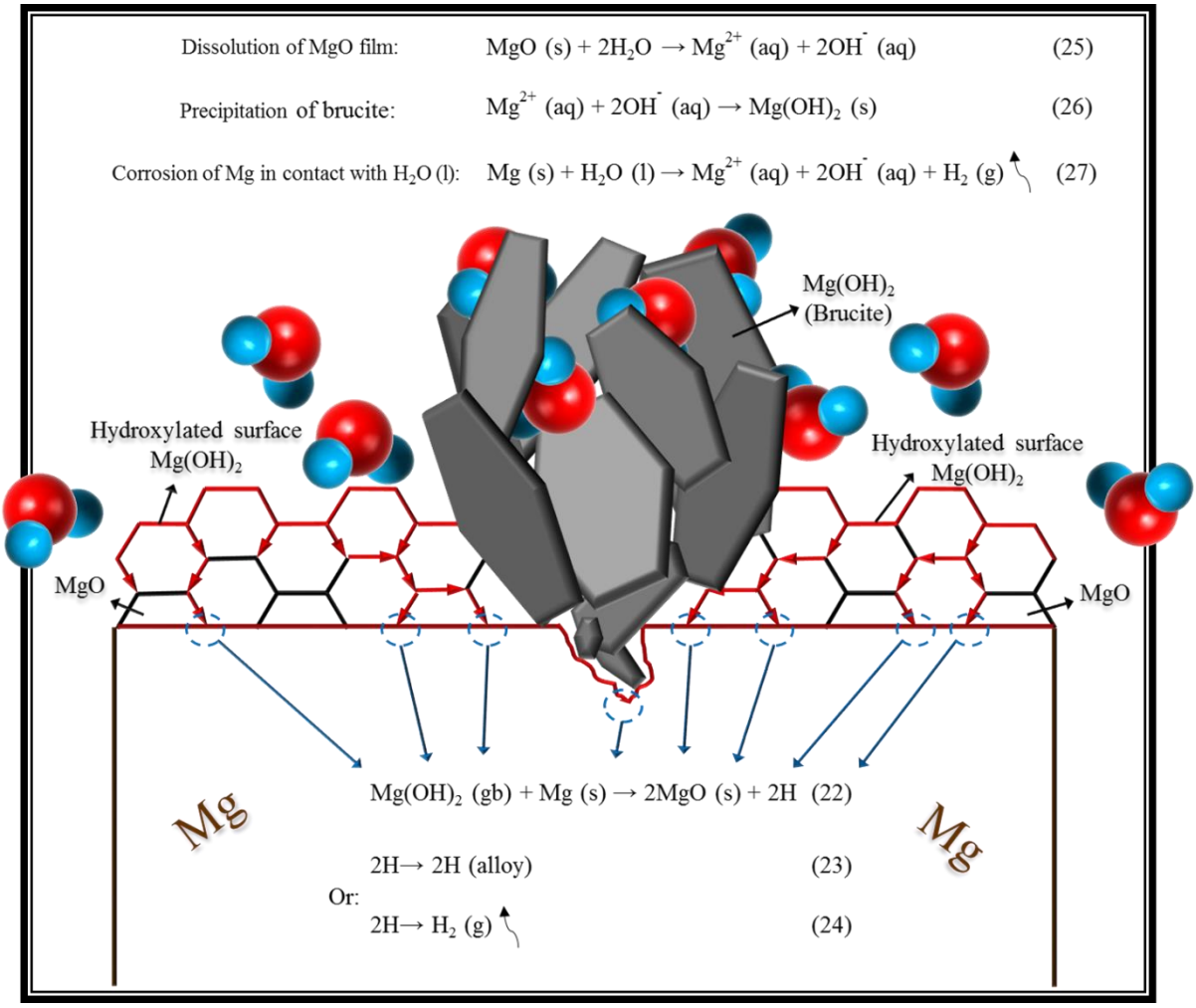

Fig. 26. Schematic illustration of the hydration mechanism and dissolution-precipitation mechanism.

4.1.2.2. Dissolution-precipitation

As noted above the air formed MgO/$Mg(OH)_2$ film grows continuously. As the film becomes thicker, the diffusion of water through the film in the form of $Mg(OH)_2$ (gb) slows. The plan-view and cross-sectional SEM images (see Fig. 27) showed localized corrosion features on the Mg surface in the form of nodules and filaments that were typically couple of microns thick. This localized corrosion suggests that another corrosion mechanism has been active in addition to the chemical reaction described above.

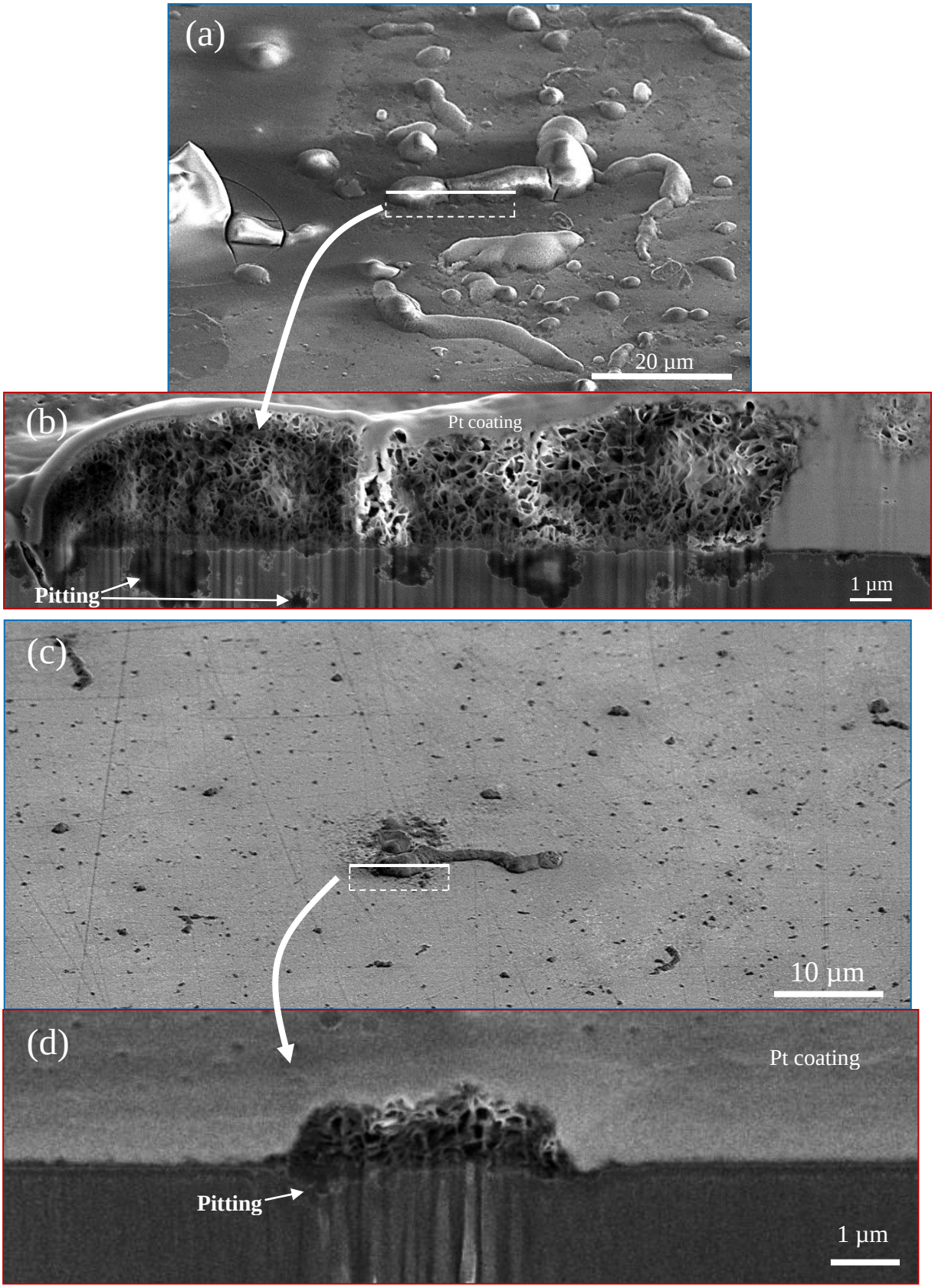

Fig. 27. Plan-view (tilted surface) and cross-sectional SE micrographs demonstrating corrosion features in the form of nodules and filaments, (a) & (b) in the presence of 400 ppm CO_2 and (c) & (d) in the absence of CO_2.

It is proposed that localized corrosion is caused by a dissolution-precipitation mechanism resulting in film thinning. As discussed above (see section 2.2.1.), at 95% RH there is be about 10 layers of water (~3 nm thick) adsorbed on the sample surface on top of the Cabrera-Mott oxide film (2-4 nm [110]). The adsorbed water layer is assumed to be liquid-like. Accordingly, MgO can dissolve in it, generating Mg^{2+} ions (see reaction (25)). However, due to the small volume of water, it can only dissolve a very small amount of MgO. Where the film is thin enough water can react directly with the bulk metal (see reaction (27)), releasing more Mg^{2+} in the solution. It may be noted that MgO is significantly more soluble than brucite. Thus, K_{sp} MgO = $1\times10^{-6.33}$ while K_{sp} $Mg(OH)_2$ (brucite) = $1\times10^{-11.16}$. In addition, the hydrated solid MgO (i.e. $Mg(OH)_2$) is not identical to brucite [102]. Thus, according to Grauer [116], the magnesium hydroxide surface layer resulting from the hydration of solid MgO is significantly more soluble than brucite with K_{sp} = $1\times10^{-9.2}$. This implies that an aqueous solution that is saturated with respect to the MgO/Mg(OH)2 film is *super-saturated* with respect to brucite. As a result, brucite crystallites can nucleate from the solution (see reaction (26)).

The MgO dissolution is favored around the brucite nuclei. In the other words, a correlation between the source and the sink sites is expected. Also, reports indicate [117-119] that MgO is attacked preferentially by water at the sites of low coordination (i.e. <5-fold).

When exposed to ambient levels of CO_2, film dissolution is assisted by the acidity of this gas. As a result reaction (25) and (27) are favored.

$$CO_2(aq) + OH^-(aq) \rightarrow HCO_3^-(aq) \quad (28)$$

$$HCO_3^-(aq) + OH^-(aq) \rightarrow CO_3^{2-}(aq) + H_2O \quad (29)$$

Consequently, the protective $MgO/Mg(OH)_2$ layer is thinned. The thinner surface film in the presence of 400 ppm CO_2 can also be explained in a different way. As described earlier, in order for the film to grow, water needs to reach the MgO on the surface and the grain boundaries. Hence, film growth may slow since other species compete with water for adsorption on MgO. In fact, Allen et al. reported a competition between the reactive dissociative adsorption of H_2O and the chemisorption of CO_2 for some MgO surfaces [120]. This is in line with the presence of higher fraction of localized corrosion product features in the presence of CO_2 compared to the CO_2-free exposures as can be seen in the micrographs of Fig. 27. However, the formation of a magnesium hydroxy carbonate surface layer appears to slow corrosion after longer exposure times [105]. The inhibitive role of CO_2 in long-term corrosion of Mg has been attributed to the formation of hydromagnesite (or similar magnesium hydroxy carbonates) on top of the hydrated MgO ($Mg(OH)_2$) film (see reaction (11)).

4.2. NaCl-induced atmospheric corrosion

4.2.1. Influence of NaCl on the corrosion of Mg

As mentioned above, the $MgO/Mg(OH)_2$ surface film protects Mg and MgAl materials against corrosion. Hence, corrosion occurs when this film is partially (pitting corrosion) or totally (general corrosion) removed. MgO is soluble in water. Aqueous solution in contact with metal

Mg results in electrochemical corrosion of the metal (section 2.1.1.). Hence, the conductivity of the electrolyte plays a significant role in the rate of corrosion.

As mentioned above, saturated salt solutions are in equilibrium with air with a certain RH. In the presence of NaCl, water condensation is expected at RH>76%. Accordingly, at e.g. 95% RH there is a significantly greater volume of water in the presence of salt compared to the thin layer of adsorbed water forming on a clean metal surface. When dissolved in water, NaCl forms Na^+ and Cl^- ions that increase the conductivity of the solution due to the larger amount of water. Thinning of the passive film accelerates and corrosion occurs with anodic dissolution of Mg and hydrogen evolution.

Figure 28 shows the average metal loss for the NaCl induced corrosion of CP Mg in the presence and in the absence of 400 ppm CO_2, at 95% RH and 22 °C for 24, 168 and 672 h. The figure also presents the metal loss of CP Mg exposed in the absence of NaCl. As expected, corrosion rate increased as the NaCl amount increased.

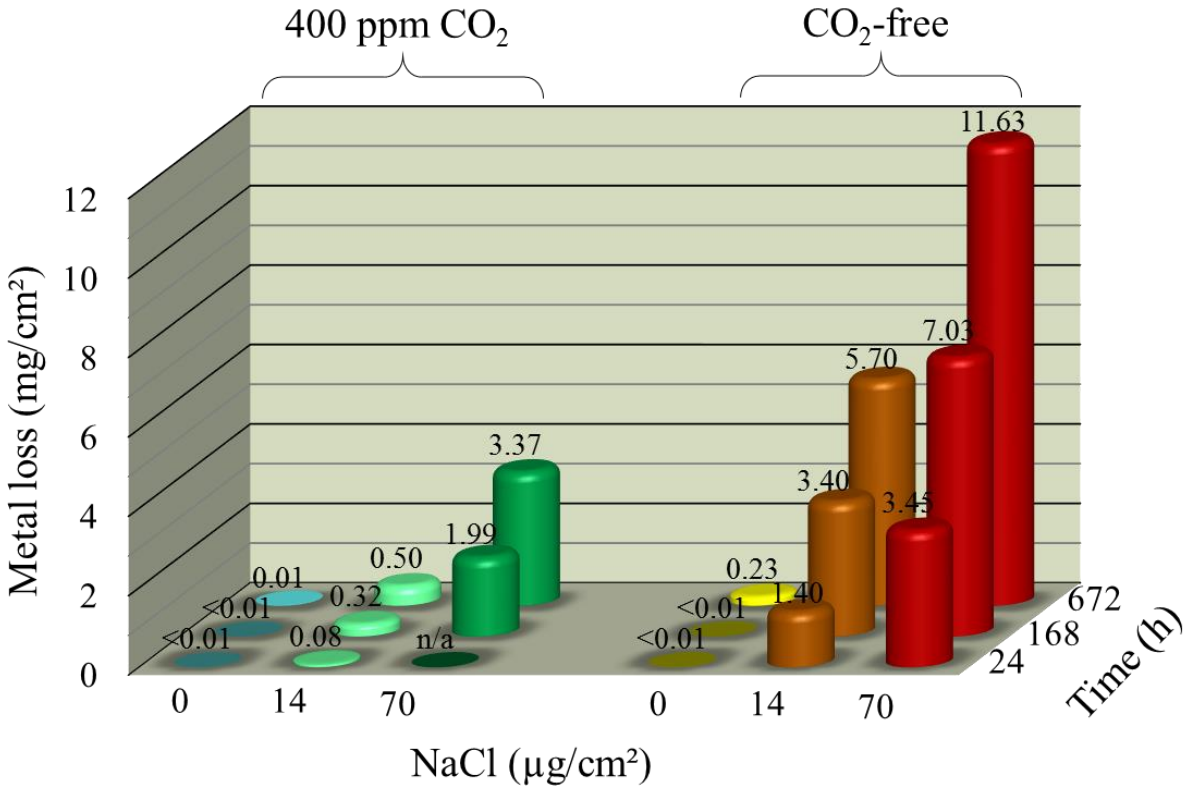

Fig. 28. Average corrosion of CP Mg exposed in the presence and in the absence of CO_2, in the presence of 14 and 70 µg/cm² NaCl and in the absence of salt for 24, 168 and 672 h at 95% RH and 22°C.

4.2.2. Influence of CO_2 on the NaCl-induced corrosion of Mg

As can be seen in Fig. 28, NaCl induced corrosion was more severe in the absence of CO_2 in comparison to when CO_2 was present. In addition, CP Mg samples exposed for 672 h without NaCl showed similar behavior. This contradicts the observation that CO_2 accelerates pitting corrosion in the initial stage of corrosion. However, as argued at the end of section 4.1., a

hydroxy carbonate film forms that covers and protects the metal surface. Complete coverage of the surface with carbonate film (i.e. conversion of $Mg(OH)_2$ to hydromagnesite) is not expected to occur in the early stages of corrosion since reaction (11) ($5Mg(OH)_2(s) + 4CO_2(aq) \rightarrow Mg_5(CO)_3(OH)_2 \cdot 4H_2O(s)$) is known to be relatively slow [121]. Nevertheless, in prolonged exposures in the absence of salt, CO_2 inhibits corrosion. The protective properties of the hydromagnesite film have been attributed to its lower solubility compared to MgO and $Mg(OH)_2$ [105, 122].

During aqueous corrosion of Mg, hydrogen evolution is the dominating cathodic reaction. According to reaction (3) ($2H_2O + 2e^- \rightarrow H_2(g) + 2OH^-(aq)$), pH increases at the cathodic sites, resulting in a pH gradient on the surface. Such pH gradient favors the localization of corrosion and development of corrosion cells. Hence, brucite is insoluble close to cathodic regions. The XRD results showed that brucite and hydromagnesite were the dominating corrosion products in the absence and in the presence of CO_2, respectively. In the latter case, brucite was also identified. This can be attributed to a relatively slow conversion of brucite to hydromagnesite. In the presence of CO_2, the cathodic alkalinity is neutralized by carbonic acid (see reaction (7)), and the corrosion cells become smaller compared to CO_2-free exposures. Thus, in the presence of CO_2, the corrosion products tend to cover the whole surface. Also, as mentioned before, in the presence of 400 ppm CO_2 at 95% RH and 22°C, hydromagnesite is less soluble than brucite, which mean the surface layer in the presence of CO_2 is more stable compared to the one that formed in the absence of CO_2.

4.2.3. Corrosion of MgAl alloys

4.2.3.1. MgAl alloys versus CP Mg

The atmospheric corrosion of MgAl alloys was investigated and compared to that of CP Mg. Alloys HPDC AM50 and DC AZ91 with 5 wt.% and 9.4 wt.% of Al (see Table 6) were investigated. The choice of casting route does not affect the comparison of alloy AM50 with alloy AZ91 in this section. In fact, the difference in the Al concentration was large enough to result in quite different microstructures, especially regarding the β-phase distribution (the microstructure of the two alloys will be discussed below). Hence, the microstructure of DC AZ91 that was investigated in the present thesis is similar to the microstructure of the HPDC AZ91 reported in the literature [38, 123]. In this section, the NaCl-induced corrosion will be discussed only for samples exposed in the presence of 70 µg/cm² NaCl for 672 h. For a more comprehensive comparison with of different NaCl concentrations and with different exposure times, please see paper II in this thesis.

Figure 29 shows the BSE micrographs presenting the polished surfaces of alloys AM50 and AZ91. As expected, the alloys consisted of α-Mg grains and $Mg_{17}Al_{12}$ (β-phase) and Al_8Mn_5 (η-phase) intermetallic particles. In the case of alloy AZ91, SEM-EDX showed that Zn was accumulated in the β-phase. As can be seen in Fig. 29 (b), β particles formed a semi-continuous network in the case of alloy AZ91 while they were more dispersed and had a lower area fraction in alloy AM50.

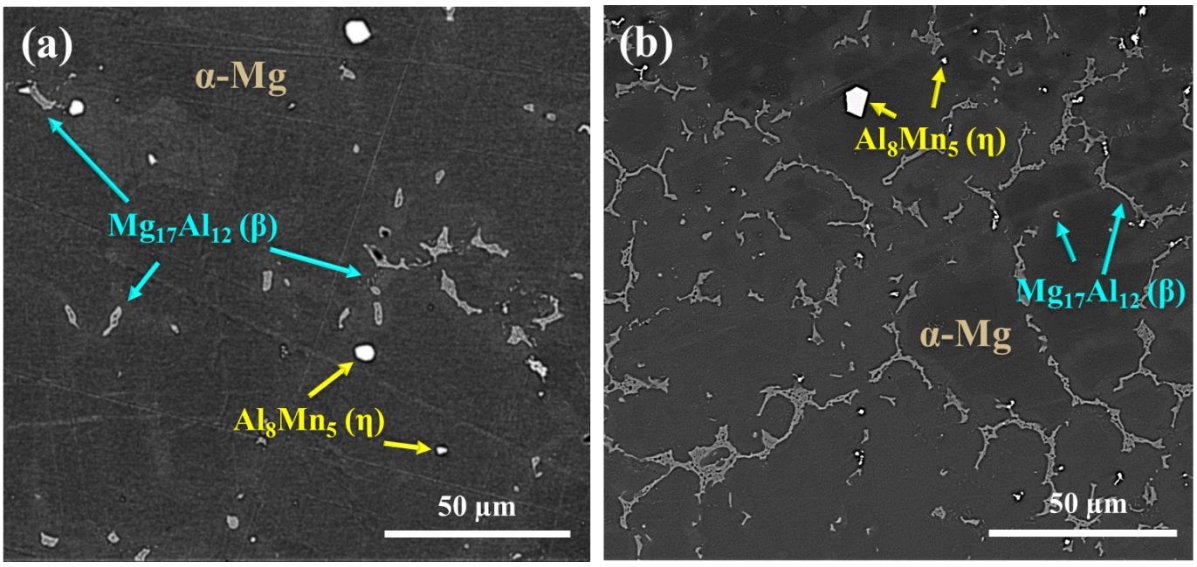

Fig. 29. BSE micrographs of polished surfaces of (a) alloy HPDC AM50 and (b) alloy DC AZ91.

Table 8 shows gravimetry results for CP Mg, alloy AM50 and alloy AZ91 after 672 h exposure at 95% RH and 22°C in the presence and in the absence of CO_2, with 70 µg/cm² NaCl. The average dry mass gain decreased in the order CP Mg > HPDC AM50 > DC AZ91 both in the presence and in the absence of CO_2. The corrosion rate of CP Mg was ~7 times greater compared to HPDC AM50 and ~18 times greater than that of DC AZ91 when exposed in the absence of CO_2. In the presence of CO_2, the corrosion rate of CP Mg was ~4 times greater than that of HPDC AM50 and ~13 times greater than that of DC AZ91.

Table. 8. Comparison of gravimetry results for CP Mg, HPDC AM50 and DC AZ91 after exposure in the presence of 70 µg/cm² NaCl for 672 h.

CO_2 (ppm)	Average dry mass gain (mg/cm²)			Average metal loss (mg/cm²)			Corrosion rate (µm/year)		
	CP Mg	HPDC AM50	DC AZ91	CP Mg	HPDC AM50	DC AZ91	CP Mg	HPDC AM50	DC AZ91
400	6.80	2.41	0.88	3.37	0.96	0.28*	252	70	20*
0	17.45	2.76	1.06	11.63	1.62	0.665	871	119	48

** In the case of alloy DC AZ91, the average metal loss was calculated using the corrosion product composition of HPDC AM50 in the same study.*

The higher corrosion resistance of AM50 and AZ91 alloys compared to CP Mg is explained by the presence of Mn and Al in the alloys. As mentioned in section 2.1.2., elements such as Fe dissolve in the η-phase. This prevents them from forming cathodically active intermetallics such as $FeAl_3$ [45]. In fact, Fe was occasionally detected in η particles by means of SEM-EDX. The alloys investigated in the present thesis were of high purity and the impurity level was below the respective "tolerance limit". The β-phase has been argued to have a protective role in corrosion (see section 2.4.1.). Such protection is expected to be efficient when a semi-continuous network of β intermetallics is present. Finally, the presence of Al in α solid-solution grains is expected to result in the presence of alumina in the surface film, which can provide a more protective passive layer.

The corrosion morphology of CP Mg and the alloys, in the presence and in the absence of CO_2, was investigated using SEM. Figure 30 (a) and (b) shows that the whole surface of CP Mg was covered by corrosion products both in the presence and in the absence of CO_2. In the case of the alloys, the corrosion attack was less severe. It can be seen in Fig.s 30 (c)-(d) that the corrosion cells were significantly larger in the absence of CO_2 compared to 400 ppm CO_2 exposures.

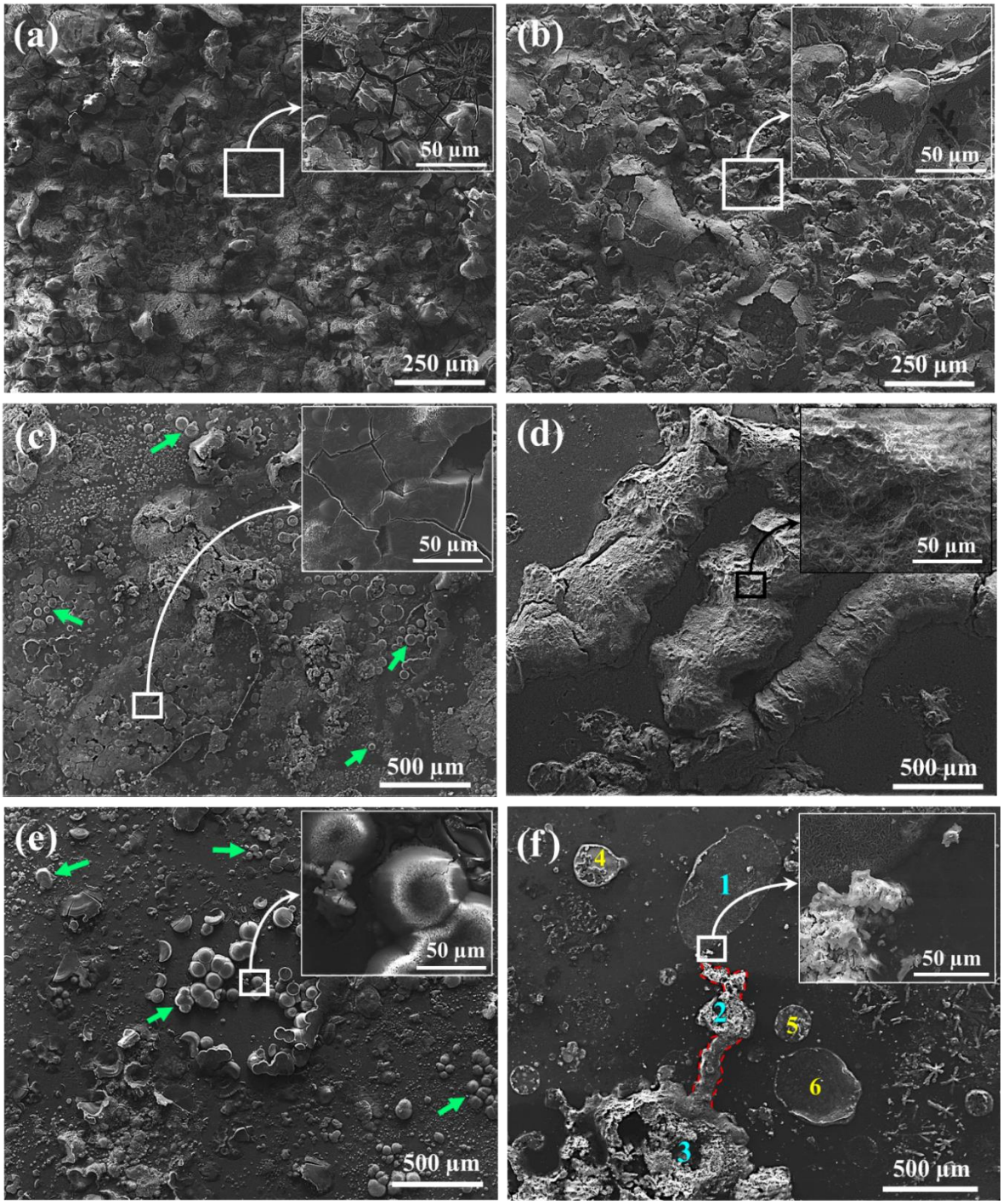

Fig. 30. SE micrographs showing the corrosion morphology of materials exposed at 95% RH and 22°C, in the presence of 70 µg/cm² NaCl for 4 weeks; (i) in the presence of CO_2: (a) CP Mg, (c) HPDC AM50, (e) DC AZ91 and (ii) in the absence of CO_2: (b) CP Mg, (d) HPDC AM50, (f) DC AZ91. The inserts show selected regions at a higher magnification.

Similar to CP Mg, for alloys, brucite was detected by XRD as the dominating corrosion product in the absence of CO_2. However, meixnerite $Mg_6Al_2(OH)_{18}\cdot 4.5H_2O$ (also reported as $Mg_6Al_2(OH)_{18}\cdot 4H_2O$ [101]) was also detected in the alloys. Meixnerite belongs to the class of LDHs. Meixnerite formation is attributed to the high pH developed at the cathodic sites. This formation initiates the dissolution of alumina in the passive layer and formation of aluminate.

$$Al(OH)_3(s) + OH^- \rightarrow Al(OH)_4^-(aq) \quad (30)$$

Aluminate reacts with brucite, forming meixnerite:

$$2Al(OH)_4^-(aq) + Mg^{2+}(aq) + 5Mg(OH)_2(s) + 4.5H_2O \rightarrow Mg_6Al_2(OH)_{18}\cdot 4.5H_2O(s) \quad (31)$$

On the other hand, in the presence of 400 ppm CO_2, magnesium hydroxy carbonates were the dominating corrosion products. The conversion of magnesium hydroxide to hydroxy carbonate is described by reaction (11). The absence of meixnerite in the presence of CO_2 is due to the neutralization of the surface electrolyte by CO_2.

As described earlier, the passive layer formed on the alloys consisted of $Mg(OH)_2$/MgO and a small amount of Al^{3+}. $Mg(OH)_2$/MgO passive films are stable in high pH while alumina passive films are stable in neutral pH. See the Pourbaix diagrams in Figs. 1 and 5. In the absence of CO_2, pH increases dramatically in the cathodic regions, leading to dissolution of alumina. However, alumina remains in the passive film at the anodic sites, which slows down the anodic reaction (reaction (1)) and improves the corrosion of the alloys in the absence of CO_2 compared to the corrosion of CP Mg.

4.2.3.2. Influence of the casting route

The effect of SSC on the atmospheric corrosion of MgAl alloys AM50 and AZ91 was studied by comparing RC AM50 and RC AZ91 with HPDC AM50 and DC AZ91, respectively. Table 9 shows the gravimetry data for the RC materials after exposure at 95% RH and 22°C, in the presence of 70 µg/cm² NaCl and in the presence and absence of CO_2 for 672 h. The results of Table 9 can be compared to those in Table 8. For alloy AM50, the corrosion rate was lower when the material was prepared using RC rather than by conventional HPDC. The improved corrosion behavior was especially pronounced in the presence of CO_2.

Table 9. Comparison of gravimetry results for RC AM50 and RC AZ91 after exposure in the presence of 70 µg/cm² NaCl for 672 h.

CO_2 (ppm)	Average dry mass gain (mg/cm²)		Average metal loss (mg/cm²)		Corrosion rate (µm/year)	
	RC AM50	RC AZ91	RC AM50	RC AZ91	RC AM50	RC AZ91
400	1.59	0.83	0.57	0.28	42	20
0	2.53	1.26	1.58	0.789	115	57

Figure 31 shows BSE micrographs of polished surfaces of RC AM50 and RC AZ91. The general microstructure of both AM50 and AZ91 materials was similar in the RC and HPDC/DC states. However, since the composition of the two alloys is the same, the microstructure should

be responsible for the differences in corrosion resistance. As discussed earlier, the Al content of the matrix and the β-phase distribution probably affect the corrosion of MgAl alloys. Thus, a more detailed investigation was performed where the Al concentration of the α-grains (measured at the center of the grains) and the fraction of β-phase was compared for both alloys prepared by different casting techniques. The measurements were averaged over 10 regions, on each material. Each region had a surface area of 0.026 mm^2. The results are presented in Table 10. The materials with higher fraction of β are accompanied with α-grains with lower Al concentration. The fraction of β-phase is considerably higher in alloy AZ91 than that of alloy AM50. However, no significant difference is observed in the Al concentration of α-grains in alloy AZ91 compared to alloy AM50.

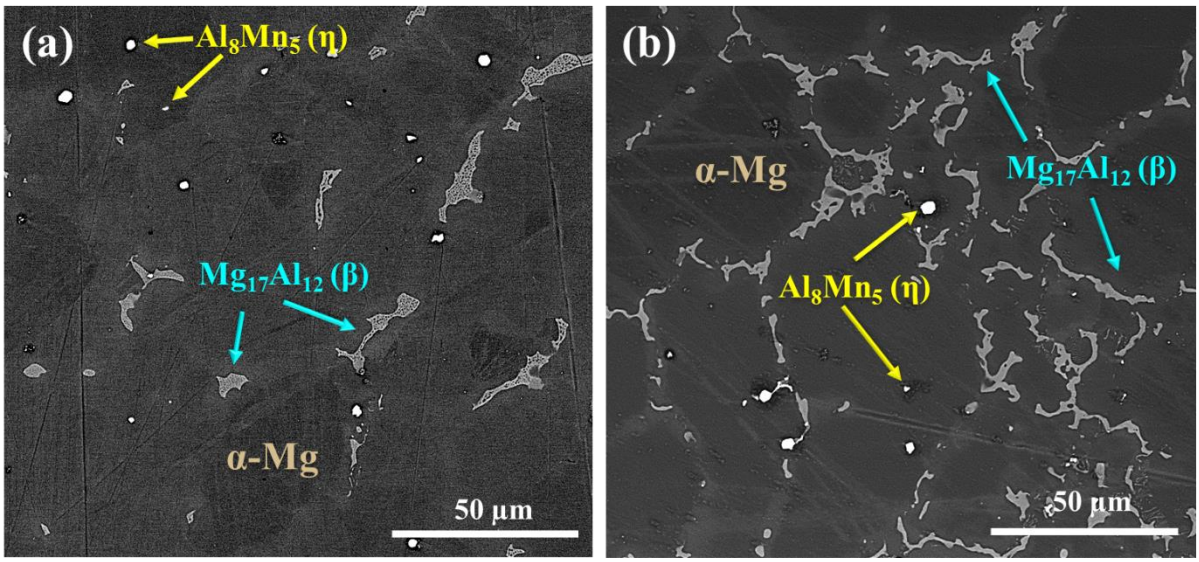

Fig. 31. BSE micrographs of polished surfaces of (a) alloy RC AM50 and (b) alloy RC AZ91.

Table 10. Area fraction of β-phase and Al content of α-Mg.

Alloy	Al content (wt.%)	Avg. β area fraction %	Standard error %	Avg. Al in α-Mg (wt.%)	Standard error (wt.%)
DC-AZ91	9.4	7.6*	0.8	2.9	0.1
RC-AZ91		7.2*	0.5	3.1	0.1
HPDC-AM50	5.0	1.3*	0.2	2.6	0.1
RC-AM50		2.1*	0.3	1.9	0.1

* *The measurements were performed on 10 regions on each material, each region having a surface area of 0.026 mm^2.*

Figure 32 shows BSE cross-sectional micrographs acquired from alloy RC AZ91 after exposure in the presence of 70 µg/cm² NaCl, in the presence and in the absence of CO_2. Both images (i.e. Fig. 32 (a) and (b)) illustrate the presence of β- and η-phase in the vicinity of the pits. Moreover, the progression of the corrosion pits ceased as they reached the particles, particularly β. Similar observations were reported for the corrosion of alloy AZ91 in bulk water [91]. It may be worth mentioning that between the two alloys RC AZ91 and DC AZ91; after exposure in the absence of CO_2, a slightly lower corrosion rate was measured for the one with a higher fraction of β (and lower Al in the α-grain).

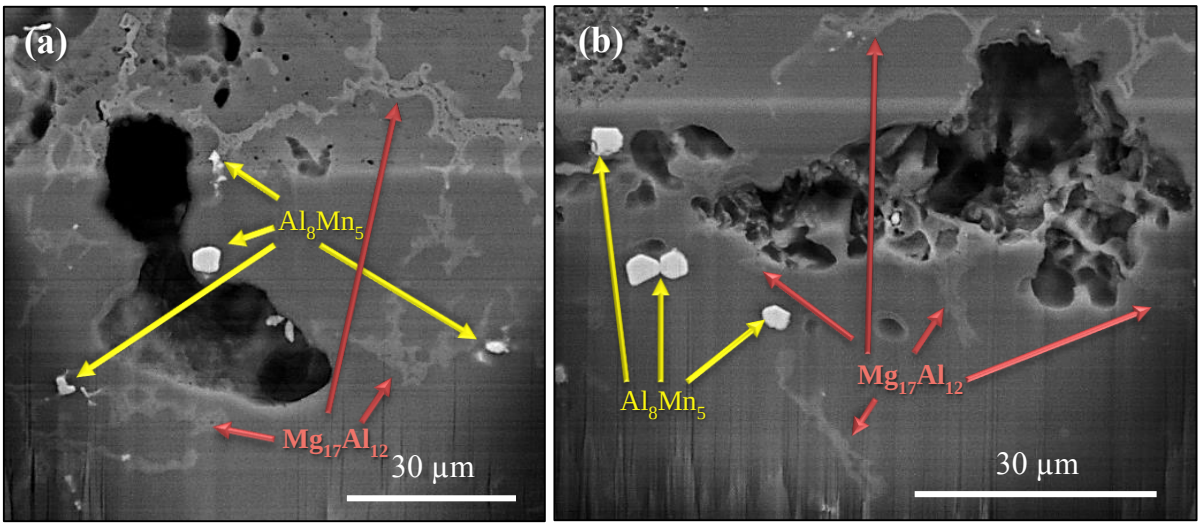

Fig. 32. BSE cross-sectional micrographs for alloy AZ91 after removal of the corrosion products. The samples had been exposed in the presence of 70 µg/cm² NaCl (a) in the presence and (b) in the absence of CO_2.

The role of β-phase as a physical barrier against corrosion was more pronounced for alloy AZ91 than for alloy AM50. However, after exposure in the presence and in the absence of CO_2, a lower corrosion rate was measured for RC AM50 with a higher fraction of β (and lower Al in the α-grain) compared to HPDC AM50 exhibiting lower fraction of β (and higher Al in the α-grain). This is analogous to the observations of alloys RC AZ91 and DC AZ91 in the absence of CO_2. Thus, it is proposed that at least in the aforementioned cases; the **positive** influence of *the increase in the fraction of β-phase* outweighed the **negative** influence of *the decrease in the Al content of the α-grains*.

Considering the micrographs in Fig. 32 and knowing that the β-phase forms in the interdendritic region, it might be concluded that an α-grain is protected more efficiently by *elongated* rather by *rounded* β-phase particles. In other words, a higher aspect ratio of an individual β particle is preferred. This might be more important in the case of alloy AM50, where no network of β-phase is expected. In order to measure the aspect ratio, individual β-particles, formed in alloy AM50, were inscribed in ellipses and the ratio of the major (transverse) diameter of an ellipse to its minor (conjugate) diameter was calculated. Figure 33 shows the distribution graph of the average aspect ratio of β-particles in the RC and HPDC alloys. In both RC and HPDC materials, the frequency of the β-particles decreased as the corresponding aspect ratio increased (see the frequency bar chart in purple, Fig. 33).

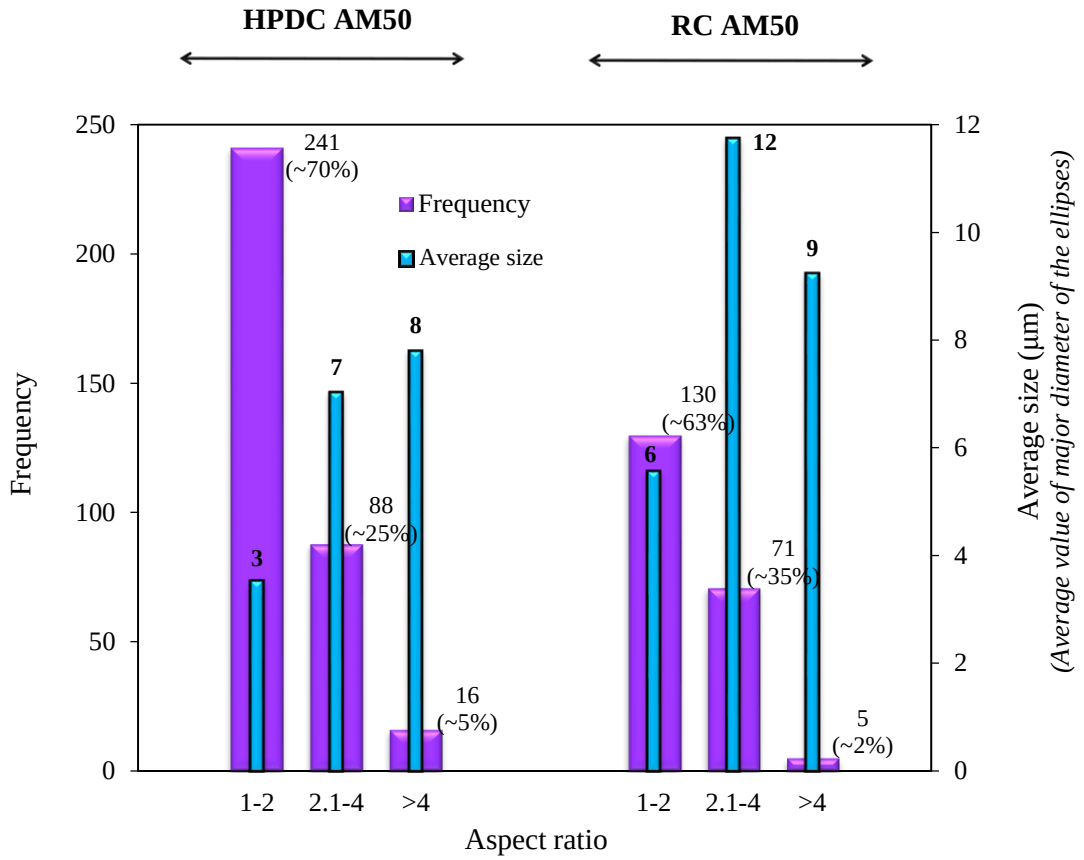

Fig. 33. Distribution of aspect ratio and average size of β-particles in the RC and HPDC AM50**.**

The size of a β-phase particle was approximated by the major diameter of the ellipse in which the particle was inscribed. It is important to measure the average size of the β-phase, since larger particles can protect a larger area of an α grain. Hence, in addition to the distribution of the aspect ratio, Fig. 33 includes the distribution of the average size of β particles. Figure 34 shows a schematic comparison between a β particle with the aspect ratio of 3.5 and size of 4 μm and another β particle with the aspect ratio of 2.5 and a size of 10 μm. For the same grain size of α-Mg (e.g. 10 μm), the small particle with a larger aspect ratio (i.e. 3.5) is less protective than the large particle with lower aspect ratio (i.e. 2.5).

The β-phase intermetallics can be divided into two groups: with low aspect ratio (1-2) and with high aspect ratio (>2), respectively. Figure 33 shows that the fraction of β particles with high aspect ratio was slightly lower in the case of HPDC AM50 (~30%) compared to RC AM50 (~37%). Furthermore, in the case of alloy HPDC AM50, the β particles with low aspect ratio had an average size of 3 μm and the β particles with high aspect ratio had an average size of 7.5 μm. On the other hand, for alloy RC AM50, the β particles with low and high aspect ratios had an average size of 6 μm and 10.5 μm, respectively. Hence, there is a higher fraction of large elongated β-phase intermetallics in RC AM50 than in HPDC AM50, which is considered beneficial by forming a barrier against the corrosion of the alloy.

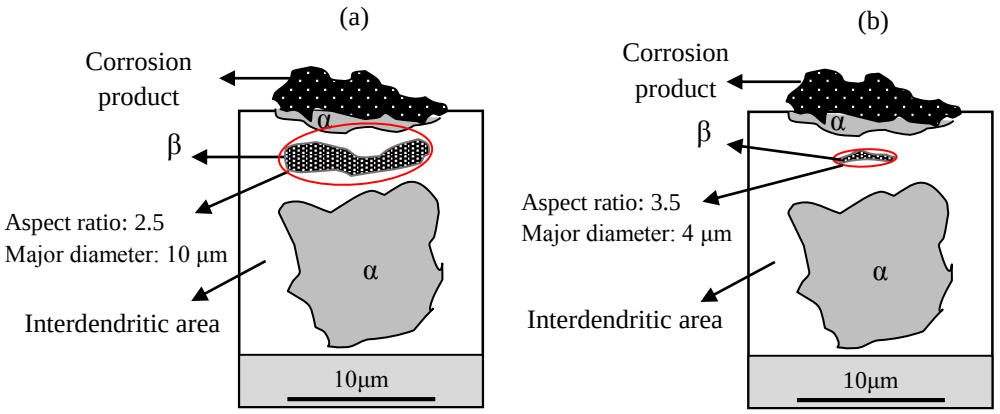

Fig. 34. Schematic cross-section overview of corroded AM50 alloy. (a) α grain is protected by a large β particle. (b) α grain is not protected by a small β particle.

The different cooling regimes during casting affect grain size, β-phase fraction and the interdendritic fraction in the alloy. In addition, different sections of cast components are expected to exhibit variations in microstructure due to different cooling rates [124]. Accurate measurement of the area fraction of the interdendritic region is a challenge, since it is partly mixed with the β particles and because there is no clear boundary between the primary α-Mg and the interdendritic region.

Table 11 summarizes the distribution of different phases in alloy RC AM50 and alloy HPDC AM50 that were investigated in a previous paper [125].

Table 11. *Distribution of different phases in the RC AM50 and HPDC AM50 [125].

RC AM50	HPDC AM50
Higher area fraction of α-Mg (~80%)	Lower area fraction of α-Mg (~68%)
Slightly lower average Al concentration at the center of α-Mg (1.8 ± 0.15 wt.%)	Slightly higher average Al concentration at the center of α-Mg (1.9 ± 0.25 wt.%)
Higher area fraction of β-phase (~6%)	Lower area fraction of β-phase (~2%)
Lower number density of β-phase	Higher number density of β-phase
Lower area fraction of interdendritic region (~12%)	Higher area fraction of interdendritic region (~26%)
Higher average concentration of Al in the interdendritic region	Lower average concentration of of Al in the interdendritic region
Slightly lower area fraction of η-phase (0.35%)	Slightly higher area fraction of η-phase (0.40%)

**Please note that the HPDC AM50 that was used in [125] was produced using different casting parameters to the HPDC AM50 discussed e.g. in Fig. 33.*

The difference in the area fraction of β-phase and Al concentration of the α-Mg grain in Table 10 and Table 11 derives from the HPDC AM50 material being obtained from two different foundries. Also, in the case of RC AM50, the difference in the area fraction of β-phase shown in Table 10 and Table 11 corresponds to the different sections of the cast where samples were machined. Nevertheless, the dependence of corrosion on the microstructure is comparable.

The results in Table 11 led us to conclude in our previous article [125] that the lower corrosion resistance of HPDC AM50 was due to the dispersion of greater number of β-phase particles in this alloy compared to RC AM50. It was argued that β acts as a cathode, activating more anodic sites in HPDC AM50 than in RC AM50. Area fraction measurements of the η-phase on different samples resulted in same value of 0.40% for both RC AM50 and HPDC AM50 (see paper I).

If the interdendritic region surrounds the α-Mg grains, the lower area fraction of the interdendritic region in the case of RC AM50 (as can be seen in Table 11) implies that the dendritic region is thinner in the case of RC AM50 compared to HPDC AM50. In addition, a higher average concentration of Al in the interdendritic region was reported for RC AM50 compared to HPDC AM50. Hence, it can be concluded that the α-Mg grains in the RC AM50 were surrounded by interdendritic regions with higher Al concentration compared to HPDC AM50. Sachdeva reported [126] that the Al-rich interdendritic region (including β-phase) acted as a barrier against corrosion of HPDC AM50 in aerated 1.6 wt.% NaCl solution. This may also be a reason for the better corrosion resistance of RC AM50 compared to HPDC AM50.

The results suggest that the area fraction of Al-rich regions (i.e. interdendritic area + β-phase) is more crucial in the corrosion of MgAl alloys than the concentration of Al in the solid solution α grains.

4.2.3.3. 2D and 3D characterization of localized corrosion

4.2.3.3.1. Corrosion product morphology in the presence and absence of CO_2

Inspection of corroded samples in SEM showed that the casting technique had little influence on the corrosion product morphology. Thus, the SE micrographs of Fig. 30 showing corroded surfaces of HPDC AM50 and DC AZ91 after 672 h exposure in the presence of 70 µg/cm² NaCl, also represent the corrosion product morphology of the RC counterparts of the two alloys[5]. As expected, a more pronounced corrosion attack can be observed in alloy AM50 compared to alloy AZ91, both in the presence and absence of CO_2. Also, an inspection of Fig. 30 indicates that both alloys exhibited a greater tendency for localized corrosion in the absence of CO_2. Hence, in the presence of CO_2, corrosion products covered most of the surface, while in the absence of CO_2, parts of the surface were only slightly affected or not affected at all by corrosion. This is in connection with the rest of the surface that was covered by relatively thick corrosion products (compare Fig. 30 (c) and (e) in the presence of CO_2 with Fig. 30 (d) and (f) in the absence of CO_2). The heavily corroded areas formed in the absence of CO_2 tended to interconnect, forming channel-like connections illustrated in Fig. 30 (f) for alloy AZ91. The connections are indicated by red dashed lines in Fig. 30 (f). Regions 4, 5 and 6 in Fig. 30 (f) exemplify unconnected corroded regions. Also, in the case of AM50 alloy exposed in the absence of CO_2, significantly larger channels-like connections formed, compared to those formed on alloy AZ91 (compare Fig. 30 (d) and (f)). After exposure in the presence of CO_2, both alloys exhibited spherical agglomerations of corrosion products, indicated by green arrows in Fig. 30 (c) and (e). The different morphology of the corrosion products is discussed in the following section.

[5] The corrosion product morphology of RC AM50 and RC AZ91 are described in paper III and paper V.

4.2.3.3.2. Development of cathodic and anodic sites (an EDX analysis)

As mentioned earlier, corrosion of MgAl alloys in the presence of an aqueous solution is an electrochemical process that involves cathodic and anodic regions. When dissolved in water NaCl dissociates and forms Na^+ and Cl^-. Accordingly, Na^+ migrates to the cathodic regions where OH^- is accumulated and Cl^- migrates towards the anodic regions where Mg^{2+} is produced. In the case of pitting corrosion, the bottom of the pit is anodic. Thus, chloride ions are expected to concentrate in the bottom of the pits. We have previously shown the accumulation of chloride ions in the bottom of the pits for corrosion of HPDC AM50 by preparing BIB milling cross-sections (see paper II). Detection of Cl^- in the pits is extremely difficult on plan-view EDX characterization because of the corrosion products that form on top of the pits. If Cl^- is identified on the surface being separated from Na^+, it can be concluded that certain anodic sites have been active during the last stage of corrosion, just before the exposure was interrupted. Thus, all the potential anodic sites are not active simultaneously.

Figure 35 shows EDX elemental maps of the corroded surface of alloy RC AM50 after 672 h exposure in the presence of 400 ppm CO_2 and 70 µg/cm² NaCl, at 95% RH and 22°C. The overlap of the Na and Cl maps shows the presence of NaCl on the sample surface, indicating that the NaCl was not consumed completely in this case. The elemental maps in the vicinity of the salt particle show chlorine but no Na. EDX point analysis at the Cl-enriched area (indicated by a cross in Fig. 35) revealed that it was dominated by O, Mg, C, and Cl, implying that Cl was associated with magnesium. No Mn was detected in the mapping area, thus the Al rich areas correspond to β-phase particles (and the interdendritic region). No significant amount of Na was detected in the Al-rich areas. Na was only detected in the NaCl particle that was likely recrystallized when the exposure was interrupted. This suggests that no efficient cathode was available in the mapped area. In the presence of CO_2 there will be less pH gradient in the electrolyte due to neutralization of the electrolyte by CO_2.

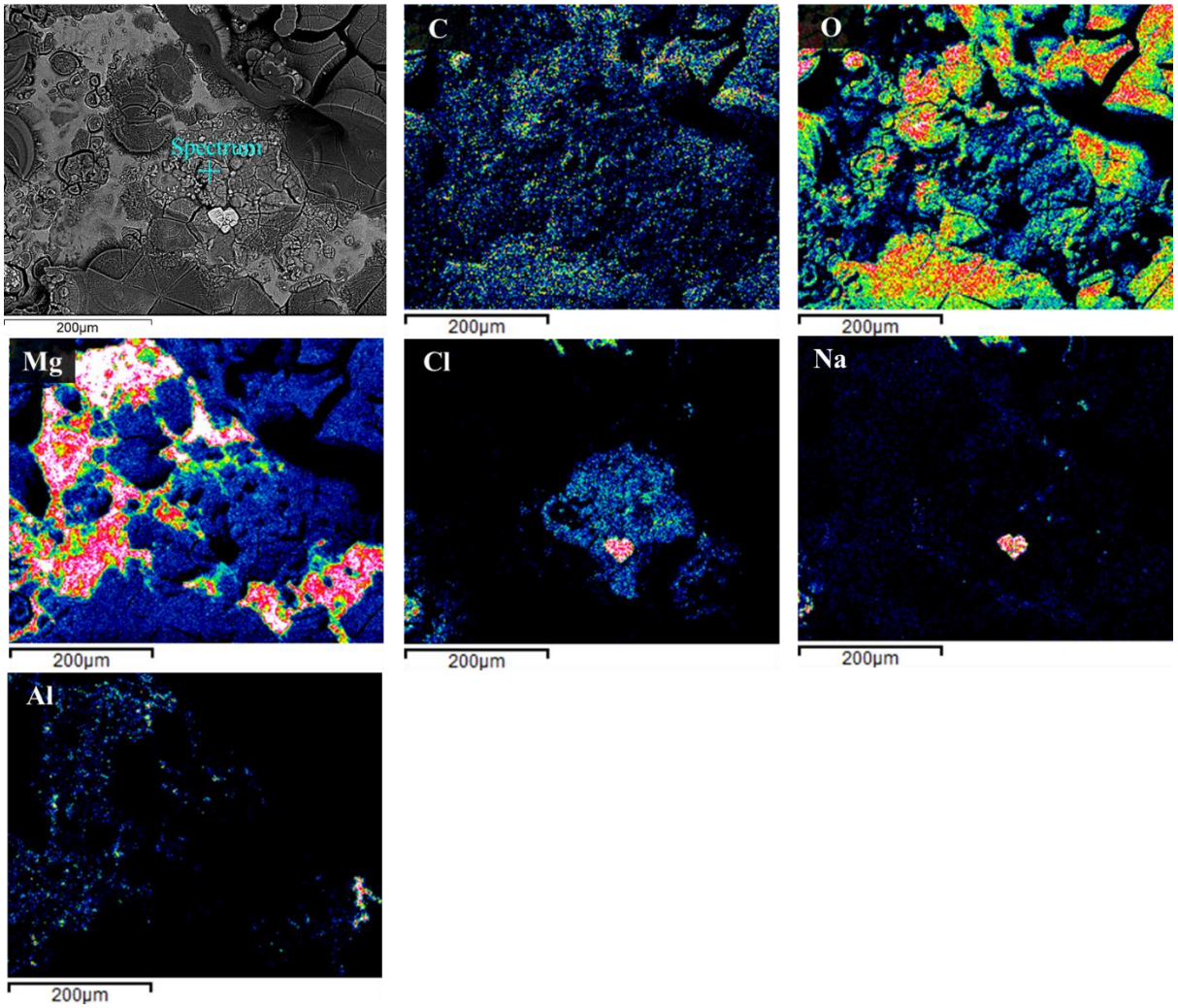

Point analysis.

Element	O	C	Mg	Cl	Na	Al
Atomic %	45	23	21	12	<1	-

Fig. 35. EDX map and point analysis for alloy RC AM50 exposed in the presence of 400 ppm CO_2 and 70 µg/cm² NaCl for 672 h at 95% RH and 22°C.

Figure 36 demonstrates EDX elemental mapping of alloy AM50 exposed in the absence of CO_2 and in the presence of 70 µg/cm² NaCl for 672 h at 95% RH and 22°C. In this case, there was no indication of NaCl, the Cl and Na maps showing little overlap. Thus, Na was concentrated on the relatively uncorroded metal surface between the corrosion product accumulations, where there was little evidence for Cl. At the regions with highest Na count, Al particles were present according to the respective elemental map. Also, in contrast to the area selected in Fig. 35, Mn was detected in the area selected in Fig. 36, where Na was present. The presence of Mn is attributed to η-phase particles. In the absence of CO_2, strong pH gradients are expected to develop between anodic and cathodic sites. Thus, NaOH (aq) is expected to accumulate in the cathodic regions. $Mg(OH)_2$ is insoluble at high pH and is expected to dominate in the cathodic

sites. Chlorine was mainly detected on the periphery of the large corrosion product accumulations and in relatively small corrosion product features.

An EDX point analysis of a small Cl-rich surface feature (indicated by a cross in Fig. 36) showed that it consisted of O, Mg, Cl and C, being similar to the point analysis in Fig. 35 and indicating the presence of magnesium chloride. The carbon detected in Fig. 36 is suggested to be contamination due to handling in laboratory air.

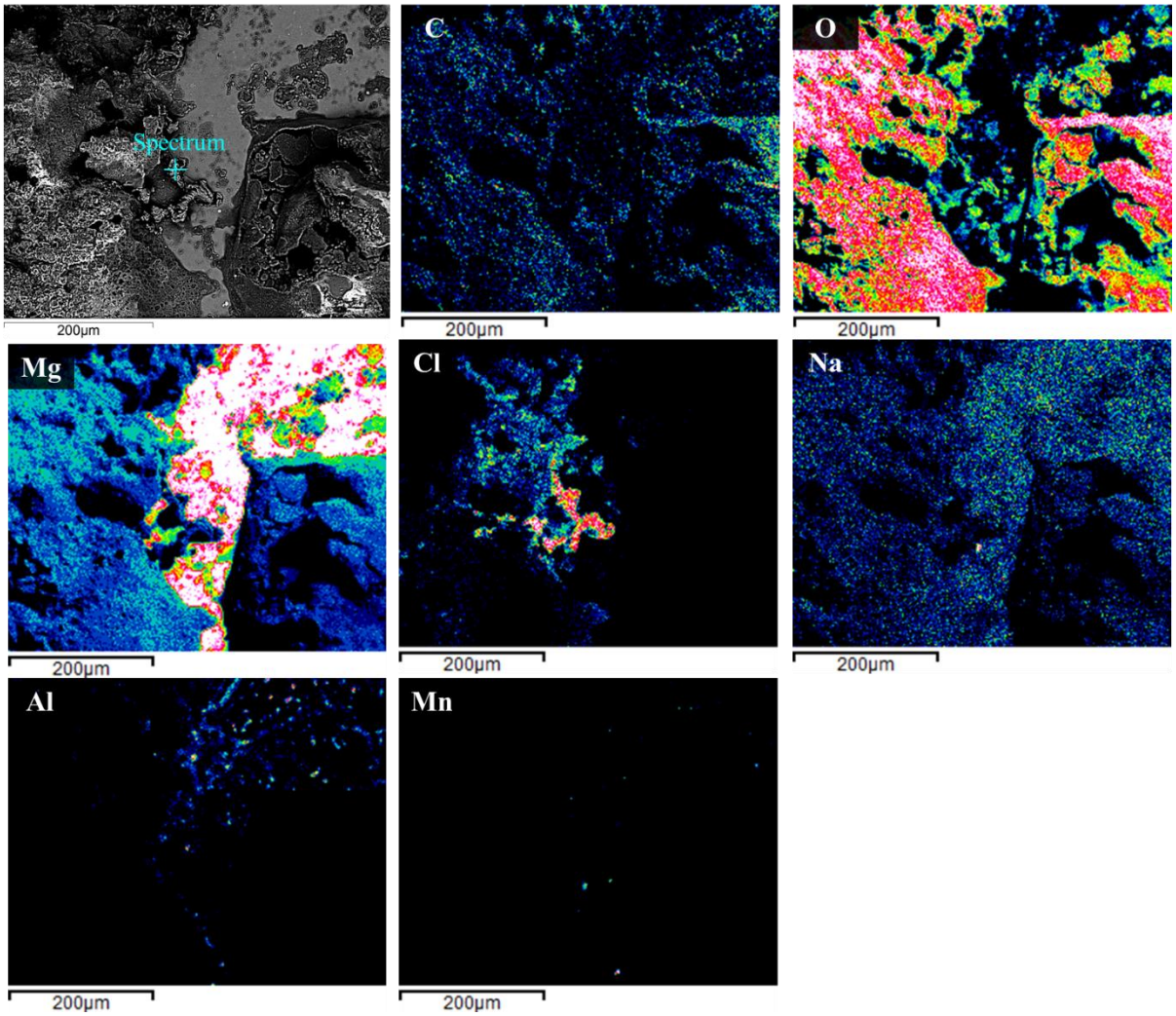

Point analysis.

Element	O	Mg	Cl	C	Al	Mn	Na
Atomic %	48	24	15	10	1	<1	-

Fig. 36. EDX map and point analysis for the RC AM50 alloy exposed in the absence of CO_2 and in the presence of 70 µg/cm² NaCl for 672 h at 22°C and 95% RH.

Fig. 37 shows an EDX map of another area of alloy RC AM50 after exposure in the absence of CO_2. The main difference between the maps in Fig 36 and Fig. 37 is a higher frequency of intermetallics (i.e. β and η) as shown by the Mn and Al maps. Figure 37 shows a strong tendency

for Na to be associated to the Mn-containing intermetallic particles, i.e. η-phase. The absence of Cl in the selected area, suggests that no anodic sites were present.

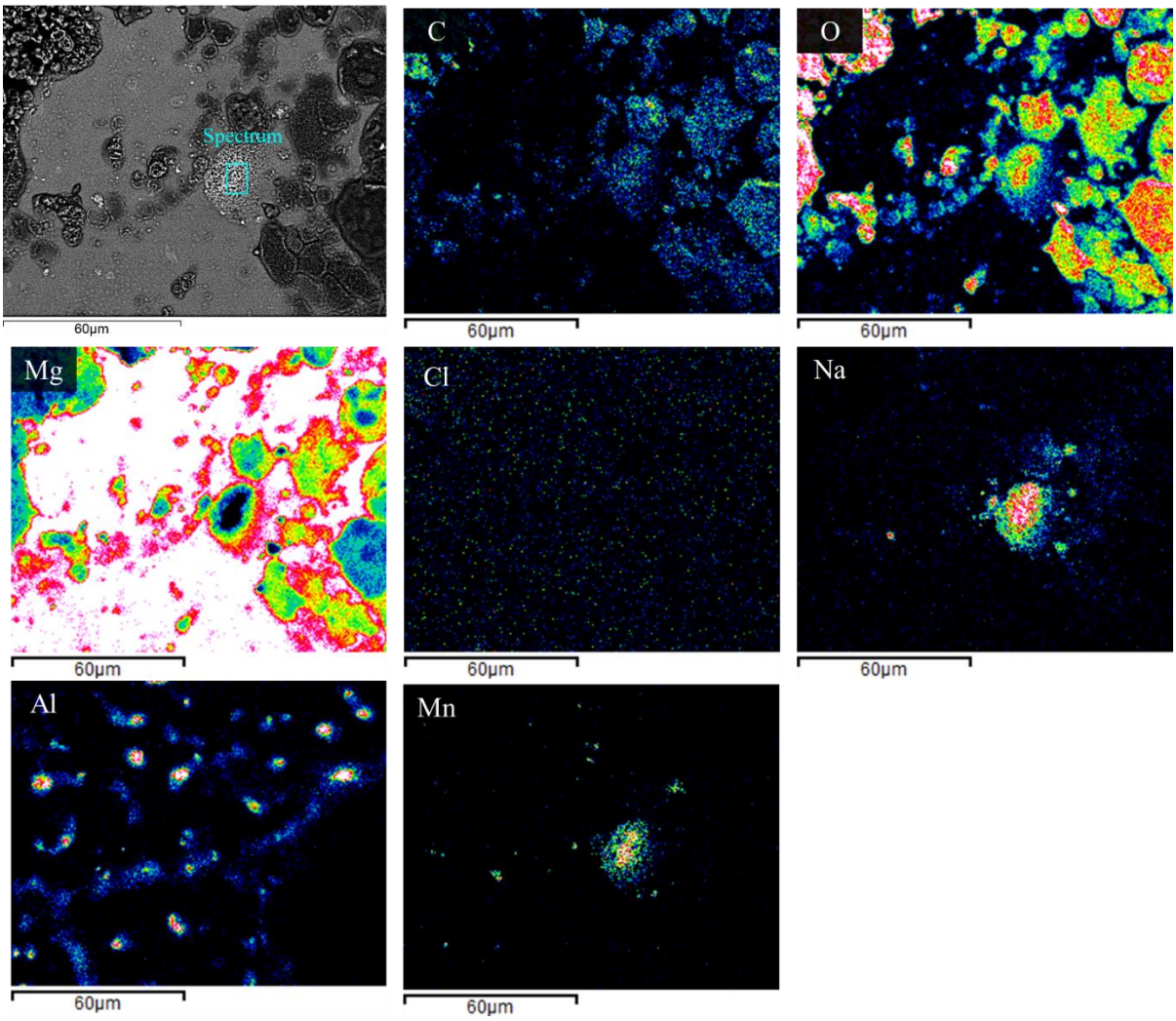

Point analysis.

Element	O	Mg	C	Na	Mn	Al	Cl
Atomic %	46	26	13	8	5	2	-

Fig. 37. EDX map and point analysis of alloy RC AM50 exposed in the absence of CO_2 (70 µg/cm² NaCl, 672 h, 22°C, 95% RH).

Jönsson et al. [41] reported that η particles has a high corrosion potential (V) compared to both β and α-Mg. Their in-situ Volta potential measurements by means of scanning Kelvin probe force microscopy (SKPFM) revealed the following sequence for the relative Volta potentials of the microstructural constituents in DC AZ91: η > β ~ interdendritic > α-Mg. Thus, η-phase, β-phase and the interdendrtitic region were all cathodic towards the α-Mg grains. Nevertheless, Jönsson et al. suggested [127] that the η-phase did not involve in the initiation of corrosion since it was embedded in the β-phase (and in the interdendritic region), and thus located away from the α-phase. On the other hand, Arrabal et al. [91] have shown that corrosion of MgAl

alloys occurred at the interface of the β-/η- and α-phase. Hence, it can be inferred that both β and η may act as cathodes in MgAl alloys, developing micro-galvanic cells. Actually, the EDX elemental maps of Fig. 35, 36 and 37 suggest that η-phase was the most efficient cathode in the present investigations, provided that it formed independently on the α-grain. The greater cathodic activity of η-phase compared to that of β-phase in the absence of CO_2, is due to the electronic conductivity of the surface film that forms in each of the particles. In the absence of CO_2, , alumina dissolves in the passive film due to the high pH increase at the cathodic areas and β-phase will likely be covered by insulating $MgO/Mg(OH)_2$ film. In the same environment, η-phase is expected to be covered by $Mn_xO_y/Mn(OH)_2$ oxide(s)/hydroxide where MnO, Mn_3O_4 and MnOOH are semi-conductors. This is in good agreement with a recent publication by Danaei et al. [128] that reported that after 96 h exposure in 1.6 wt.% NaCl solution, Mn_3O_4 formed on the η-phase due to high local alkalinity and preferential dissolution of Al. On the other hand, in the presence of 400 ppm CO_2, alumina is more stable at the cathodic areas (due to neutralization) and the surface film on both β- and η-phase is dominated by alumina.

The difference in the corrosion morphologies observed in the presence and in the absence of CO_2 may be related to pH development on the sample surface. The contrast between the small galvanic cells formed in the presence of CO_2 and large galvanic cells formed in the absence of CO_2, is seen in Fig. 5 (c), (e) and Fig. 5 (d), (f); respectively. Investigating the NaCl-induced atmospheric corrosion of Cu, Chen et al. reported [129] that NaCl (aq) droplets formed at 80% RH in air on the sample, tended to spread over the metal surface when the concentration of CO_2 was <5 ppm. In contrast, there was little spreading of the droplets at ambient levels of CO_2. The effect was explained by the cathodic reaction causing high pH in the periphery of the droplet in the absence of CO_2. The high pH resulted in a negative surface charge on the surface of the corrosion product film, decreasing the surface tension of the oxide-electrolyte interface and favoring droplet spreading. Figure 5 (c) and (e) show an accumulation of closely spaced spherical corrosion products on the surface of the RC AM50 and RC AZ91 alloys, in the presence of 400 ppm CO_2. This might be attributed to the absence of NaCl (aq) droplet coalescence. On the other hand, after the CO_2-free exposures for both of the alloys, extensive localized corrosion was observed that corresponds to the coalescence of most NaCl (aq) droplets in this case. In addition, the channel-like connection between the extensive corrosion cells in the absence of CO_2, suggests a moving-anode phenomenon in this case (see Fig. 5 (d) and (f)).

4.2.3.3.3. Corrosion pits–formation and connectivity

The characterization of corrosion pits will be discussed based on the results from alloy RC AM50. At the end of this section, the findings for other materials will also be mentioned for comparison.[6]

Following corrosion product removal by pickling, 3D topographical profiles were obtained. They are presented in Fig. 38 as well as 2D profiles (see the lines parallel to the X and Y direction on each sample). On each sample, a region of interest (ROI) is indicated showing a

[6] For the corresponding analysis of RC AZ91, see paper V.

typical pitted area. On the 2D profile the ROI is situated between the red and the blue line (see Fig. 38).

While corrosion was relatively evenly distributed over the whole surface after exposure in the presence of CO_2, severe corrosion affected only a small part of the surface in the absence of CO_2, large areas being seemingly uncorroded after exposure (see Fig. 38). These observations were corroborated by 3D imaging after corrosion product removal. Thus, Fig. 38 (a) shows that relatively evenly distributed pits on the surface after corrosion in the presence of CO_2. In contrast, two different distributions of pits were identified after corrosion in the absence of CO_2 (see Fig. 38 (b) and (c)). Hence, the sample that was exposed in the presence of 400 ppm CO_2 exhibited circular pits that were typically ~40 µm deep. In contrast, the sample that was exposed in the absence of CO_2 showed relatively deep connected pits (~80 µm) with a channel-like morphology as well as shallow circular pits (~5 µm). The two features were located at a distance from each other and were not connected. The shallow pits formed in the absence of CO_2 are analogous to the anodic sites observed in regions 4, 5 and 6 of Fig. 30 (f). The size of the initial NaCl (aq) droplets as well as the availability of the electrolyte might have influenced the connectivity of the anodic sites.

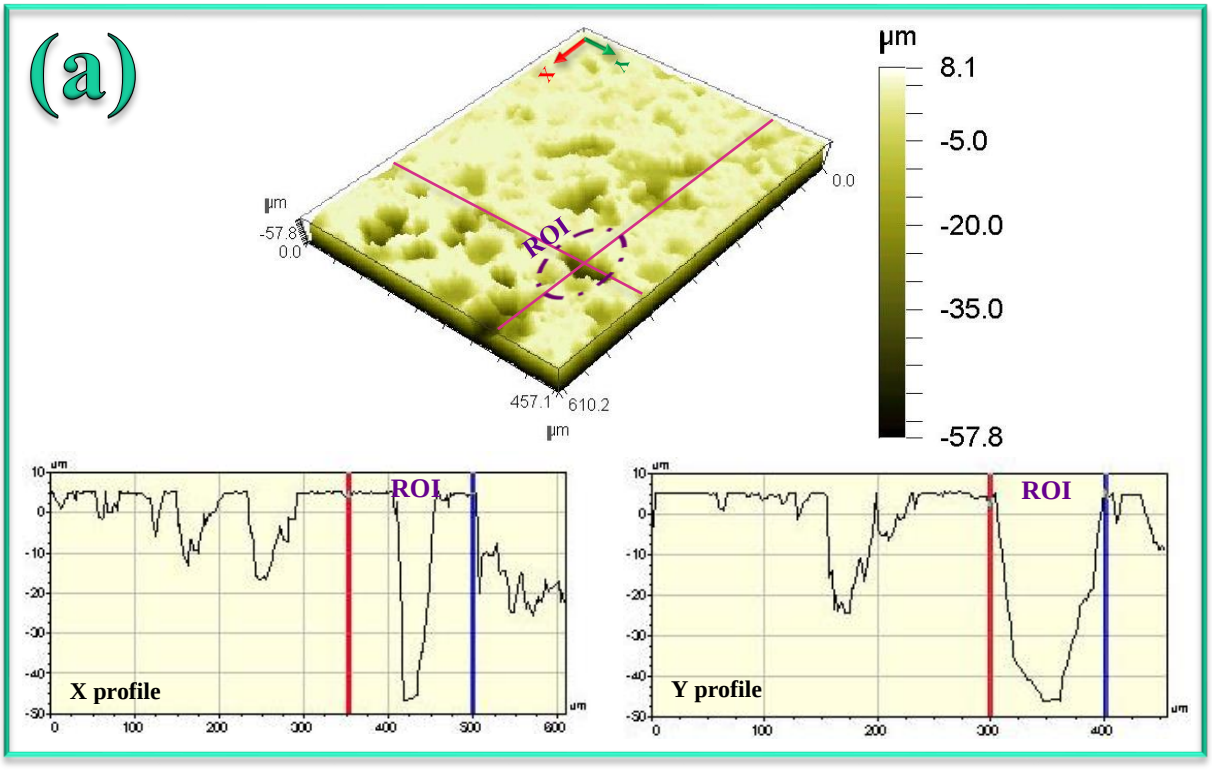

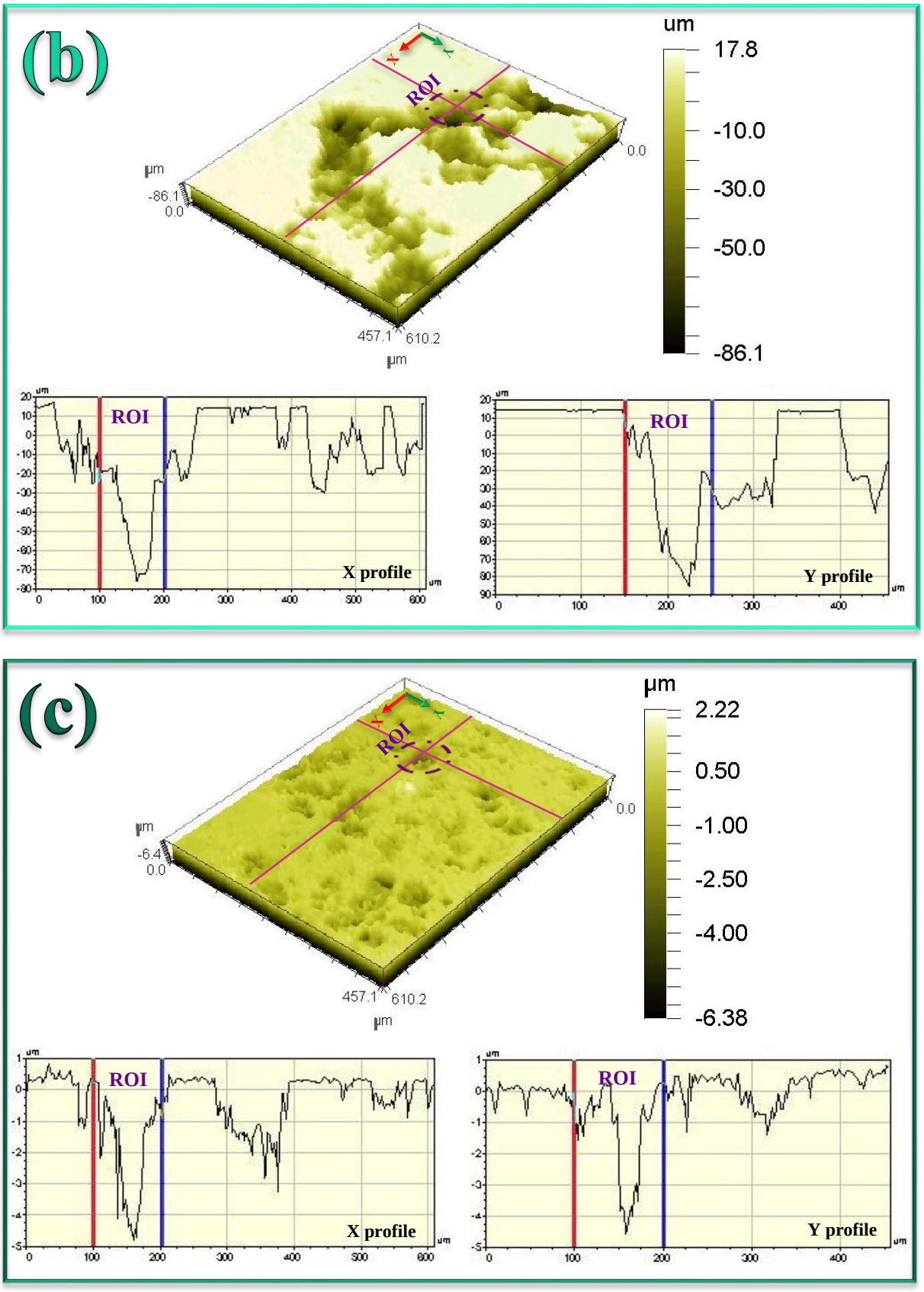

Fig. 38. 3D and 2D depth profiles of the pits for the alloy RC AM50 exposed at 95% RH and 22°C and in the presence of 70 µg/cm² NaCl for 672 h, (a) in the presence of 400 ppm CO_2 and (c)-(d) in the absence of CO_2.

The pits have irregular shapes. Also, as the 2D line profiles in Fig. 38 show, the pits have different depths. To complement the results from the optical profilometry, random regions with pits were chosen and studied by consecutive steps of FIB cross-sectional milling-SE imaging. This procedure allowed us to study the connectivity of pits with 500 nm increments (i.e. the thickness of each slice) in the selected area. A stack of images was compiled corresponding to the investigated volume.

Figure 39 shows selected cross-sections that were cropped from the compiled volumes. Figure 39, also includes the plan view micrograph of the same volume and shows the selected area. Figure 39 (a) displays circular pits formed in the presence of 400 ppm CO_2 while Fig. 39 (b) shows the deep channel formed in the absence of CO_2. Note that the channel is formed from individual pits connecting to neighboring pits. It is not clear at this stage whether the individual pits formed and grew simultaneously, or if the channel-like connection formed through a moving-anode phenomenon. In contrast, only circular pits formed in the presence of CO_2. This suggests that neutralization by CO_2, which leads to less pH gradients, resulted in formation of smaller corrosion cells. Thus, smaller anodic sites were surrounded by smaller cathodic areas, reducing the probability of a moving anode phenomenon.

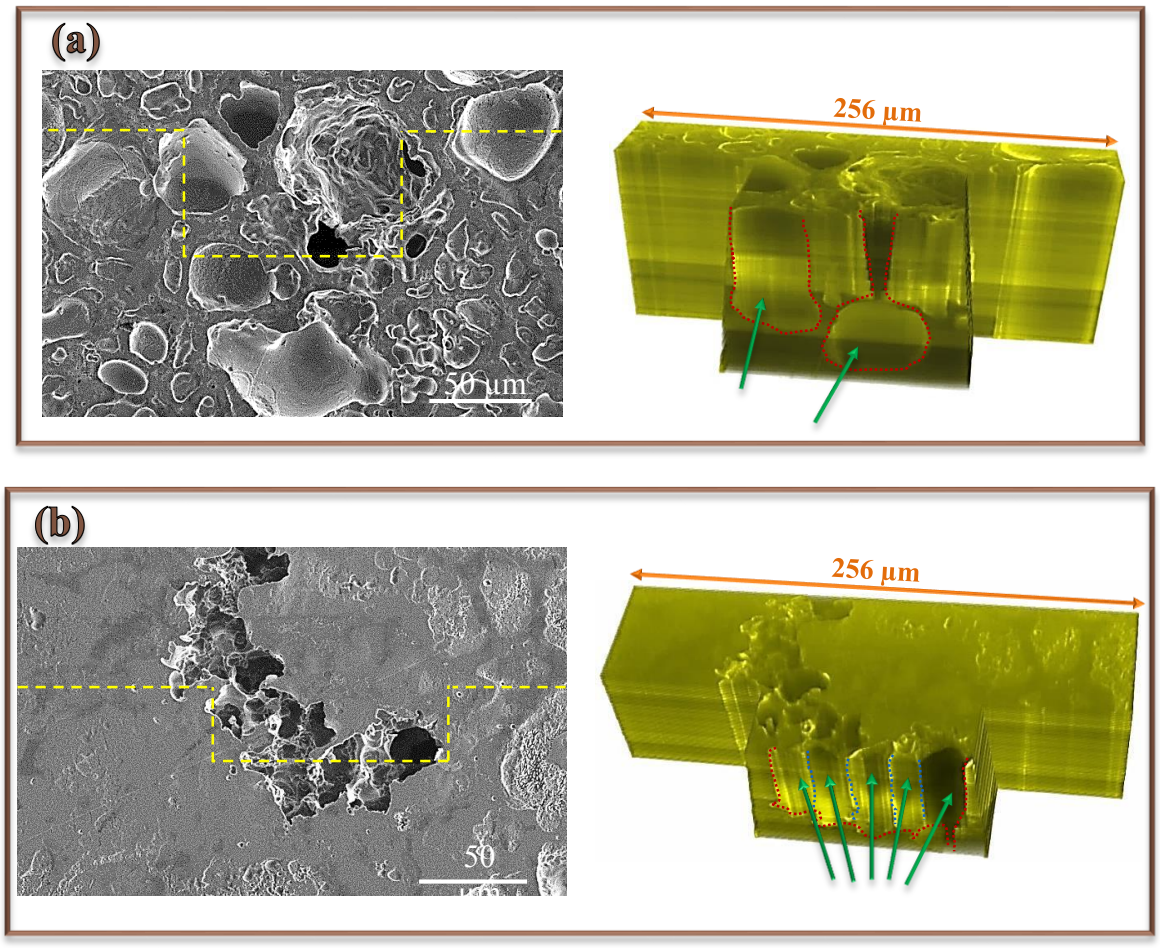

Fig. 39. 3D imaging of corrosion pits formed on alloy RC AM50 exposed at 95% RH and 22°C in the presence of 70 µg/cm² NaCl for 672 h, (a) in the presence of 400 ppm CO_2 and (b) in the absence of CO_2.

5. Concluding remarks

The atmospheric corrosion of Mg and MgAl alloys AM50 and AZ91 was investigated. The passive film was characterized and a mechanism was proposed for film growth. In addition, the NaCl–induced atmospheric corrosion of Mg and MgAl alloys was studied. The effects of CO_2 and microstructure on the morphology of corrosion were analyzed. In the case of the alloys, comparisons were made between materials prepared by rheocasting and by conventional casting (i.e. DC and HPDC). The major findings of the present thesis are summarized below.

- Exposure of Mg and two MgAl alloys to air with 95% RH resulted in the growth of a $Mg(OH)_2$/MgO surface film and some localized corrosion.

- In the absence of CO_2, the film surface consisted of $Mg(OH)_2$ while the bulk of the film was made up of MgO containing some hydroxide. The film was covered by a thin layer of carbonate in the presence of CO_2.

- The films formed on the two MgAl alloys were similar to the films formed on Mg except that they contained a few percent of alumina. The aluminum concentration increased towards the film/alloy interface.

- The presence of Al^{3+} in the film caused brucite to be replaced by a layered double hydroxide (LDH).

- The film is suggested to grow by the reaction of $Mg(OH)_2$ with the metal. $Mg(OH)_2$ forms by dissociative chemisorption of H_2O in the grain boundaries of the MgO film. Film growth is slower in the presence of CO_2.

- Localized corrosion of Mg and MgAl alloys is suggested to be initiated by film thinning through a dissolution-precipitation mechanism where the more soluble MgO is dissolved into the liquid-like surface water layer, to be precipitated as brucite $Mg(OH)_2$ or LDH. That dissolution was accelerated at the vicinity of the first precipitation, leading to pit formation. MgO is always expected at the bottom of the film and the pits.

- Localized corrosion was more frequent in the presence of CO_2. This is attributed to the acidity of CO_2 that speeds up film dissolution and to the observation that CO_2 causes the films to be thinner.

- Atmospheric corrosion of Mg and MgAl alloys was significantly more severe in the presence of NaCl (aq) due to the increased conductivity of the electrolyte. Brucite was the main corrosion product in the absence of CO_2. In the case of the alloys, the LDH compound meixnerite was also detected. In the presence of 400 ppm CO_2, magnesium hydroxy carbonates were the dominating corrosion products. Meixnerite and

$Mg_5(CO_3)_4(OH)_2 \cdot 8H_2O$ were identified and reported as corrosion products for the first time.

- It was shown that CO_2 inhibited corrosion, particularly in longer stages of corrosion. That was suggested to be attributed to the formation of a magnesium hydroxy carbonate film which has less solubility than $Mg(OH)_2$ and MgO. For MgAl alloys, the neutralization by CO_2 also stabilized alumina in the passive film together with $Mg(OH)_2$.

- Lower corrosion rate was measured for MgAl alloys compared to CP Mg in the presence and in the absence of CO_2. This effect was attributed to the presence of $A1^{3+}$ (in the passive film) and to the presence of β-phase. Also, the semi-continuous distribution of β intermetallics increased the corrosion resistance of alloy AZ91 compared to alloy AM50 in which β particles were individually distributed.

- It was shown that rheocasting improved the corrosion resistance of alloy AM50 compared to HPDC material. This was due to the high fraction of β particles in the RC material compared to HPDC one. Also, it was shown that in general, the β intermetallics formed in the RC case had a higher aspect ratio and larger size than those formed in the HPDC material.

- In the absence of CO_2 the η-phase (Al-Mn) precipitates were cathodically more active than the β-phase particles. This is explained by the high pH electrolyte which dissolves alumina, leaving behind a $Mn_xO_y/Mn(OH)_2$ surface film on the η-phase particles which is more conductive electronically in contrast to the alumina–dominated film present at lower pH (in the presence of CO_2).

- The clustering of pits in the absence of CO_2 is attributed to the growth of the corrosion cells, encompassing a growing number of cathodic sites. Due to the resulting increased anodic polarization of the area in the vicinity of the original pit, new pits tend to initiate.

6. Future work

In the present thesis, the surface film was characterized by means of surface sensitve techniques such as XPS, FTIR, GI-XRD, and AES. Also, a chemical reaction mechanism was proposed that explained the thickening of this film at high humidity. The XPS results (calibrated for Ta_2O_5) suggest that the film was ~2 nm and ~10 nm thick in the presence and in the absence of CO_2, respectively. It will be interesting to investigate the surafce film using TEM and to check its thickness. In addition, electron diffractionmay reveal the composition of the film which complements the findings of this thesis.

Regarding presented chemical reaction mechanism, this thesis proposed that H is produced at the interface of film and metal. However, the presence of H in the substrate could not be shown by means of the instruments employed in the present thesis. Hence, SIMS analysis might also complement our results.

In the case of the NaCl–induced corrosion, 3D imaging by means of FIB milling was employed which contributed to the understanding of pit connectivity. However, the in-situ slice and image technique can also be used before corrosion product removal. One challenge against cross-sectional milling in this case is the massive curtaining effect due to the uneven corrosion products. Thus, it requires a high degree of caution and protection while milling. What might be really interesting in this case is to run 3D EDX mapping to study the distribution of Na and Cl in the vicinity of pits. In addition, 3D EBSD phase mapping can be performed, which can complement the XRD results of the present thesis.

Also, EBSD orentation mapping can be performed to investigate the probable influence of orientation of grains on the corrosion of Mg and MgAl alloys. Few people have been published in this area and those that were published do not cover alloys with different microstrcutures [130-132]. Caution should be taken in to account while performing this experiment to ensure that electrolyte covers the entire surface homogenously.

Acknowledgement

My deepest gratitude goes to my supervisor Prof. Lars-Gunnar Johansson for his substantial support, instructive comments, his kindness and constant help. I am so grateful for what I have learned in the field of atmospheric corrosion from him during the past four years. I would also like to express my best regards to Prof. Jan-Erik Svensson. He has generously shared his valuable knowledge in the field of atmospheric corrosion and has always showed support for my ideas. My sincere gratitude goes out to Prof. Mats Halvarsson for sharing his expertise in the area of electron microscopy. It would have been so difficult to solve certain problems without his enlightening discussions and encouraging comments. Many thanks to Dr. Yu Cao for her invaluable contributions in XPS measurements. This work would not have been completed without her fruitful collaboration. Special thanks to Dr. Rikald Ylmén for his contributions to FTIR measurements.

This work was performed in close collaboration with my colleague Mr. Mohsen Esmaily. It was a great opportunity to work closely with him. We were able to establish an efficient system that helped us move this project forward. I want to thank Mohsen for being friendly, caring and helpful. I wish him the best in his future career.

Dr. Anders Kvist, Mr. Esa Väänänen and Mr. Erik Brunius are gratefully acknowledged for their technical support throughout the work. Also, Ms. Charlotte Bouveng and Ms. Sandra Gustafson are truly appreciated for their kind administrative help.

Special thanks go out to all my colleagues and friends in the Environmental Inorganic Chemistry division who were always supportive and helpful.

My deep thanks go out to the Swedish Foundation for Strategic Research (SSF) for funding this project. I also want to acknowledge Jönköping University for providing the semi-solid material.

I cannot thank my family enough for they are the only thing I have and that is the pure honest truth.

Mehrdad Shahabi
August 2015, Gothenburg

References

1. Kojima, Y., *Platform science and technology for advanced magnesium alloys.* Magnesium Alloys 2000, 2000. **350-3**: p. 3-17.
2. Song, G.-L. and A. Atrens, *Corrosion mechanisms of magnesium alloys.* Advanced Engineering Materials, 1999. **1**(1): p. 11-33.
3. Gray, J.E. and B. Luan, *Protective coatings on magnesium and its alloys - a critical review.* Journal of Alloys and Compounds, 2002. **336**(1-2): p. 88-113.
4. Wang, R.M., Eliezer, A., Gutman, E., *Microstructures and dislocations in the stressed AZ91D magnesium alloys.* Materials Science and Engineering A, 2002. **344**: p. 279-287.
5. Lee, S., Ham, H.J., Kwon, S.Y., Kim, S.W., Suh, C.M., *Thermal Conductivity of Magnesium Alloys in the Temperature Range from −125°C to 400°C.* International Journal of Thermophysics, 2011. **34**(12): p. 2343-2350.
6. Kuwahara, H., et al., *Surface reaction of magnesium in Hank's solutions.* Magnesium Alloys 2000, 2000. **350-3**: p. 349-358.
7. Kielbus, A., Rzychon, T., Cibis, R., *Microstructure of AM50 die casting magnesium alloy.* Journal of Achievements in Materials and Manufacturing Engineering, 2006. **18**: p. 135-138.
8. Wang, L., Turnley, P., Savage, G., *Gas content in high pressure die castings.* Journal of Materials Processing Technology, 2011. **211**(9): p. 1510-1515.
9. Prakash, D.G., Regener, D., *Micro–macro interactions and effect of section thickness of hpdc AZ91 Mg alloy.* Journal of Alloys and Compounds, 2008. **464**(1-2): p. 133-137.
10. Huang, H., Kato, H., Chen, C., Wang, Z., Yuan, G., *The effect of nanoquasicrystals on mechanical properties of as-extruded Mg–Zn–Gd alloy.* Materials Letters, 2012. **79**: p. 281-283.
11. Zhu, S.Q., Yan, H. G., Chen, J. H., Wu, Y. Z., Liu, J. Z., Tian, J. , *Effect of twinning and dynamic recrystallization on the high strain rate rolling process.* Scripta Materialia, 2010. **63**(10): p. 985-988.
12. Minárik, P., Král, r., Janeček, M., *Effect of ECAP processing on corrosion resistance of AE21 and AE42 magnesium alloys.* Applied Surface Science, 2013. **281**: p. 44-48.
13. Flemings, M.C., Riek, R. G., Young, K. P., *Rheocasting.* Materials Science and Engineering, 1976. **25**: p. 103-117.
14. Antion, C., Donnadieu, P., Perrard, F., Deschamps, A., Tassin, C., Pisch, A., *Hardening precipitation in a Mg–4Y–3RE alloy.* Acta Materialia, 2003. **51**(18): p. 5335-5348.
15. Száraza, Z., Trojanová, Z., Cabbibo, M., Evangelista, E., *Strengthening in a WE54 magnesium alloy containing SiC particles.* Materials Science and Engineering A, 2007. **462**(1-2): p. 225-229.
16. Tikhova, N.M., Blokhina, V. A., Antipova, A. P., Vasil'eva, T. P., Solov'eva, G. G., *Effect of prolonged heating on the properties of magnesium alloys ML9 and ML10.* Metal Science and Heat Treatment, 1971. **13**(10): p. 887-890.
17. Ning, Z., Liu, H. H., Cao, F. Y., Wang, S. T., Suna, J. F., Qian, M., *The effect of grain size on the tensile and creep properties of Mg–2.6Nd–0.35Zn–xZr alloys at 250°C.* Materials Science and Engineering A, 2013. **560**: p. 163-169.

18. Guangyin, Y., Manping, L., Wenjiang, D., Inoue, A., *Microstructure and mechanical properties of Mg–Zn–Si-based alloys.* Materials Science and Engineering A, 2003. **357**(1-2): p. 314-320.
19. Yang, M., Li, H., Duan, C., Zhang, J., *Effects of minor Ti addition on as-cast microstructure and mechanical properties of Mg–3Sn–2Sr (wt.%) magnesium alloy*. Journal of Alloys and Compounds, 2013. **579**: p. 92-99.
20. Emley, E.F., *Principles of Magnesium Technology*. 1966: Pergamon Press New York.
21. Song, G.-L., A. Atrens, and M. Dargusch, *Influence of microstructure on the corrosion of diecast AZ91D.* Corrosion Science, 1999. **41**(2): p. 249-273.
22. Pardo, A., et al., *Influence of microstructure and composition on the corrosion behaviour of Mg/Al alloys in chloride media.* Electrochimica Acta, 2008. **53**(27): p. 7890-7902.
23. Mathieu, S., et al., *Corrosion behaviour of high pressure die-cast and semi-solid cast AZ91D alloys.* Corrosion Science, 2002. **44**(12): p. 2737-2756.
24. Jonsson, M. and D. Persson, *The influence of the microstructure on the atmospheric corrosion behaviour of magnesium alloys AZ91D and AM50.* Corrosion Science, 2010. **52**(3): p. 1077-1085.
25. Lindstrom, R., J.E. Svensson, and L.G. Johansson, *The influence of carbon dioxide on the atmospheric corrosion of some magnesium alloys in the presence of NaCl.* Journal of the Electrochemical Society, 2002. **149**(4): p. B103-B107.
26. Cui, L., Xiaogang, L., *Role of CO_2 in the initial stage of atmospheric corrosion of AZ91 magnesium alloy in the presence of NaCl.* Rare Metals, 2006. **25**(2): p. 190-196.
27. Martell, A.E., Smith, R. M., *Critical stability constants*. 1974-1989, New York; London: Plenum Press.
28. Nordlien, J.H., et al., *Morphology and structure of oxide films formed on MgAl alloys by exposure to air and water.* Journal of the Electrochemical Society, 1996. **143**(8): p. 2564-2572.
29. Lindstrom, R., L.G. Johansson, and J.E. Svensson, *The influence of NaCl and CO2 on the atmospheric corrosion of magnesium alloy AZ91.* Materials and Corrosion-Werkstoffe Und Korrosion, 2003. **54**(8): p. 587-594.
30. Baril, G. and N. Pebere, *The corrosion of pure magnesium in aerated and deaerated sodium sulphate solutions.* Corrosion Science, 2001. **43**(3): p. 471-484.
31. Ryoo, K., *Metal oxide particle removal using electrolyzed anode water.* Journal of the Electrochemical Society, 2005. **152**(11): p. G885-G888.
32. Lunder, O., Nisancioglu, K., Hansen, R. S., *Corrosion of Die Cast Magnesium-Aluminum Alloys*, in *SAE Technical Paper No. 930755*. 1993.
33. Yang, Z., Li, J. P., Zhang, J. X., Lorimer, G. W., Robson, J. , *REVIEW ON RESEARCH AND DEVELOPMENT OF MAGNESIUM ALLOYS.* Acta Metallurgica Sinica (English Letters), 2008. **21**(5): p. 313-328.
34. Cahn, R.W., Shi, C. X., Ke, J., *Structure and Properties of Nanferrous Alloys*, in *Beijing Science Press*. 1999: Beijing.
35. Buldum, B.B., Sik, A., Ozkul, I., *INVESTIGATION OF MAGNESIUM ALLOYS MACHINABILITY*. INTERNATIONAL JOURNAL OF ELECTRONICS; MECHANICAL and MECHATRONICS ENGINEERING, 2011. **2**(3): p. 261-268.
36. Lee, C.W., Song, D. H., Nam, K. Y., Choi, B. H., Park, Y. H., Cho, K. M., Park, I. M., *Effect of Al on the Castability, Tensile and Creep Properties of Mg-xAl-Zn.* Key Engineering Materials, 2006. **321-323**: p. 1370-1373.

37. Akyuz, B., *Influence of Al content on machinability of AZ series Mg alloys.* Transactions of Nonferrous Metals Society of China, 2013. **23**: p. 2243-2249.
38. Ambat, R., N.N. Aung, and W. Zhou, *Evaluation of microstructural effects on corrosion behaviour of AZ91D magnesium alloy.* Corrosion Science, 2000. **42**(8): p. 1433-1455.
39. Lunder, O., et al., *The Role of Mg17Al12 Phase in the Corrosion of Mg Alloy AZ91.* Corrosion, 1989. **45**(9): p. 741-748.
40. Song, G.-L., et al., *Corrosion behaviour of AZ21, AZ501 and AZ91 in sodium chloride.* Corrosion Science, 1998. **40**(10): p. 1769-1791.
41. Jonsson, M., D. Thierry, and N. LeBozec, *The influence of microstructure on the corrosion behaviour of AZ91D studied by scanning Kelvin probe force microscopy and scanning Kelvin probe.* Corrosion Science, 2006. **48**(5): p. 1193-1208.
42. Merino, M.C., et al., *Influence of chloride ion concentration and temperature on the corrosion of Mg-Al alloys in salt fog.* Corrosion Science, 2010. **52**(5): p. 1696-1704.
43. Cao, F., Shi, Z., Song, G.-L., Liu, M., Atrens, A., *Corrosion behaviour in salt spray and in 3.5% NaCl solution saturated with Mg(OH)2 of as-cast and solution heat-treated binary Mg–X alloys: X = Mn, Sn, Ca, Zn, Al, Zr, Si, Sr.* Corrosion Science, 2013. **76**.
44. Makar, G.L. and J. Kruger, *Corrosion of Magnesium.* International Materials Reviews, 1993. **38**(3): p. 138-153.
45. Loose, W.S., *Corrosion and Protection of Magnesium*. 1946, Materials Park, OH: ASM International. 173-260.
46. Mercer, W.E., hillis, J. E., *The Critical Contaminant Limits and Salt Water Corrosion Performance of Magnesium AE42 Alloy* in *SAE Technical Paper No 920073*. 1992.
47. Phipps, P.B.P., Rice, D.W., *The role of Water in Atmospheric Corrosion*, in *Corrosion Chemistry* 1979, American Chemical Society. p. 235-261.
48. Jones, D.A., *Principles and prevention of corrosion*. 2nd ed. 1996, Upper Saddle River, NJ: Prentice Hall.
49. *The Atmosphere*, in *Corrosion-Metal/Environment Reactions*, A.A. Shreir, Jarman, R.A., Burstein, G.T., Editor. 1994, Planta Tree: Great Britain. p. 31-35.
50. Stevenson, C.M., *An analysis of the chemical composition of rain-water and air over the British Isles and Eire for the years 1959–1964.* Quarterly Journal of the Royal Meteorological Society, 1968. **94**(399): p. 59-70.
51. Kusik, C.L., Meissner, H. P., *Electrolyte activity coefficients in inorganic processing*, in *AlChE Symp. Ser., No. 173.* 1978.
52. Askey, A., Lyon, S. B., Thompson, G. E., Johnson, J. B., Wood, G. C., Sage, P. W., Cooke, M. J., *The effect of fly-ash particulates on the atmospheric corrosion of zinc and mild steel.* Corrosion Science, 1993. **34**(7): p. 1055-1081.
53. Dunbar, S.R., Showak, W., *Atmospheric corrosion of zinc and its alloys*. Atmospheric Corrosion, ed. W.H. Ailor. 1982, New York: Wiley & Sons.
54. Froats, A., Aune, T. K., Hawke, D., Unsworth, W., Hillis, J., *Metals Handbook*. 9th ed. Vol. 13. 1987, Materials Park, OH: ASM International.
55. Lindstrom, R., *On the Chemistry of Atmospheric Corrosion-A laboratory study on Zn and Mg/Mg-Al Alloys*. 2001, Gothenburg.
56. Seinfeld, J.H., Pandis, S. N. , *Atmospheric chemistry and physics; from Air Pollution to Climate Change*. 1998: John Wiley and Sons Inc.
57. Heintzenberg, J., Tellus, series B: Chemical nad Physical Meteorology, 1989. **41**.
58. McCafferty, E., *Sequence of steps in the pitting of aluminum by chloride ions.* Corrosion Science, 2003. **45**: p. 1421-1438.

59. *Passivity and Localised Corrosion*, in *Corrosion-Metal/Environment Reactions*, A.A. Shreir, Jarman, R.A., Burstein, G.T., Editor. 1994, Planta Tree: Great Britain. p. 142-150.
60. Isaacs, H.S., *The Localized Breakdown and Repair of Passive Surfaces during Pitting.* Corrosion Science, 1989. **29**(2-3): p. 313-323.
61. Bertocci, U., et al., *A Statistical-Analysis of the Fluctuations of the Passive Current.* Journal of the Electrochemical Society, 1986. **133**(9): p. 1782-1786.
62. Hoar, T.P. and W.R. Jacob, *Breakdown of Passivity of Stainless Steel by Halide Ions.* Nature, 1967. **216**(5122): p. 1299-&.
63. Nguyen, T.H., Foley, R. T., *The Chemical Nature of Aluminum Corrosion: III . The Dissolution Mechanism of Aluminum Oxide and Aluminum Powder in Various Electrolytes.* Journal of the Electrochemical Society, 1980. **127**(12): p. 2563-2566.
64. Badawy, W.A., et al., *Kinetic-Studies on the Dissolution Behavior of Anodic Oxide-Films on Aluminum in Kf-Solutions.* Corrosion, 1986. **42**(6): p. 324-328.
65. Bockris, J.O. and Y.K. Kang, *The protectivity of aluminum and its alloys with transition metals.* Journal of Solid State Electrochemistry, 1997. **1**(1): p. 17-35.
66. Chao, C.Y., Lin, L. F., Macdonald, D. D. , *A Point Defect Model for Anodic Passive Films: I . Film Growth Kinetics.* Journal of the Electrochemical Society, 1981. **128**(1981): p. 1187-1194.
67. Godard, H.P., Jepson, W. B., Bothwell, M. R., Kane, r. L., *The corrosion of light metals*. 1967, New York: John Wiley and Sons.
68. Hui, H.D., Strekalov, P. V., Mikhailovskii, Y. N., Bin, D. T., Mmikhailov, A. A. , *Composition and microstructure of corrosion products of alluminum and MA2-1 magnesium alloy in the wet tropical climate of vietnam.* Protection of Metals, 1994. **30**(6): p. 506-508.
69. Mattson, E., *The atmospheric corrosion properties of some common structural metals - A comparative study*. 1982, National Association of Corrosion Engineers.
70. Fuente, D.d.l., Díaz, I., Simancas, I., Chico, B., Morcillo, M., *Long-term atmospheric corrosion of mild steel.* Corrosion Science, 2011. **53**: p. 604-617.
71. Grossman, D.M., *More Realistic Tests for Atmospheric Corrosion* in *ASTM Standardization News*. 1996, ASTM International: West Conshohocken, PA, USA.
72. *Test standards for the Q-FOG cyclic corrosion tester*. 2015 [cited 2015 June, 17]; Home>Resources>Standards>Test Standards for the Q-FOG Cyclic Corrosion Tester]. Available from: http://www.q-lab.com/resources/standards/category/q-fog-cyclic-corrosion-chamber.
73. LeBozec, N., Thierry, D., Rohwerder, M. Persson, D., Luckeneder, G., Luxem, L., *Effect of carbon dioxide on the atmospheric corrosion of Zn–Mg–Al coated steel.* Corrosion Science, 2013. **74**: p. 379-386.
74. Young, J.F., *HUMIDITY CONTROL IN THE LABORATORY USING SALT SOLUTIONS-A REVIEW.* Journal of Applied Chemistry, 1967. **17**: p. 241-245.
75. Chen, Y.Y., Chung, S. C., Shih, H. C., *Studies on the initial stages of zinc atmospheric corrosion in the presence of chloride.* Corrosion Science, 2006. **48**: p. 3547-3564.
76. Zhao, M.-C., Schmutz,P., Brunner, S., Liu, M., Song, G.-L., Atrens, A., *An exploratory study of the corrosion of Mg alloys during interrupted salt spray testing.* Corrosion Science, 2009. **51**: p. 1277-1292.
77. Blucher, D.B., J.E. Svensson, and L.G. Johansson, *The influence of CO2, ACl(3)center dot 6H(2)O, MgCl2 center dot 6H(2)O, Na2SO4 and NaCl on the atmospheric corrosion of aluminum.* Corrosion Science, 2006. **48**(7): p. 1848-1866.

78. Lindstrom, R., Svensson, J.-E., Johansson, L.-G., *The Influence of Salt Deposit on the Atmospheric Corrosion of Zinc.* Journal of the Electrochemical Society, 2002. **149**(2): p. B57-B64.
79. Prosek, T., Thierry, D., Taxén, C., Maixner, J., *Effect of cations on corrosion of zinc and carbon steel covered with chloride deposits under atmospheric conditions.* Corrosion Science, 2007. **49**(6): p. 2676-2693.
80. Pardo, A., et al., *Corrosion behaviour of magnesium/aluminium alloys in 3.5 wt.% NaCl.* Corrosion Science, 2008. **50**(3): p. 823-834.
81. Matsubara, H., Ichige, Y., Fujita, K., Nishiyama, H., Hodouchi, K., *Effect of impurity Fe on corrosion behavior of AM50 and AM60 magnesium alloys.* Corrosion Science, 2013. **66**: p. 203-210.
82. Shalaby, L.A., El Sobki, K. M., Abdul Azim, A. A. , *Corrosion of aluminium in chloride solutions containing some anions—I. In 0.01M NaCl solutions.* Corrosion Science, 1976. **16**(9): p. 637-643.
83. Borgmann, C.W., Evans, U. R., *THE CORROSION OF ZINC IN CHLORIDE SOLUTIONS.* Journal of Electrochemical Society, 1934. **65**(1): p. 249-274.
84. Jevremović, I., Singer, M., Nešić, S., Mišković-Stanković, V., *Inhibition properties of self-assembled corrosion inhibitor talloil diethylenetriamine imidazoline for mild steel corrosion in chloride solution saturated with carbon dioxide.* Corrosion Science, 2013. **77**: p. 265-272.
85. Falk, T., Svensson, J.-E., Johansson, L.-G., *The Role of Carbon Dioxide in the Atmospheric Corrosion of Zinc.* Journal of Electrochemical Society, 1998. **145**(1): p. 39-44.
86. Fürbeth, W., Stratmann, M., *Scanning Kelvin Probe investigations on the delamination of polymeric coatings from metallic surfaces.* Progress in Organic Coatings, 2000. **39**: p. 23-29.
87. Whitby, L., *The atmospheric corrosion of magnesium.* Transactions of the Faraday Society, 1933. **29**: p. 0844-0852.
88. Jonsson, M., D. Persson, and D. Thierry, *Corrosion product formation during NaCl induced atmospheric corrosion of magnesium alloy AZ91D.* Corrosion Science, 2007. **49**(3): p. 1540-1558.
89. Feliu Jr., S., Merino, M. C., Arrabal, R., Coy, A. E., Matykina, E. , *XPS study of the effect of aluminium on the atmospheric corrosion of the AZ31 magnesium alloy.* Surface and Interface Analysis, 2008. **41**: p. 143-150.
90. Pourbaix, M., *Atlas of Electrochemical Equilibria in Aqueous Solutions*. 1974, Houston, Texas, USA: NACE International.
91. Arrabal, R., et al., *Corrosion behaviour of Mg/Al alloys in high humidity atmospheres.* Materials and Corrosion-Werkstoffe Und Korrosion, 2011. **62**(4): p. 326-334.
92. Handwerker, C., Kattner, U., Moon, K.-W., *Non-Equilibrium Effects of Diffusion in the Solid on Equilibrium Solidification*, in *Lead-Free Soldering*, J.S. Bath, Editor. 2007, Springer: Milpitas, CA.
93. Magnesium.com, *Magnesium-Aluminum alloys*. 2013.
94. Jonsson, M., D. Persson, and C. Leygraf, *Atmospheric corrosion of field-exposed magnesium alloy AZ91D.* Corrosion Science, 2008. **50**(5): p. 1406-1413.
95. Arrabal, R., Mingo, B., Padro, A., Mohedango, M., Matykina, E., Rodriguez, *Pitting corrosion of rheocast A356 aluminium alloy in 3.5 wt.% NaCl solution.* Corrosion Science, 2013. **73**: p. 342-355.

96. Östklint, M., Wessén, M., Jarfors, A.E.W., *Microstructure and material soundness in liquid and rheocast AZ91: effect of section thickness.* International Journal of Cast Metals Research, 2013.
97. Haynes, R., *Interference microscopy*, in *Optical Microscopy of Materials*. 1984, Springer US. p. 77-87.
98. Grimm III, W.M., Fateley, W.G., Grasselli, J.G., *Introduction to Dispersive and Interferometric Infrared Spectroscopy*, in *Fourier Transform Infrare Spectroscopy-Industrial Chemical and Biochemical Applications*, T. Theophanides, Editor. 1984, D. Reidel: Dodrecht/Boston/Lancaster. p. 25-42.
99. Schindelin, J., Arganda-Carreras, I., Frise, E., Kaynig, V., Longair, M., Pietzsch, T., Preibisch, S., Rueden, C., Saalfeld, S., Schmid, B., Tinevez, J.-Y., White, D. J., Hartenstein, V., Eliceiri, K., Tomancak, P., Cardona, A., *Fiji: an open-source platform for biological-image analysis.* Nature Methods, 2012. **9**(7): p. 676-682.
100. Cavani, F., F. Trifiro, and A. Vaccari, *Hydrotalcite-Type Anionic Clays: Preparation, Properties and Applications.* Catalysis Today, 1991. **11**(2): p. 173-301.
101. Mascolo, G., Marino, O., *A new synthesis and characterization of magnesium-aluminium hydroxides.* Mineralogical Magazine, 1980. **43**: p. 619-621.
102. Taheri, M., et al., *Analysis of the surface film formed on Mg by exposure to water using a FIB cross-section and STEM-EDS.* Corrosion Science, 2012. **59**: p. 222-228.
103. Nordlien, J.H., et al., *Morphology and Structure of Oxide-Films Formed on Magnesium by Exposure to Air and Water.* Journal of the Electrochemical Society, 1995. **142**(10): p. 3320-3322.
104. Shahabi-Navid, M., Esmaily, M., Svensson, J.-E., Halvarsson, M., Nyborg, L., Cao, Y., Johansson, L.-G., *NaCl-Induced Atmospheric Corrosion of the MgAl Alloy AM50-The Influence of CO2.* Journal of the Electrochemical Society, 2014. **161**(6): p. C277-C287.
105. Lindstrom, R., et al., *Corrosion of magnesium in humid air.* Corrosion Science, 2004. **46**(5): p. 1141-1158.
106. Arrabal, R., et al., *Corrosion behaviour of AZ91D and AM50 magnesium alloys with Nd and Gd additions in humid environments.* Corrosion Science, 2012. **55**: p. 351-362.
107. Xiong, Y.L., *Experimental determination of solubility constant of hydromagnesite (5424) in NaCl solutions up to 4.4 m at room temperature.* Chemical Geology, 2011. **284**(3-4): p. 262-269.
108. Danaie, M., Asmussen, R. M., Jakupi, P., Shoesmith, D. W., Botton, G. A., *The role of aluminum distribution on the local corrosion resistance of the microstructure in a sand-cast AM50 alloy.* Corrosion Science, 2013. **77**: p. 151-163.
109. Cabrera, N. and N.F. Mott, *Theory of the Oxidation of Metals.* Reports on Progress in Physics, 1948. **12**: p. 163-184.
110. Do, T., et al., *The oxidation kinetics of Mg and Al surfaces studied by AES and XPS.* Surface Science, 1997. **387**(1-3): p. 192-198.
111. Splinter, S.J. and N.S. Mcintyre, *The Initial Interaction of Water-Vapor with Mg-Al Alloy Surfaces at Room-Temperature.* Surface Science, 1994. **314**(2): p. 157-171.
112. Refson, K., et al., *Water Chemisorption and Reconstruction of the Mgo Surface.* Physical Review B, 1995. **52**(15): p. 10823-10826.
113. Unocic, K.A., et al., *Transmission Electron Microscopy Study of Aqueous Film Formation and Evolution on Magnesium Alloys.* Journal of the Electrochemical Society, 2014. **161**(6): p. C302-C311.

114. White, A.H. *Volume Changes of Portland Cement as Affected by Chemical Composition and Aging*. in *ASTM*. 1928.
115. Birchal, V.S., et al., *A simplified mechanistic analysis of the hydration of magnesia.* Canadian Journal of Chemical Engineering, 2001. **79**(4): p. 507-511.
116. Grauer, V.R., *Feste Korrosionsprodukte – I. Magnesium, Zink, Cadmium, Blei und Kupfer.* Werkstoffe und Korrosion, 1980. **31**: p. 837-850.
117. Holt, S., A., Jones, G., S., Crossley, A., Johnston, C., Sofield, C., J., Myhra, S., *Surface modification of MgO substrates from aqueous exposure: an atomic force microscopy study*. Thin Solid Films, 1997. **292**: p. 96-102.
118. Coluccia, S., A. Barton, and A.J. Tench, *Reactivity of Low-Coordination Sites on the Surface of Magnesium-Oxide.* Journal of the Chemical Society-Faraday Transactions I, 1981. **77**: p. 2203-2207.
119. Jones, C.F., et al., *Surface-Structure and the Dissolution Rates of Ionic Oxides.* Journal of Materials Science Letters, 1984. **3**(9): p. 810-812.
120. Allen, J.P., A. Marmier, and S.C. Parker, *Atomistic Simulation of Surface Selectivity on Carbonate Formation at Calcium and Magnesium Oxide Surfaces.* Journal of Physical Chemistry C, 2012. **116**(24): p. 13240-13251.
121. Xiong, Y.L. and A.S. Lord, *Experimental investigations of the reaction path in the MgO-CO(2)-H(2)O system in solutions with various ionic strengths, and their applications to nuclear waste isolation.* Applied Geochemistry, 2008. **23**(6): p. 1634-1659.
122. Gautier, Q., et al., *Hydromagnesite solubility product and growth kinetics in aqueous solution from 25 to 75 degrees C.* Geochimica Et Cosmochimica Acta, 2014. **138**: p. 1-20.
123. Zander, D., Schnatterer, C., *The influence of manufacturing processes on the microstructure and corrosion of the AZ91D magnesium alloy evaluated using a computational image analysis.* Corrosion Science, 2015.
124. Esmaily, M., et al., *Microstructural characterization of the Mg-Al alloy AM50 produced by a newly developed rheo-casting process.* Materials Characterization, 2014. **95**: p. 50-64.
125. Esmaily, M., et al., *Effect of Rheocasting on Corrosion of AM50 Mg Alloy.* Journal of the Electrochemical Society, 2015. **162**(3): p. C85-C95.
126. Sachdeva, D., *Insights into microstructure based corrosion mechanism of high pressure die cast AM50 alloy.* Corrosion Science, 2012. **60**: p. 18-31.
127. Jonsson, M., D. Persson, and R. Gubner, *The initial steps of atmospheric corrosion on magnesium alloy AZ91D.* Journal of the Electrochemical Society, 2007. **154**(11): p. C684-C691.
128. Danaie, M., et al., *The cathodic behaviour of Al-Mn precipitates during atmospheric and saline aqueous corrosion of a sand-cast AM50 alloy.* Corrosion Science, 2014. **83**: p. 299-309.
129. Chen, Z.Y., et al., *In situ studies of the effect of CO2 on the initial NaCl-induced atmospheric corrosion of copper.* Journal of the Electrochemical Society, 2005. **152**(9): p. B342-B351.
130. Song, G.-L. and Z.Q. Xu, *Crystal orientation and electrochemical corrosion of polycrystalline Mg.* Corrosion Science, 2012. **63**: p. 100-112.
131. Song, G.L., R. Mishra, and Z.Q. Xu, *Crystallographic orientation and electrochemical activity of AZ31 Mg alloy.* Electrochemistry Communications, 2010. **12**(8): p. 1009-1012.
132. Liu, M., et al., *The effect of crystallographic orientation on the active corrosion of pure magnesium.* Scripta Materialia, 2008. **58**(5): p. 421-424.